Improving the modelling of the associated production of W-bosons and jets in the ATLAS detector

Verbesserung der Modellierung der assoziierten Produktion von W-Bosonen und Jets im ATLAS Detektor

Masterarbeit der Fakultät für Physik
der
Ludwig-Maximilians-Universität München

vorgelegt von
Adam Samara

München, den 07. Februar 2018

Abstract

Supersymmetry is a theoretical extension of the Standard Model of particle physics and provides a framework that can resolve most of the limitations that arise within the Standard Model, as for instance the Hierarchy problem, which is why a large effort is put into searching for superymmetric particles at the Large Hadron Collider at CERN. Inside the accelerator, protons collide in bunches with a frequency of 40 MHz, producing a tremendous amount of physical processes. The majority of these processes do not contain new physics. Thus, an efficient separation of the interesting signal events from the Standard Model background processes is crucial for analysing recorded data. Monte Carlo simulation is used to estimate the background events.

This thesis presents a method to reduce the statistical uncertainties of Monte Carlo background events, namely the associated production of a W-boson together with jets, for searches that contain two tau leptons in the final state.

Results are shown for the application of the method to the search for pair production of scalar tau leptons with a subsequent hadronic decay into a Standard Model tau lepton and a lightest neutralino at a center-of-mass energy of $\sqrt{s}$=13 TeV, scaled to an integrated luminosity of 36.1 fb^{-1}, which corresponds to the data recorded by ATLAS in 2015 and 2016.

Zusammenfassung

Supersymmetrie ist eine theoretische Erweiterung des Standardmodells der Teilchenphysik und kann die Probleme des Standardmodells, wie beispielsweise das Hierarchieproblem, zum größten Teil lösen, weshalb am Large Hadron Collider am CERN intensiv nach supersymmetrischen Teilchen gesucht wird. Protonen kollidieren in dem Beschleuniger mit einer Frequenz von 40 MHz, wodurch eine enorme Menge an physikalischen Prozessen entsteht. Die Mehrheit dieser Prozesse enthält keine neue Physik. Daher ist eine effiziente Trennung des Standardmodell-Untergrunds von den interessanten Signalereignissen nötig, um die aufgezeichneten Daten zu analysieren. Für die Untergrundabschätzung wird Monte Carlo Simulation verwendet.

In dieser Arbeit wird eine Methode präsentiert, die die statistischen Unsicherheiten der Monte Carlo Untergrundmodellierung für die assoziierte Produktion eines W-Bosons zusammen mit Jets für Analysen mit zwei Tau-Leptonen im Endzustand reduziert.

Die Ergebnisse für die Anwendung dieser Methode werden für die Suche nach direkter Produktion von supersymmetrischen skalaren Tau-Leptonen bei einer Schwerpunktsenergie von $\sqrt{s}$=13 TeV, normiert auf eine integrierte Luminosität von 36,1 fb^{-1}, welche den von ATLAS aufgezeichneten Daten in den Jahren 2015 und 2016 entspricht, gezeigt.

Contents

1 Introduction

The endeavour of searching for the last elementary particle predicted by the Standard Model of particle physics led to success with the discovery of the Higgs boson in 2012 [1] [2]. Besides further investigations of the Standard Model, the aim of particle physicists is to find evidence for theories beyond it. This is due to remaining open questions, which answers are not able to be provided for the Standard Model.

A site that makes these studies possible is the Large Hadron Collider (LHC), the largest and most powerful of its kind, at the European Organization for Nuclear Research CERN in Geneva. After its first run, at which it was operating at a center of mass energy up to $s = \sqrt{8}$ TeV it was shut down for two years to enhance its performance, now enabling it to reach a center of mass energy of $s = \sqrt{1}3$ TeV. Also, the experiments were upgraded during that time in order to take data more efficient, hence increasing chances to explore new physics.

One of the theories that serves as an extension to the Standard Model, solving many of its problems, is Supersymmetry. The main concept behind Supersymmetry is that each fermion has an associated bosonic partner, called its superpartner, the spin of which differs by a half integer, and vice versa. In unbroken Supersymmetry the superpartners would have the same mass as their corresponding Standard Model particles. However, as there was no observation of supersymmetric particles yet, they must have larger masses, which are more likely to be reached in the second run of the LHC. In order to examine if candidates for new physics were produced, the decay products of the particles originating from the collision are analysed, which gives information about the initial particles. Knowing the end states of the processes involving supersymmetric particles, it is crucial to be able to separate them from identical or similar final states that do not include new physics, so called background.

This thesis presents a method that improves the background estimation and hence enables better signal efficiency. In the following, the theory of the Standard Model as well as Supersymmetry are shown in more detail and the experimental setup of the LHC and ATLAS detector is illustrated. Afterwards, object and event selections are defined and the specific analysis which was the motivation for developing Tau-Promotion is described. In addition the concept of the method is explained and studies concerning different approaches of its functionality as well as the results obtained by using the method are exhibited.

2 Theory

This section gives a brief overview of the Standard Model of particle physics and its limitations followed by an introduction to Supersymmetry, elucidating its motivation and theoretical concepts. In addition the process relevant for the analysis, for which the Tau-Promotion method was developed, is illustrated.

2.1 Standard Model

The Standard Model of particle physics provides a framework in which the fundamental particles and the forces interacting between them are described with high accuracy [3] [4] . However, one stumbles upon some problems, for example concerning energies at the reduced Planck scale $M_P = (8\pi G_{Newton})^{-1/2} = 2.4 \times 10^{18}\text{GeV}$, where quantum gravitational effects become crucial [5]. These problems are addressed further in section 2.1.3. This suggests that the Standard Model is a low energy approximation of a more complex theory, providing tools that can solve the problems that the Standard Model has.

2.1.1 Quantum field theory

The Standard Model is a quantum field theory (QFT) with the gauge groups $SU(3) \otimes SU(2) \otimes U(1)$, which are internal symmetries of the Lagrangian, depicting the mediators of force, the gauge bosons. QFT comprises aspects of special relativity combined with quantum mechanics and is described by a field formalism, where the fundamental particles are represented as excitations of these fields. It is based on the Lagrangian formalism analogous to classical mechanics, where the Euler Lagrange equation

$$\frac{\partial}{\partial x^\mu}\left[\frac{\partial \mathcal{L}}{\partial(\frac{\partial \varphi}{\partial x^\mu})}\right] - \frac{\partial \mathcal{L}}{\partial \varphi} = 0 \tag{2.1}$$

with the Lagrangian density $\mathcal{L}$ provides a solution for the equation of motion. In QFT the same Lagrangian procedure is used and the equations of motions are then complemented by commutation relations known from quantum mechanics. The local $U(1)$ symmetry gives the framework for the interaction of a boson with particles

and describes the electromagnetic interaction, referred to as quantum electrodynamics (QED). Its gauge boson is a photon. $SU(3)$ represents quantum chromodynamics (QFT), which describes the interaction between particles carrying colour charge with the gluon as the mediating gauge boson [6]. The unification of electromagnetic and weak theory, the electroweak theory, is described by $SU(2) \times U(1)$. Due to the Higgs field, where the W- and Z-bosons get their mass from via the Higgs-mechanism, this a spontaneously broken symmetry.

2.1.2 Particle Content

The fundamental particles of the Standard Model are divided into two groups: Fermions possessing half-integer spin and bosons with integer spin. Fermions make up the known matter and are further divided into quarks and leptons, each of which occuring in three generations. Each generation is made up of an up- and down-like quark, a charged lepton and a neutral lepton, the neutrino. The fermions of the SM are illustrated in Table Table 2.1 and Table 2.2 Fermions follow the Fermi Dirac statistics and obey the Pauli Principle, which states that the wave function is antisymmetric under exchange of two identical particles implying that two indistinguishable fermions can not occupy the exact same quantum state.

Name	Symbol	Charge [e]	Mass [MeV]
up	u	2/3	2.2
down	d	-1/3	4.7
charm	c	2/3	$1.27 \cdot 10^3$
strange	s	-1/3	96
top	t	2/3	$173.2 \cdot 10^3$
bottom	b	-1/3	$4.18 \cdot 10^3$

Table 2.1: The quarks of the SM, taken from [7].

Name	Symbol	Charge [e]	Mass [MeV]
electron	e	-1	0.511
electron-neutrino	ν_e	0	$< 2 \cdot 10^{-6}$
muon	μ	-1	105.7
muon-neutrino	ν_μ	0	$< 2 \cdot 10^{-6}$
tau	τ	-1	$1.776 \cdot 10^3$
tau-neutrino	ν_τ	0	$< 2 \cdot 10^{-6}$

Table 2.2: The leptons of the SM, taken from [8].

Bosons follow the Bose-Einstein statistics, which does not restrict the number of them occupying the same state. The bosons of the SM are listed in Table 2.3. Bosons with

spin 1 mediate forces: Photons mediate the electromagnetic interaction, W- and Z-bosons mediate the weak interaction and gluons are the force carriers for the strongest interaction. Concerning the last remaining force, gravity, it is assumed that its gauge boson is the spin 2 graviton, however there were no observations made yet. The scalar Higgs boson is the quantum excitation of the Higgs field, giving mass to the W- and Z-bosons via spontaneous symmetry breaking and enabling Yukawa coupling to massless quark and lepton fields.

Name	Symbol	Charge [e]	Mass [MeV]	Spin
higgs	H^0	0	$125.09 \cdot 10^3$	0
W	$W^{\pm}$	± 1	$80.39 \cdot 10^3$	1
Z	Z^0	0	$91.19 \cdot 10^3$	1
photon	γ	0	0	1
gluon	g	0	0	1
graviton	G	0	0	2

Table 2.3: The bosons of the SM, taken from [9]

2.1.3 Open Questions

One of the SM's limitations is the so called hierarchy problem, which refers to the large deviation between aspects of the weak force and gravity. The SM does not provide any explanation why the weak force, that involves Fermis constant, is stronger than gravity, which depends on Newtons constant, by a factor of 10^{24} [10]. This question leads to the Higgs boson, more precisely to the question why the Higgs boson is so much lighter than the Planck mass. The large quantum contributions to the square of the Higgs boson is expected to make its mass huge, unless some fine tuning cancellation between the quadratic radiative corrections and the bare mass occurs, which can not be formulated with the SM. The Higgs potential in the SM is

$$V = m_H^2|H|^2 + \lambda|H|^4, \tag{2.2}$$

with the Higgs mass m_{H}, a complex scalar H, and the Higgs self-coupling constant λ. The Higgs potential must have a non-vanishing vacuum expectation value for H at the minimum in the SM. The underlying problem is that the large quantum contributions to the square of the mass of Higgs boson from a loop containing a Dirac fermion f with mass m_f is expected to make its mass huge. These quantum contributions are shown in Figure 2.1 and the correction, if the Higgs field couples to f, is

$$\Delta m_H^2 = \frac{|\lambda_f|^2}{8\pi^2}\Lambda_{UV}^2 + ... , \tag{2.3}$$

with the ultraviolet momentum cutoff Λ_{UV} needed to regulate the loop integral. The problem occurs if Λ_{UV} is of the order of the Planck scale M_P, what makes this

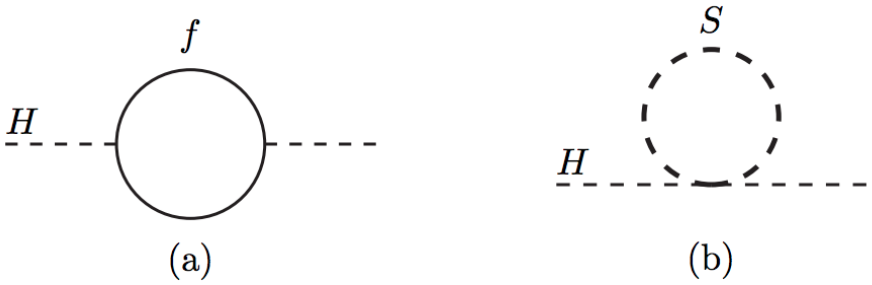

Figure 2.1: One-loop quantum contributions to the Higgs squared mass m_H^2 caused by (a) a Dirac fermion f, and (b) a scalar S.

quantum correction about 30 orders of magnitude larger than the required value of $m_H^2 \approx -(92.9\text{GeV})^2$. As the electroweak gauge bosons Z^0, $W^\pm$ of the SM receive their mass from the Higgs field, the entire mass spectrum of the SM is sensitive to the cutoff Λ_{UV}. Solving the problem by choosing a smaller Λ_{UV} is not possible as one would need new physics at the scale Λ_{UV} that cuts off the loop integral. In a theory whose Lagrangian does not contain more than two derivatives, this is difficult, and higher-deviative theories in general suffer from a failure of either unitary or causality. The alternative would be that some fine tuning cancellation between the quadratic radiative corrections and the bare mass occurs. One could exploit the sign difference between fermion and boson loops and tune the magnitude of the other couplings in order to keep the net contribution to the Higgs mass in 100 GeV range. However, even if couplings are adjusted in a certain order in perturbation theory, the adjustment is offset in the next order, which is why the tuning has to be done order by order. [11]

Another problem of the Standard Model is the fact that gravity is not included. Gravity can be neglected in the description of particle physics experiments as it is the weakest force, however, gravitational effects become relevant at the Planck scale at $10^{19}GeV$.

Furthermore, the SM only explains a fractional amount of the energy, about 5%, present in the universe. The rest of the energy of the universe consists of about 26% Dark Matter, which does not or does only weakly interact with the SM fields. The SM does not offer a particle suitable as a candidate for Dark Matter. The remaining energy of the universe is made up of Dark Energy, a constant energy density for the vacuum, which can not be explained in terms of vacuum energy of the SM.

Besides the observation of neutrino oscillations, a phenomenon whereby a neutrino created with a specific lepton flavour is later measured to have a different flavour, proved that neutrinos do have mass. Mass terms of the neutrinos can be added to the SM by hand, but they create new theoretical problems. These problems arise by the fact that the mass terms have to be exceedingly small and it is not clear if the masses originate in the same way in which the masses of other SM particles do.

The matter-antimatter asymmetry marks another phenomenon, that the SM fails to

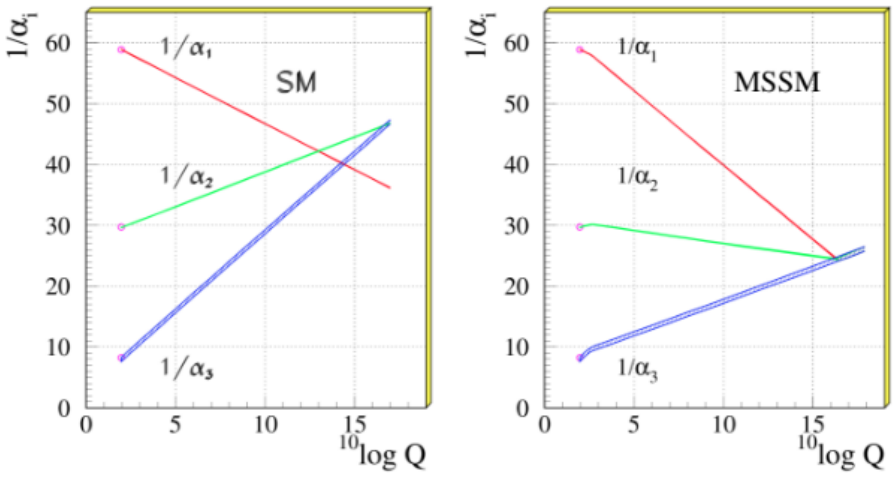

Figure 2.2: The scale dependence of the gauge couplings α_1, α_2 and α_3 in the SM and the MSSM, showing that that do only converge for the MSSM, making it a candidate for a unified theory [12].

explain. It refers to the disequilibrium between baryonic matter and antibaryonic matter in the universe. The SM predicts that matter and antimatter have been produced in equal amounts at the Big Bang.

Another limitation of the SM is reached regarding unified theories, which state that the weak, strong and electromagnetic interactions are only different aspects of one single interaction. Within the SM it is not possible to obtain an unified theory as for that reason, the three scale-dependent gauge couplings α_1, α_2 and α_3 of the SM gauge group $SU(3) \otimes SU(2) \otimes U(1)$ have to converge at a high energy scale. In Figure 2.2 the gauge couplings of the SM and the so called Minimal Supersymmetric Standard Model (MSSM), are illustrated, showing that the gauge couplings do not converge in the SM in contrast to the MSSM. The MSSM and SUSY in general will be explained below.

2.2 Supersymmetry

In order to solve the limitations of the SM, a theory beyond the SM is needed. Supersymmetry is such an extension that makes it possible to answer the majority of the remaining open questions, which is why a large effort is being made verifying its existence via experimental observation. A brief summary of the theory behind SUSY is given below [13] [14] [15].

2.2.1 Algebra

The basic concept of SUSY is that the particle content of the SM is extended, by making it possible that each fermionic state can be transformed into a bosonic one and vice versa through an operator Q:

$$Q|\text{fermion}\rangle = |\text{boson}\rangle, \tag{2.4}$$
$$Q|\text{boson}\rangle = |\text{fermion}\rangle \tag{2.5}$$

associating each SM particle with a supersymmetric partner that differs in spin by $1/2$. The supersymmetric algebra extends the ordinary Lorentz symmetry groups of 4d quantum field theory by additional fermionic generators, which are the Weyl spinors. There are N such generators Q_α with their Hermitian conjugates $Q^\dagger_{\dot{\alpha}}$. α and $\dot{\alpha}$ are spinor indices which transform as the fundamental (anti-fundamental) representatives of $SU(2,\mathbb{C})$, where undotted indices refer to left-handed fermions and dotted indices refer to right-handed ones and the index runs over the values $\alpha \in \{1,2\}$:

$$\{Q_\alpha, Q_{\dot{\beta}}\} = \{Q^\dagger_\alpha, Q^\dagger_{\dot{\beta}}\} = 0. \tag{2.6}$$

The extension of the Poincaré algebra shows how SUSY is connected to spacetime translations with the following anti-commuting relation:

$$\{Q_\alpha, Q^\dagger_{\dot{\beta}}\} = 2\sigma^\mu_{\alpha\beta} P_\mu, \tag{2.7}$$

where P^μ represents the four-momentum generator for spacetime translations, which follow the commutation relation

$$[P_\mu, P_\nu] = 0. \tag{2.8}$$

σ^μ are the Pauli matrices, which state how the tensor product $2 \otimes \bar{2}$ of the two spinors can be expressed as vector. The Dirac matrices γ^μ can be expressed as direct sums of the Pauli matrices with the tensor product giving an algebraic relation to the Minkowski metrik $g^{\mu\nu}$, which is described by $\{\gamma^\mu, \gamma^\nu\} = 2g^{\mu\nu}$ and $\sigma^{\mu\nu} = \frac{i}{2}[\gamma^\mu, \gamma^\nu]$. SUSY is independent of spacetime position, making it an internal symmetry, which is expressed by the commutator

$$[P_\mu, Q_\alpha] = [P_\mu, Q^\dagger_{\dot{\alpha}}] = 0 \tag{2.9}$$

As a consequence from this equation the squared-mass operator $P^2 = P^\mu P_\nu$ commutes with Q, what implies that superpartners have the same mass, as all particles within the same supermultiplet have the same eigenvalue of $-P^2$. Due to the fact that there have been no superpartners observed yet, disproving that they have equal mass, SUSY has to be a broken symmetry [16]. The transformations involving the Lorentz generators $\Lambda^{\alpha\beta}$ can be summarized by the statement that Q_α transforms as a spinor under Lorentz transformations with the generator $M^{\mu\nu}$ and μ, ν ranging over the space-time dimensions $\mu, \nu \in \{0,1,2,3\}$:

$$[Q_\alpha, M^{\mu\nu}] = (\sigma^{\mu\nu})^\beta_\alpha Q_\beta. \tag{2.10}$$

2.2.2 The Minimal Supersymmetric Standard Model (MSSM)

The Minimal Supersymmetric Standard Model (MSSM) is an extension of the SM $SU(3) \otimes SU(2) \otimes U(1)$ gauge theory with one generator, called N=1 SUSY [17]. In this theory, a vector superfield (VFS) is assigned to each gauge field and a chiral superfield (χ SF) to each matter field. The VSF contains one gauge boson and a Weyl fermion, called gaugino, as physical particles, while the χ SF contains one Weyl fermion and one complex scalar. New superpartners have to be introduced to each SM gauge boson as none of the SM fermions transform under the adjoint of the gauge group and are thus not able to be identified with the gauginos. Table 2.4 illustrates the χ SFs in the MSSM. The spin-0 fields are complex scalars and the spin-$1/2$ are left-handed two-component Weyl fermions.

Name	spin 0	spin $1/2$	$SU(3)_C,\ SU(2)_L,\ U(1)_Y$
squarks, quarks (3 generations)	$(\tilde{u_L}\ \tilde{d_L})$	$(u_L\ d_L)$	$(3,\ 2,\ 1/6)$
	$\tilde{u}^*_R$	$u^\dagger_R$	$(\bar{3},\ 1,\ -2/3)$
	$\tilde{d}^*_R$	$d^\dagger_R$	$(\bar{3},\ 1,\ 2/3)$
sleptons, leptons (3 generations)	$(\tilde{\nu}\ \tilde{e^L})$	$\nu\ e^L)$	$(1,\ 2,\ -1/2)$
	$\tilde{e}^*_R$	$\dagger e^*_R$	$(1,\ 1,\ 1)$
Higgs, higgsino	$(H^+_u\ H^0_u)$	$(\tilde{H}^+_u\ \tilde{H}^0_u)$	$(1,\ 2,\ +1/2)$
	$(H^0_d\ H^-_d)$	$(\tilde{H}^0_d\ \tilde{H}^-_d)$	$(1,\ 2,\ -1/2)$

Table 2.4: The chiral supermultiplet fields in the MSSM.

In order for the gauge anomalies to cancel the third component of weak isospin T_3 and the weak hypercharge Y in a normalization where the ordinary electric charge is $Q_{EM} = T_3 + Y$ must satisfy $\mathrm{Tr}[T_3^2 Y] = \mathrm{Tr}[Y^3] = 0$. In the SM these conditions are fulfilled by the known quarks and leptons. Considering a fermionic partner of a Higgs chiral supermultiplet it has to be a weak isodoublet with weak hypercharge $Y = 1/2$ or $Y = -1/2$, which would cause a non-zero contribution to the traces in both cases and prevent the anomaly cancellation. This can be solved by adding another Higgs supermultiplet, resulting in two Higgs supermultiplets with each of $Y = \pm 1/2$ so that the total contribution to the traces vanishes by cancellation. The SM Higgs boson can be described as a linear combination of H_u and H_d and its superpartner is called higgsino, where the $SU(2)_L$-doublet left-handed Weyl spinor fields are denoted as $\tilde{H}_u$ and $\tilde{H}_d$.

As H_d has exactly the same gauge quantum numbers as the left-handed sleptons and leptons L_i, one might suppose that a neutrino is the superpartner of the Higgs. The conclusion would be that the Higgs boson and a sneutrino are the same particle, however, this does not work due to resulting phenomenological problems, including non-conservation of lepton-number and large deviation for the mass of at least one neutrino with respect to experimental bounds. For this reason, each superpartner of the cor-

responding SM particle is a new particle, meaning that it cannot be identified with another SM state.

The fermionic superpartners of the SM vector bosons are denoted as gauginos. The superpartner of the gluon g, mediator of the $SU(3)_C$ color gauge interactions of QCD, is the spin-1/2 color-octet gluino $\tilde{g}$. Mediators of the electroweak interactions with gauge symmetry $SU(2)_L \times U(1)_Y$, namely the spin-1 gauge-bosons W^+, W^-, W^0 and B^0, are associated to the superpartners $\tilde{W}^+$, $\tilde{W}^-$, $\tilde{W}^0$ and $\tilde{B}^0$, called winos and binos. The mass eigenstates Z^0 and γ result after the electroweak symmetry breaking from the W^0 and B^0, and their superpartners are called zino ($\tilde{Z}^0$) and photino ($\tilde{\gamma}$). Table 2.5 summarizes the gauge supermultiplets of the MSSM [18].

Name	spin 0	spin 1/2	$SU(3)_C,\ SU(2)_L,\ U(1)_Y$
gluino, gluon	$\tilde{g}$	g	(8, 1, 0)
winos, W-bosons	$\tilde{W}^+\ \tilde{W}^-\ \tilde{W}^0$	$W^+\ W^-\ W^0$	(1, 3, 0)
bino, B-boson	$\tilde{B}^0$	B^0	(1, 1, 0)

Table 2.5: The gauge supermultiplet fields in the MSSM.

Furthermore the gauge couplings of the MSSM converge at the Grand Unified Theory (GUT) scale, suggesting that there is a higher unified structure present at exceedingly small scales. However, there is no direct evidence for GUTs as the proton decay, which has not been observed yet [19] [20].

2.2.3 Soft Supersymmetry breaking interactions

As earlier mentioned, SUSY has to be a broken symmetry due to the fact that the superpartners do not have the same mass as the corresponding SM particles. SUSY is expected to be an exact symmetry that is broken spontaneously, meaning that the Lagrangian density of the fundamental model should be invariant under SUSY, but its vacuum state should not [21] [22]. Additionally, the SUSY-breaking couplings should be soft, i.e. of positive mass dimension, so that a hierarchy between the electroweak scale and the Planck scale can be naturally maintained.

2.2.4 R-parity

The superpotential of the MSSM is

$$W_{\text{MSSM}} = \bar{u}\mathrm{y_d}QH_u - \bar{d}\mathrm{y_d}QH_u - \bar{e}\mathrm{y_d}LH_d = \mu H_u H_d \tag{2.11}$$

with the chiral superfields $H_u, H_d, Q, L, \bar{u}, \bar{d}, \bar{e}$. The superpotential is sufficient to produce a phenomenological usable model. Other terms could be added that are gauge-invariant and holomorphic in the chiral superfields, yet they are not included in the MSSM as they violate either baryon number B or lepton number L. Processes described by the SM conserve B and L, which is manifested by the fact that the proton is stable. Although it is already known that B and L are violated by non-perturbative electroweak effects, this fact can be neglected at ordinary energies in particle physics experiments far below the Planck scale. Thus, a new symmetry is introduced in the MSSM, that eliminates the possibility of B- and L-violating terms in the renormalizable superpotential, called R-parity. R-parity is defined as

$$P_R = (-1)^{3(\mathrm{B}-\mathrm{L})+2s} \tag{2.12}$$

with baryon number B, lepton number L and the spin s of the particle. For SM particles one obtains even parity ($P_R = +1$) and for SUSY particles odd parity ($P_R = -1$). Assuming R-Parity is conserved, every interaction vertex contains an even number of sparticles. As a consequence the lightest supersymmetric patricle (LSP) has to be stable. If the LSP is electrically neutral, it only takes part in weak interactions with ordinary matter, which makes it a candidate for Dark Matter [23] [24]. Furthermore, every other sparticle must ultimately decay into a state containing an odd number of LSPs and sparticles can only be produced pairwise in collider experiments.

2.2.5 Investigated signal model

The analysis in this thesis is targetting the search for SUSY in a simplified model, defined by a set of particles as well a sequence of their production and decay. Within a simplified model only the production process for a limited number of particles in the decaychain is considered and the branching ratio is assumed to be 100% The process embraced in the following is the direct pair production of scalar taus $\tilde{\tau}$. The scalar tau pairs can be produced via a Drell-Yan process and decay subsequently into one SM τ-lepton and one lights neutalino $\tilde{\chi}_1^0$ what is assumed to be the LSP as it is stable. The Feynman diagram for this process is shown in Figure 2.3. As the neutralino only takes part in weak interactions it is not possible to detect it directly, but it causes missing transvere energy, a mismatch of the total momentum of all produced particles. The τ-leptons decay in three different decay modes. The three possibilities are that both τ-leptons decay hadronically (HadHad-channel), both decay leptonically (LepLep-channel) or one decays leptonically and the other one hadronically (LepHad-channel). As the LepLep- channel has a relatively small branching ratio, the main effort of the studies is focused on the other two decay modes. In this model, the $\tilde{\tau}_1$ is assumed to be purely left-handed, whereas the $\tilde{\tau}_2$ is right-handed. The cross sections depend on the stau mass, ranging from 0.07 pb to 0.8 pb for stau masses between 80 GeV and 260 GeV.

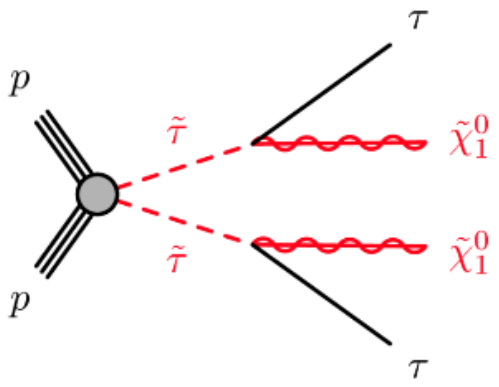

Figure 2.3: Feynman diagram for the direct production of scalar tau leptons $\tilde{\tau}$, each of which subsequently decaying into a lightest neutralino $\tilde{\chi}_1^0$ and a SM τ, taken from [25]

Final states with tau leptons are experimentally challenging, however, of particular interest for studies searching for SUSY. Light sleptons could be involved in the coannihilation of neutralinos, and models with light staus can lead to a dark matter relic density consistent with the one cosmologically observed.

Due to multiple SM processes that either exhibit the same or a similar signature in the detector as the signal process, called background processes, it is crucial to obtain a good background rejection, while keeping the signal efficiency as high as possible. That implies a precise background estimation, which is done using Monte Carlo simulation. Monte Carlo simulation and the several background processes for the signal considered in this analysis are specified in chapter 4.

One background process is the associated production of a W-boson together with other physical objects, called W+jets. However, there is one problem with this particular one: Only a small fraction of the Monte Carlo simulated events for this process has the needed signature of two τ-leptons and missing transverse energy and can thus be used to estimate the background for this analysis. This results in high uncertainties making it impossible to get any sensitivity. The reweighting method Tau Promotion was designed to improve the statistical uncertainties for the W+jets background with this particular signature.

3 Experimental Setup

Several scientific breakthroughs in particle physics have been achieved at the European Organization for Nuclear Research CERN, the most recent one being the discovery of a boson consistent with the Higgs boson, which was the last SM particle that had not been observed. A large effort is currently put into searches for physics beyond the SM, including the search for SUSY. The following chapter gives an overview of the setup of the LHC at CERN and the ATLAS experiment located at the LHC.

3.1 The Large Hadron Collider

The LHC is extended to a size of 27 kilometers in circumference and is located in a tunnel as deep as 175 metres beneath the France-Switzerland border near Geneva, Switzerland. This tunnel had been initially constructed for the Large Electron- Positron Collider (LEP), where, as the name suggests, electron-positron collision took place, reaching a center-of-mass energy of $\sqrt{s}$=209 GeV. LEP has been operating from 1989 until 2000, when it was shut down so that the LHC could be built. The LHC represents the ultimate part of the CERN accelerator complex, a sequence of machines where the beam is injected from each machine into the other one with increasing higher energies, reaching a center of mass energy of $\sqrt{s}$=13 GeV. Figure 3.1 shows the CERN accelerator complex. Protons, originating from hydrogen atoms, are initially injected into the PS Booster, reaching an energy of 1.4 GeV. Afterwards, they are directed into the Proton Synchrotron, where they are accelerated to 25 GeV, and are sent to the Super Proton Synchrotron, which accelerates them to 450 GeV, before they are transferred in bunches to the LHC, both clockwise and anti-clockwise in two separate beam-pipes in order to compose two counter-rotating beams. Each beam is made up of 2808 bunches, each bunch consisting of 10^{11} protons, under nominal operation conditions. At full luminosity the bunch spacing amounts to 25 ns. However, the bunch size varies around the ring, as it is squeezed around the interaction point to about 20 μm, to increase the probability of a collision, and is expanded again to a few centimetres to travel through the beam-pipe. The time between two bunch crossings of 25 ns corresponds to a frequency of 40 MHz, but for practical reasons there are a few larger gaps in the pattern of bunches allowing for example the kicker magnets to inject or dump the beams. Thus, the average bunch crossing frequency is lower, with a frequency about 30 MHz.

The LHC is not a perfect ring as it consists of eight straight sections and eight arcs.

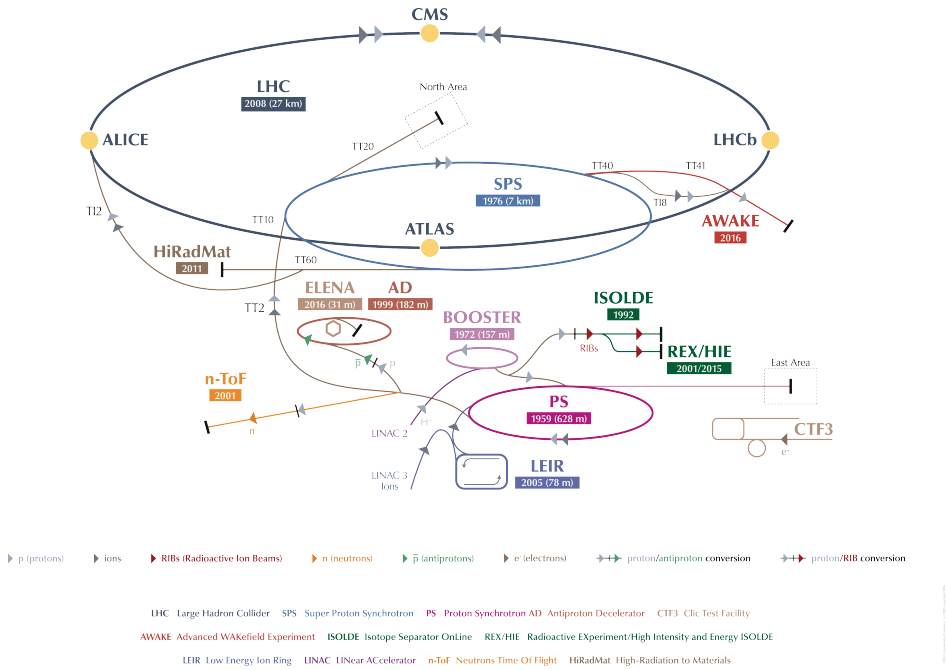

Figure 3.1: Schematic overview of the CERN accelerator complex [26].

There are three vacuum systems within the LHC: insulation vacuum for cryomagnets, insulation vacuum for the helium distribution line and beam vacuum. In the vacuum tube dipole magnets keep the particles in circular orbits, quadrupole magnets focus the beam and electromagnetic resonators accelerate the particles and compensate for energy losses maintaining them at constant energy. The dipole magnets with a magnetic field of 8.33 T use niobium-titanium (NbTi) cables that become superconducting below a temperature of 10 K. The LHC is operating at 1.9 K. This temperature is reached by pumping superfluid helium into the magnet system.

3.2 The ATLAS Detector

One of the seven particle detector experiments at the LHC is the ATLAS (A Toroidal LHC ApparatuS) Experiment, centred at a LHC collision point. It's size is 46m in length and 25m in diameter, and it has been designed to measure the paths and energies of the particles emerging from the collisions. The ATLAS Experiment consists of a succession of concentric sub-systems as shown in Figure 3.2, each being sensitive to different types of particles produced in the collisions [27] [28]. The several components are described below.

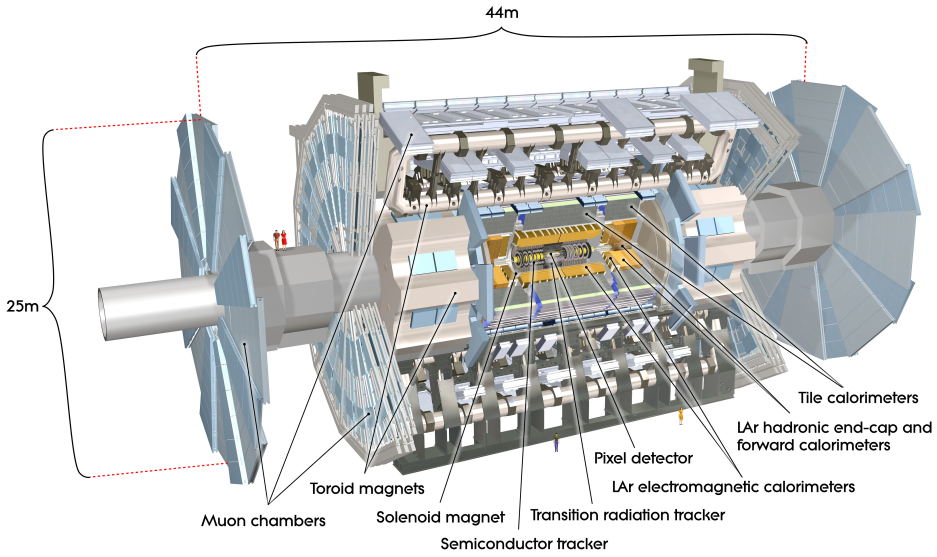

Figure 3.2: Schematic layout of the ATLAS detector [29].

3.2.1 Coordinate system

The interaction point is the origin of a right-handed coordinate system. The z-axis points along the beam line, while the positive x-axis points from the interactions point to the center of the LHC and the positive y-axis points upward to the earths surface. Hence the x-y-plane is perpendicular to the beam line. It is denoted as the transverse plane, thus particle momenta measured in the transverse plane are denoted as the transverse momenta $p_{\mathrm{T}} = \sqrt{p_x^2 + p_y^2}$ and the transverse energy E_{T} amounts to $E_{\mathrm{T}} = \sqrt{m^2 + p_{\mathrm{T}}^2}$. The transverse plane can be described in terms of the azimuthal angle ϕ, measured from the x-axis around the beam, and the radial dimension r, which measures the distance from the beam line. The polar angle ϕ is defined as the angle from the positive z-axis and is often described in terms of pseudorapidity

$$\eta = -\ln \tan \frac{\theta}{2}. \tag{3.1}$$

The distance ΔR in $\eta - \psi$-space is denoted as

$$\Delta R = \sqrt{\Delta\eta^2 + \Delta\phi^2}. \tag{3.2}$$

3.2.2 Inner Detector

With the Inner Detector (ID) the positions of the charged particles are measured. A magnetic field of 2 T provided by the solenoid magnet is located around the ID. Under the influence of the magnetic field the trajectories of charged particle are being bent, and can thus be identified as charged particles. The ID is composed of a pixel detector, a semiconductor tracker and a transition radiation tracker, providing a precise momentum and vertex measurement. The pixel detector lies closest to the interaction point. It consists of 4 layers of silicon pixel detectors enabling a measurement of the particle tracks with high spacial resolution, which is important to identify hadrons containing b-quarks. The semiconductor tracker, which is composed of silicon strips assembled inline with the beam axis, surrounds the pixel detector and provides a precise tracking. The outer part of the ID uses straw drift tubes and transition radiation tracker for momentum measurement. By detecting and tracking transition radiation photons it enables an improvement of the identification efficiency for electrons.

3.2.3 Calorimeter System

The calorimeter system is composed of the electromagnetic calorimeter (ECAL), which measures the energies of electrons and photons, and the hadronic calorimeter (HCAL), which measures the energies of hadrons. Within the sampling calorimeter incident particles produce showers of energy, only a fraction of which is measured actively by detector sensors. The energy of the complete shower can be deduced from the observed energy. The ECAL is a liquid-argon (LAr) detector with a specific geometry that enables complete ϕ coverage as well as fast readout. It is subdivided into three radial sections with different η-ϕ granularities. The first layer enables fine segmentation in η. The second one provides the bulk of the energy measurement with a fine segmentation in both η and ϕ. The third layer has a coarser granularity and adds more depth to the calorimeter. The ECAL covers the pseudorapidity range $|\eta| < 3.2$. The HCAL consists of the Tile calorimeter and the LAr hadronic hadronic end-cap calorimeter. The Tile calorimeter covers $|\eta| < 1.7$ The scintillator-tile calorimeter is divided into a barrel and two extended barrel cylinders. In the range $1.5 < |\eta| < 3.2$, the end-caps, LAr is used for the HCAL. The LAr forward calorimeters enable both electromagnetic and hadronic energy measurements covering the pseudorapidity range to $|\eta| = 4.9$.

3.2.4 Muon Spectrometer

As muons pass through the ID and the calorimeter system nearly undetected, a muon spectrometer is needed to identify and measure the momenta of muons. It consists of a set of 1200 chambers measuring the tracks of the muons with high spacial resolution and a set of triggering chambers with precise time resolution. They are located in a magnetic field provided by three toroidal magnets. The positions of the muons are

measured in chambers assembled in three layers around the beam axis in the barrel region, while in the transition and end-cap region the chambers are perpendicular to the beam. Monitored Drift Tubes are used to measure the muon positions, with exception of the range $2 < |\eta| < 2.7$, where Cathode Strip Chambers are used. In addition to tracking, there are also muon chambers used for triggering, as explained in the subsection below.

3.2.5 Trigger System

Many processes that contain interesting physics have a pretty small cross section. Thus a large number of brunch crossings, with an average of 30 MHz, is necessary to produce a considerable amount of these rare events. However, ATLAS can only save a small fraction, around 1000 events per second, of the recorded events. Real-time event selection is performed by the trigger system to decrease the number of recorded events. The trigger system is designed to dismiss the events not containing interesting physics. The level one trigger (L1) lowers the initial event rate to 100 kHz. It is based on calorimeter clustering and track finding in the Muon Spectrometer. It defines so called regions of interests within a decision time of 2.5 μs. Due to this extremely short decision time, the reconstruction algorithms are implemented directly in hardware. The regions of interests are then used as input for the software-based high-level trigger (HLT), where the complete event information of the ATLAS detector is analyzed by running eligible selection algorithms. The event rate is further reduced by the HLT to 1 kHz within a decision time of around 22 ms. Aimed at different several signatures, different combinations of L1 triggers and HLTs are used.

3.2.6 Pile-up

A variety of interactions can occur within one bunch-crossing, which are referred to as pile-up. Several subsystems of the ATLAS experiment have sensitivity windows longer than 25ns, the time between two bunch crossing, thus every physics object is affected with pile-up in a certain way. Pile-up influences for example the energy contributions in jets and the reconstruction of background. As with higher center-of-mass energy the pile-up increases, it is crucial to understand this background and to be capable of modeling it in perfoming analysis in ATLAS. The pile-up background has five contributions:

- In-time pile up: collisions arising in the same bunch crossing as the collision of interest.
- Out-of-time pile-up: collisions arising in bunch-crossing right before and after the collision of interest. With a sensitivity window longer than the bunch crossing time these collisions can influence the detection of the collision of interest.

- Cavern background: the gas of neutrons and photons that occurs in the cavern while the LHC is running, resulting mostly in hits in the MS.
- Beam halo events: protons from a bunch moving against an up-stream collimator, generating sprays of muons that run approximately parallel to the beam line.
- Beam gas events: protons colliding with residual gas inside the beam-pipe.

The methods used to perform pile-up corrections are described in [30].

4 Monte Carlo Simulation

In particle physics collisions can be simulated using Monte Carlo (MC) generators. The probability density functions of events from a certain process can be calculated from theory, enabling to estimate signal and background processes and to compare theoretical predictions to data. The Monte Carlo method refers to computational algorithms that use random numbers to obtain numerical quantities. The algorithms are based on repeated random sampling. In the following an overview is given on how Monte Carlo based methods are used in particle physics.

4.1 Monte Carlo Event Generation

Theoretical predictions for particle physics processes can be reproduced through Monte Carlo event generators. These generators produce hypothetical events with the distribution predicted by theory. The underlying theory for the *pp* collisions within the LHC is explained by QCD, which describes the strong interaction between quarks and gluon precisely at high energy. At low energy, one needs different models, due to the gluons coupling to each other, which cannot be solved with a perturbation approach anymore. A model that is not relying on perturbation theory is for example Lattice QCD [31].

The workflow of Monte Carlo generators is divided into separate subtasks. In order to fully describe an event, the following components are considered [32] [33]:

- **Hard scattering matrix element $\mathcal{M}$**

  They define the process which is being studied as its cross section is proportional to $|\mathcal{M}|^2$.

- **Structure functions**

  They are partition density functions that describe the momentum distribution of the partons, the protons components.

- **Final state radiation**

  It is possible that partons in the final state might radiate. This perturbative radiation is the dominant mechanism for structuring jets at high energies.

- **Initial state radiation**

Also the incoming partons could radiate before the interaction. This is the source of additional jets.

- **Beam jets**

  The assumption is made that only one parton from each incoming hadron participates in the hard interaction as well as in the initial state showering. The remaining partons produce the beam jets located along the directions of the original incoming hadrons.

- **Fragmentation and decays**

  A direct observation of partons is not possible, as they hadronize, forming stable hadrons. This leads to the jet-characteristic of partons.

The structuring above is very schematic and not distinct as for example an additional gluon in the final state can be included in the matrix element or in the final state radiation. Therefore, it is crucial to consistently join the different descriptions in order to avoid double counting. For that reason the Monte Carlo program is divided into two different approaches: using either parton showers or matrix elements.

In terms of the parton shower approach, in general only the lowest order matrix elements are implemented. Initial and final state radiation are added as showers, which are assumed to be universal, meaning that the shower evolution must only depend on the gross features of the hard scattering, not upon its details. These features contain energies and flavours of incoming and outgoing partons. After adding beam jets and fragmentation models, the total amount of phenomenological crucial features of hadron collisions is accounted for in the event modelling.

The emphasis of the matrix-element approach lies on the use of precise higher-order matrix elements. The analytic framework used in this approach is more complex and has a more advanced phase space generation. As the precision aspect is crucial for the matrix calculation itself and the efficient selection of kinematic variables, it is not manageable to attach a generic notion of parton shower. For that reason usually only a small amount of partons is generated. Furthermore, fragmentation and beam jets become less interesting, as most modern fragmentation modes are adjusted to be attached at the end of the parton shower evolution.

Using the parton shower and matrix element approach one can benefit from the advantages of each of them. One can obtain an accurate description of well distinct, hard partons from matrix element generators together with a good approximation of various soft, collinear partons provided by parton shower generators.

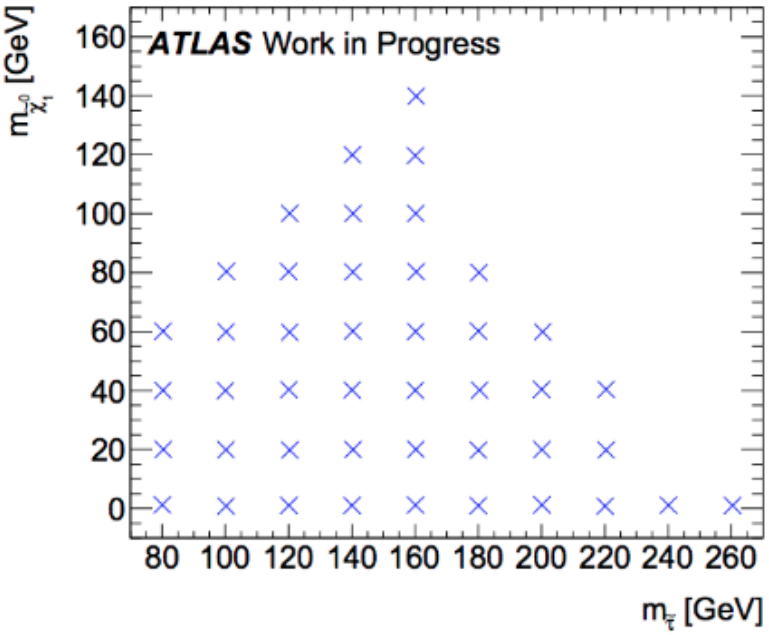

Figure 4.1: Signal grid for the direct stau production in the HadHad-channel, taken from [34]

4.2 Processes included in the analysis

4.2.1 Monte Carlo signal samples

The signal process in this analysis is the direct stau production. In Monte Carlo simulations the signal samples are produced for different masses of stau and neutralino, respectively, also refered to as mass points. At tree level the process is simulated with MadGraph and the parton shower is added by PYTHIA8. The signal grid is composed of 44 mass points that range from 80 GeV to 260 GeV in stau mass and from 0 GeV to 140 GeV in neutralino mass. The signal grid is illustrated in Figure 4.1. Two subsets are simulated for each mass point accounting for the two staus, denoted as $\bar{\tau}_1$ and $\bar{\tau}_2$. The two subsets have different cross-sections, however they are merged together into one sample, due to the fact that they are mass degenerate. All samples are weighted to an integrated luminosity of 36.1 fb^{-1}.

4.2.2 Monte Carlo background samples

The relevant background processes for the direct stau production are the following:

- **W+jets**

This background covers all events in which a W-boson is produced together with one or more jets. This process is relevant for the HadHad-channel. When considering the LepHad-channel, the W-boson either decays directly into a light lepton, that is an electron or muon, or into a tau, which decays leptonically. Also in this case the jet fakes the hadronic tau. The Monte Carlo generator used for the simulation of W+jets is Sherpa2.2.1. The samples are listed in Appendix I.

The W+jets events that contribute to the background for the direct stau production, are the ones that contain two taus, one real tau from the W-boson decay and one jet, which fakes a tau. The misidentification rate of a jet as a tau is very low, leaving only a small amount of Monte Carlo events that contribute to the background. Because most of the events cannot be used for the background modelling, the statistical uncertainty becomes large. The reweighting method presented in this thesis, called Tau Promotion, targets this problem, and provides an approach for the improvement of the statistical uncertainty. The Tau Promotion method is described in chapter 6.

- **Z+jets**

  The Z+jets background is composed of events, where a Z-boson is produced in association with a certain number of jets. For the HadHad-channel mostly Z-bosons decaying into two hadronic decaying taus are relevant, whereas for the LepHad-channel one of the taus decays hadronically and the other one leptonically. Z+jets events are produced by the Monte Carlo generator Sherpa 2.2.1.

- **Dibosonic Events**

  In dibosonic processes two electroweak bosons are produced. Events that leave the same signature as the signal process are for example $ZZ \to \tau\tau\mu\mu$ and $WW \to \tau\nu\tau\nu$, which form an important irreducible background. Dibosonic events are also generated with Sherpa 2.2.1.

- **Processes containing Top Quarks**

  Background events that contain top quarks are composed of top quark pair production ($t\bar{t}$), single top production and top pair production with an associated boson radiation ($t\bar{t}V$). The latter, however, has only a small contribution. Furthermore the production of a top quark together with a Higgs boson is neglected for this analysis. As top quarks mostly decay into a bottom quark and a W-boson, which subsequently decays into taus, light leptons or quarks, this background can be rejected quite well by requiring events that contain no b-jets. This requirement is referred to as a b-jet veto. Events containing top quarks are simulated by the POWHEG event generator, except $t\bar{t}V$ events, where MadGraph is used. The parton shower is added by PYTHIA for all events.

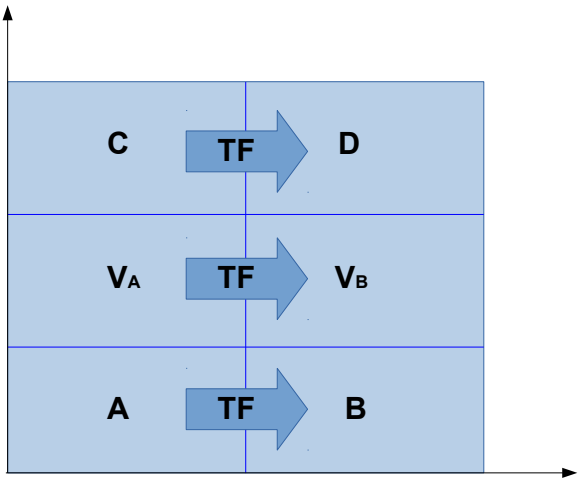

Figure 4.2: Illustration of the ABCD method with control regions A, B and C, signal region D, and two validation regions V_A and V_B. All regions are othogonal to each other.

- **QCD Multijet Processes**

  For the background, that consists of QCD Multijet Processes, there is no estimation via simulation available. Therefore different approaches are needed in order to estimate the contribution of this background. One technique is the so called ABCD-method. The concept of this method, is that two uncorrelated variables span a phase space, which is then divided into four region: One signal region D, and three control regions A, B and C. It is assumed, that the control regions do not contain any signal. Hence when subtracting the Monte Carlo estimation of all the other backgrounds from data, the remaining contribution has to be the QCD background. A transfer factor is calculated from the differences of observed data and Monte Carlo simulation in the regions A and B. Under the assumption that the relation of region B to region A is equivalent to the relation of D to C, the same transfer factor is applied to region C, giving an estimate for the signal region D. Additionaly, one can introduce two validation regions, V_A and V_B, in order to validate this method, as it is illustrated in Figure 4.2 The transfer factor is applied to region V_A in order to get an estimate for region V_B, which is then compared to the real difference of data to Monte Carlo in region V_B.

5 Object and Event Selection

In the following the objects, selection criteria and kinematic observables in the analysis will be introduced. Figure 5.1 shows the different signatures of particle crossing the detector. Each signature will be explained in more detail below. In addition object definitions in the context of the Tau-Promotion method are illustrated.

5.1 Object Definitions

- **Electrons**

  Electrons are reconstructed by using information of both the ECAL clusters and the ID, as electrons leave a track in the ID and initiate an electromagnetic shower within the ECAL. The ECAL absorbs nearly all of the electrons energy before it reaches the HCAL. To ensure that the electrons originate from primary vertex, signal electrons must satisfy $|d_0/\sigma(d_0)| < 5$ and $|z_0 \sin\theta| < 0.5$mm, where d_0 is the smallest distance of the track to the beam line, $|\sigma(d_0)| < 5$ the uncertainty on d_0 and z_0 is the distance between the primary vertex and the point, at which d_0 is measured, projected onto the z-axis [36]. Electrons are identified with a likelihood based method, that makes use of several characteristics of the reconstructed objects. Electron candidates must satisfy the very loose identification criteria as described in [37].

- **Muons**

  As mentioned earlier, Muons traverse the complete ATLAS detector, due to the fact that muons are minimally ionizing, hence hardly interacting with the detector material. All other interacting particles are stopped before they reach the MS, thus muons are identified by the fact that they hit the MS. Muon reconstruction is performed by matching tracks in the ID to tracks in the MS. For identifying isolated muons the requirement is set that the energy of the reconstructed tracks and clusters in vicinity of the reconstructed muon must not exceed a certain value. By applying this isolation requirement muons produced from background processes are suppressed. Possible background processes are semileptonic hadron decays and misidentified jets. Muons from secondary vertices are suppressed by requiring $|d_0/\sigma(d_0)| < 3$ and $|z_0 \sin\theta| < 0.5$mm.

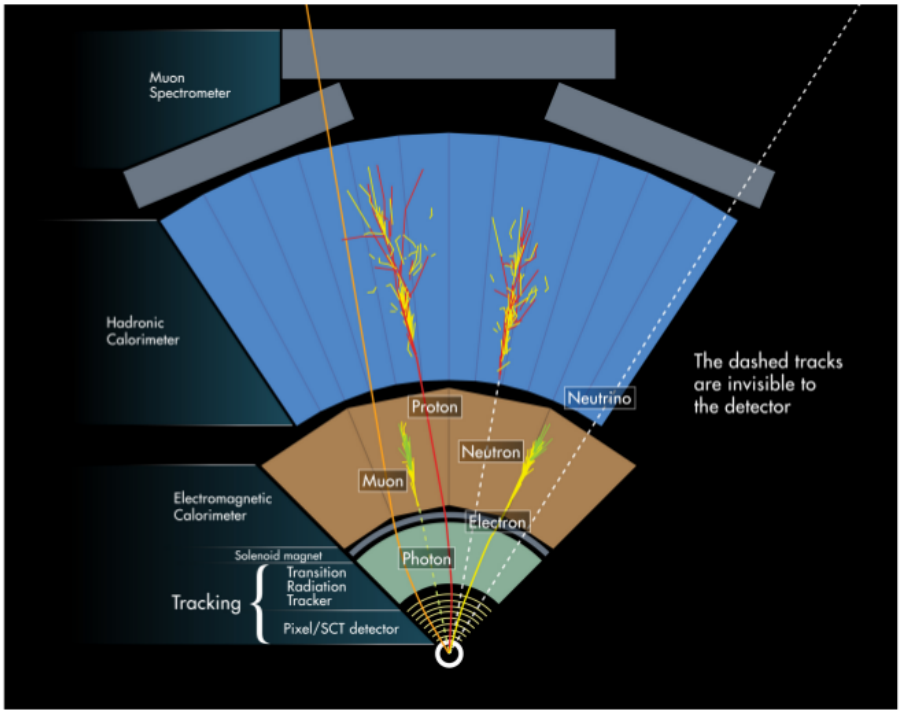

Figure 5.1: Signatures of various particles in the different layers of the ATLAS detector. [35]

- **Jets**

  Jets are cascades of colorless hadrons originating from high-energy colored particles, quarks and gluons, which undergo hadronisation. Measuring the energy and direction of a jet provides information about the initial quarks or gluons that took part in the process of interest. The shape of a jet in the detector resembles the shape of a cone. Jets are reconstructed by making use of the four-momenta of the particles measured by using three-dimensional topological calorimeter cell clusters and the anti-k_T [38] with the radius parameter R chosen to be 0.4. Additionally the measurement of the energy deposit in the cells is calibrated for each cell, as the detector performance for electromagnetic and hadronic particles differs. The jet energy scale calibration (JES) relates the reconstructed jet energy to the truth energy. JES contains correction of the four-momentum of the jet to make it point to the original interaction point, pile-up reweighing and a correction of the detector response based on Monte Carlo simulations [39] [40].

- **Tau leptons**

  Tau leptons cannot be detected directly as they are very massive (1.777 GeV) and have a short decay length (87 μm), thus decaying before reaching the active regions of the ATLAS detector. The decay is either leptonic or hadronic, so that the decay products of the tau leptons can be detected in the ECAL or HCAL, respectively. Only hadronic tau lepton decay modes, contributing with 65% to all possible decays, are reconstructed as a tau lepton, whereas leptonic decays are considered as light signal leptons. The bulk of the hadronic decay products contains either one or three charged pions, referred to as 1-prong and 3-prong, respectively. The visible part of the tau lepton consists of the neutral and charged hadrons originating from the tau lepton decay, and is denoted as $\tau_{\text{had-vis}}$. Most of the background processes to hadronic tau lepton decays originate from jets of energetic hadrons. This background is present at trigger level, referred to as online, as well as during the event reconstruction, referred to as offline. In order to distinguish the candidates from jets, discriminating variables based on the narrow shower in the calorimeter, the explicit number of tracks and the displaced tau lepton decay vertex are used. Another background for $\tau_{\text{had-vis}}$ that contain one charged hadron, namely 1-prong, are electrons, which will be revisited shortly. Jets seeding tau candidates are required to have p_{T} >10 GeV and $|\eta| < 2.5$. In the transition region between barrel and forward calorimeters $1.37 < |\eta| < 1.52$ tau candidates are vetoed. The tau lepton vertex is chosen as the candidate track vertex, which has the largest fraction of momentum from tracks connected with the jet ($\Delta < 0.2$). The tracks need to fulfil requirements on the number of hits in the detector and have $P_{\text{T}} > 1$GeV. Further requirements are $|d_0| < 1$mm and $z_0 \sin\theta < 1.5$mm. Afterwards the tracks are associated to core ($0 < \Delta\text{R} < 0.2$) and isolation ($0.2 < \Delta\text{R} < 0.4$) regions around the tau candidate. The calculation of the η-ϕ-direction of the tau candidate is done using the vectorial sum of the

topological calorimeter cell clusters within $\Delta R < 0.2$ of the seed jet barycenter by using the tau vertex as the origin. The energy deposition measured in the detector is corrected using a tau-specific energy calibration as explained in [41].

The tau identification algorithm uses Boosted Decision Tree (BDT) based methods [42] and is designed to reject backgrounds from jets originating from quarks and gluons as described in [41] and [43]. Three working points are provided, denoted as loose, medium and tight. These are associated to different tau identification efficiency values, with the target efficiency being 0.6, 0.55 and 0.45 for generated 1-prong loose, medium and tight working point, and 0.5, 0.4 and 0.3 for the associated 3-prong target efficiencies. This is the case for the offline reconstruction of tau leptons. For the trigger selection an analogous procedure is performed online using a BDT. However, the identification efficiencies for the 1-prong and 3-prong tau leptons are 0.95 and 0.7, respectively.

In order to suppress the background from electrons, 1-prong tau candidates are rejected offline, if they are within a distance $\Delta R < 0.4$ of a reconstructed electron, which passes a very loose working point [43]. An online discrimination of tau leptons and electrons is not available. For this thesis 1-prong and 3-prong tau leptons are used, which fulfil $p_T > 20\text{GeV}$ and $|\eta| < 2.5$ and their charge has to be +1 or 1 in units of the elementary electric charge e.

- $\boldsymbol{E_{\mathrm{T}}^{\mathrm{miss}}}$

  Momentum conservation in the plane transverse to the beam imposes that the transverse momentum of the collision products should sum to zero. An imbalance is referred to as missing transverse momentum, denoted $E_{\mathrm{T}}^{\mathrm{miss}}$, and is a possible indication for weakly-interacting, stable particles in the final state. The only SM particles, that cause $E_{\mathrm{T}}^{\mathrm{miss}}$, are neutrinos. However, when considering theories beyond the SM, $E_{\mathrm{T}}^{\mathrm{miss}}$ can be a signature for new particles. In the MSSM, for instance, the LSP $\tilde{\chi}_1^0$ leaves missing transverse momentum in the detector. Fake $E_{\mathrm{T}}^{\mathrm{miss}}$ can arise from interacting SM particles that either escape the acceptance of the detector, are badly reconstructed or are not reconstructed at all.

  $E_{\mathrm{T}}^{\mathrm{miss}}$ is defined as the negative vector sum of the transverse momenta of all reconstructed physics objects and includes a track-based soft term [44] [45]. The soft term contains reconstructed tracks pointing to the primary vertex that are not associated to any of the reconstructed physics objects.

5.2 Overlap Removal

As the reconstruction procedures run independently from each other, processing the same data, it is possible that the same detector signature is reconstructed as two different physics objects. Overlap removal is an algorithm designed to resolve these

ambiguities as it decides which object should be kept and which should be removed. The algorithm checks whether two reconstructed objects lie within a cone of certain size $\Delta R = \sqrt{\Delta\eta^2 + \Delta\phi^2}$, that depends on the objects that are compared. For the case that more than two objects lie within the cone, the routine is repeated.

5.3 Kinematic Variables

- **Effective mass**

  The effective mass m_{eff} is defined as

$$m_{\text{eff}} = \sum_{\tau} |\mathbf{p}_{\text{T}}| + E_{\text{T}}^{\text{miss}} \tag{5.1}$$

  where the sum of the transverse momenta of the tau leptons is added to the missing transverse energy.

- **Invariant mass**

  The part of the total mass of an object that is independent of the overall motion of the system is called invariant mass. The invariant mass of two particles with four-momenta $p_{1,2}$, $E_{1,2}$ and three-momenta $\mathbf{p}_{1,2}$ is computed as:

$$m_{\text{inv}}^2 = (p_1 + p_2)^2 = 2m^2 + 2(E_1 E_2 - \mathbf{p}_1 \cdot \mathbf{p}_2) \tag{5.2}$$

  In collider experiments, the invariant mass is often defined in terms of the azimuthal angle ϕ and pseudorapidity η. For massless or highly relativistic particles ($E \gg m$) the invariant mass then becomes:

$$m_{\text{inv}} = 2p_{\text{T}1}p_{\text{T}2}(\cosh(\eta_1 - \eta_2) - \cos(\phi_1 - \phi_2)) \tag{5.3}$$

- **Pseudorapidity**

  A variable that is related to the angle between the x-y plane and the direction of the direction of the emitted particles originating from the collision is the rapidity y, defined as:

$$y = \frac{1}{2}\ln\left(\frac{E + p_{\text{T}}}{E - p_{\text{T}}}\right) \tag{5.4}$$

For a particle moving perpendicular to the beam direction, the rapidity will be close to zero, whereas for a particle moving alongside the beam axis y tends to $\pm\infty$.

However, it may be difficult to measure the rapidity for highly relativistic particles, as one needs both the energy and the total momentum. A variable which defines a similar quantity as y, but is easier to measure for highly energetic particles, is called pseudorapidity η. It is defined as

$$\eta = -\ln \tan \frac{\theta}{2}, \tag{5.5}$$

with θ being the angle between the particles trajectory and the beam pipe. Especially in hadron colliders such as the LHC, where due to the composition of the colliding protons the interactions rarely have their center-of-mass frame coincident with the detector rest frame, the estimation of η is far quicker than that of y.

- **Transverse mass**

  If a particle in the collisions decays into two physics objects, where one of them is invisible, it is not possible to reconstruct the original mass M from the mass of the decay products. The transverse mass m_T gives a lower bound on M, calculated as

$$m_{\mathrm{T}}^2 = 2p_{\mathrm{T}1}p_{\mathrm{T}2}(1 - \cos\Delta\phi) \leq M^2, \tag{5.6}$$

  where $p_{\mathrm{T}1}$ and $p_{\mathrm{T}2}$ are the absolute values of the transverse momentum of particle a and b, respectively, and $\Delta\phi = \phi_b\phi_a$ is the angle in the transverse plane of the reconstructed particle and $E_{\mathrm{T}}^{\mathrm{miss}}$. This procedure was used for the measurement of the W -boson mass [46].

- **Stransverse mass**

  The stransverse mass is used to bound masses of an unseen pair of particles which are assumed to have decayed semi-invisibly into particles which were seen. There are two parallel decay chains 1 and 2, each of them containing one reconstructed object $\mathrm{a}_{1,2}$ and one invinsible particle $b_{1,2}$. The contributions from the invisible particles to $E_{\mathrm{T}}^{\mathrm{miss}}$ is not known. For that reason $m_{\mathrm{T}}(a_1, b_1)$ and $m_{\mathrm{T}}(a_2, b_2)$ are computed for all possibilities in order to distribute $E_{\mathrm{T}}^{\mathrm{miss}}$ on $p_{\mathrm{T}}(b_1)$ and $p_{\mathrm{T}}(b_2)$. The stransverse mass gives an upper bound on M by choosing the larger minimization of $m_{\mathrm{T}}(a_1, b_1)$ and $m_{\mathrm{T}}(a_2, b_2)$ over all possible distributions:

$$m_{\mathrm{T2}}(a_1, a_2) = \min_{\mathbf{p}_{\mathrm{T}}(b_1)+\mathbf{p}_{\mathrm{T}}(b_2)=E_{\mathrm{T}}^{\mathrm{miss}}} \left[\max\{m_{\mathrm{T}}^2(a_1, b_1), m_{\mathrm{T}}^2(a_2, b_2)\}\right] \leq M^2 \qquad (5.7)$$

In the case of direct stau production, two neutralinos are produced which contribute to $E_{\mathrm{T}}^{\mathrm{miss}}$, which cannot be distinguished. In the calculation of the stransverse mass, the mass of the neutralinos as well as the mass of the tau lepton are neglected.

5.4 Trigger

In order to be able to handle the huge amount of data that is produced through collisions at the LHC, only collisions are recorded that store a reasonable amount of interesting event. The selection is performed by triggers as mentioned in chapter 3.

For the search of direct pair production of two staus, two triggers are used: the assymetric tau trigger [1] and the ditau+MET trigger [2]. The assymetric tau trigger fires at events, where the two leading taus have a large difference in their transverse momenta. Furthermore the two taus need to pass the online medium requirement. The online thresholds for the momenta of the taus for this trigger are 80 GeV for the leading tau and 50 GeV for the next-to-leading tau. As the trigger efficiency reaches its optimal value with higher values of $p_{\mathrm{T}}(\tau)$, which is described by the so called turn-on curve, the offline values for the assymetric tau trigger are 95 GeV and 65 GeV for the two taus, respectively. The ditau+MET trigger selects events with two medium taus and missing transverse momentum above a particular threshold. For the transverse momenta of the two taus, the online thresholds are 35 GeV and 25 GeV, while for the missing transverse momentum the online threshold lies at 50 GeV. The offline thresholds for the momenta of the two taus are 50 GeV and 40 GeV. For the missing transverse momentum the turn-on curve is more shallow than for the transverse momentum, hence the plateu-region is reached at higher values. For that reason the offline threshold for the missing transverse momentum has a relatively high value with 150 GeV.

[1] HLT_tau80_medium1_tracktwo_L1TAU60_tau50_medium1_tracktwo_L1TAU12
[2] HLT_tau35_medium1_tracktwo_tau25_medium1_tracktwo_xe50

6 Improvement of the W+jets Monte Carlo statistics

6.1 Method

The Tau Promotion method was initially developed to reduce the statistical uncertainties on the W+jets background estimation for the direct production of a scalar tau pair, but it can be generally used in searches for final states, that contain two hadronically decaying taus. For these searches the W+jets events that contribute to the background consist of one real tau from the W boson decay and at least one object, which is misidentified as a tau. As the misidentification rate of a jet as a tau is very low, most Monte Carlo events do not contribute to the W+jets background. This leads to large statistical fluctuations due to the small amount of events that can be used for the background modelling.

As earlier mentioned, the tau candidates are further classified into loose, medium or tight, provided that they fulfil the criteria. The pool the tau candidates are selected from is referred to as container taus. Tau candidates, which have to fulfil the requirements described in section 5.1, are labeled as container taus, if they pass the additional requirements of $p_{\mathrm{T}} > 20$ GeV, $\eta < 2.5$, as well as leaving one track (1-prong) or three tracks (3-prong) in the calorimeter. The idea behind the Tau Promotion method is to randomly pick one container tau, and purposely misidentify it to loose, medium or tight quality, depending on which working point is used in the analysis. In the following this deliberate misidentification is referred to as "promotion" of the tau leptons. Container taus are required to fulfil certain criteria in order to be considered as a promotion candidate as they are not allowed to be classified as the working point used in the analysis nor are they allowed to be real taus. These criteria are quite straightforward, as one only considers events, that would be cut out by applying a selection requiring at least two taus.

Real taus, that are not reconstructed as taus, could also be considered for promotion. Events that contain real taus that are reconstructed as jets and, thus, do not have two tau leptons in the final state, would then have one real tau after promotion. If such an event does not have a fake tau and has a container tau eligible for promotion, this container tau could then also be promoted, so that the event would contribute to the background. For the promotion of jets one needs to find an equivalent fake efficiency for real taus, that are not reconstructed, in order to compute the reweghting factor.

The promotion of jets has not been considered in this thesis.

Identifying fake container taus is done using truth-matching. In this procedure a truth-sample is used which simulates the same process as the $W \to \tau\nu$ datasets itemized in Appendix I. In these samples the information on the particle decay chains and their true identities is available. After matching each container tau to a true tau in the truth sample, a candidate tau is denoted as real tau if it corresponds to a true tau within ΔR, and fake if it does not.

Figure 6.1 illustrates the scheme of the Tau Promotion method. After a container tau has been promoted, an event that had one real tau, originating from the W-boson decay, has an additional fake tau. This event can now be used for the modelling of the W+jets background in the analysis. Thus more events contribute to the background estimation leading to the reduction of the statistical uncertainties. As the estimated contribution of events to the background must not get larger despite the additional contribution of events containing promoted taus, the events need to be reweighted to the initial contribution. The reweighting factor is computed from the fake efficiency. In this thesis the fake efficiency was measured using two approaches: measurement in bins in the $E_{\mathrm{T}}^{\mathrm{miss}}$-$p_{\mathrm{T}}(\tau)$-plane and in bins in the $\eta(\tau)$-$p_{\mathrm{T}}(\tau)$-plane, both from Monte Carlo simulation. These two approaches were compared considering the accuracy of the reweighting, the results are shown in the next sections. The fake efficiency differs strongly for 1-prong and 3-prong taus, as it is shown in Figure 6.3 and Figure 6.4, and is thus measured separately for the two cases. Assuming the working point for the taus used in the analysis is medium, then the container taus are promoted to medium quality. So when there are n non-real container taus of which k fulfil the criteria for medium quality, there will be $k+1$ medium taus after promotion. The probability for k fake medium taus and $n-k$ fake non-medium container taus can be calculated by:

$$P(k) = \epsilon^k (1-\epsilon)^{n-k} \binom{n}{k} \tag{6.1}$$

After a container tau is promoted this binomial probability distribution becomes:

$$P(k+1) = \epsilon^{k+1} (1-\epsilon)^{n-k-1} \binom{n}{k+1} \tag{6.2}$$

A reweighting factor is necessary in order to get the same sum of weights after promotion as the nominal distribution, which leads to the following equation:

$$P(k+1) = P(k) \cdot \omega \tag{6.3}$$

which gives a reweghting factor of

$$\omega = \frac{P(k+1)}{P(k)} = \frac{\epsilon}{1-\epsilon} \cdot \frac{n-k}{k+1} \tag{6.4}$$

Eventually ω is dependent on the fake efficiency ϵ and a combinatorical factor C, that can be computed as

$$C = \frac{\text{number of non-medium fake taus before promotion}}{\text{number of medium fake taus after promotion}} \tag{6.5}$$

giving a reweighting factor of

$$\omega = \frac{\epsilon}{1-\epsilon} \cdot C. \tag{6.6}$$

For events without container taus that fulfill the requirements to be selected for promotion, the reweighting factor becomes equal to zero, so that these events are not accounted for twice in the background contribution.

The $W \to \tau\nu$ Monte Carlo samples, listed in Appendix I, are sorted by $p_{\mathrm{T}}(W)$ and the applied filter, as shown in Table 6.1. Figure 6.2 shows the contribution of the $W \to \tau\nu$-samples sorted by $p_{\mathrm{T}}(W)$.

DSID	$p_{\mathrm{T}}(W)$	filter
364184	0-70	light-jet
364185	0-70	c-jet
364186	0-70	b-jet
364187	70-140	light-jet
364188	70-140	c-jet
364189	70-140	b-jet
364190	140-280	light-jet
364191	140-280	c-jet
364192	140-280	b-jet
364193	280-500	light-jet
364194	280-500	c-jet
364195	280-500	b-jet
364196	500-1000	-
364197	>1000	-

Table 6.1: $W \to \tau\nu$ Monte Carlo samples, sorted by $p_{\mathrm{T}}(W)$ and applied filter.

6.2 Studies on reweighting improvement

In this section the container taus are promoted to the medium woking point, as that is the working point used in the analysis for the search for direct production of scalar tau leptons. The results for the promotion of container taus to both loose and tight working point are shown in the next section.

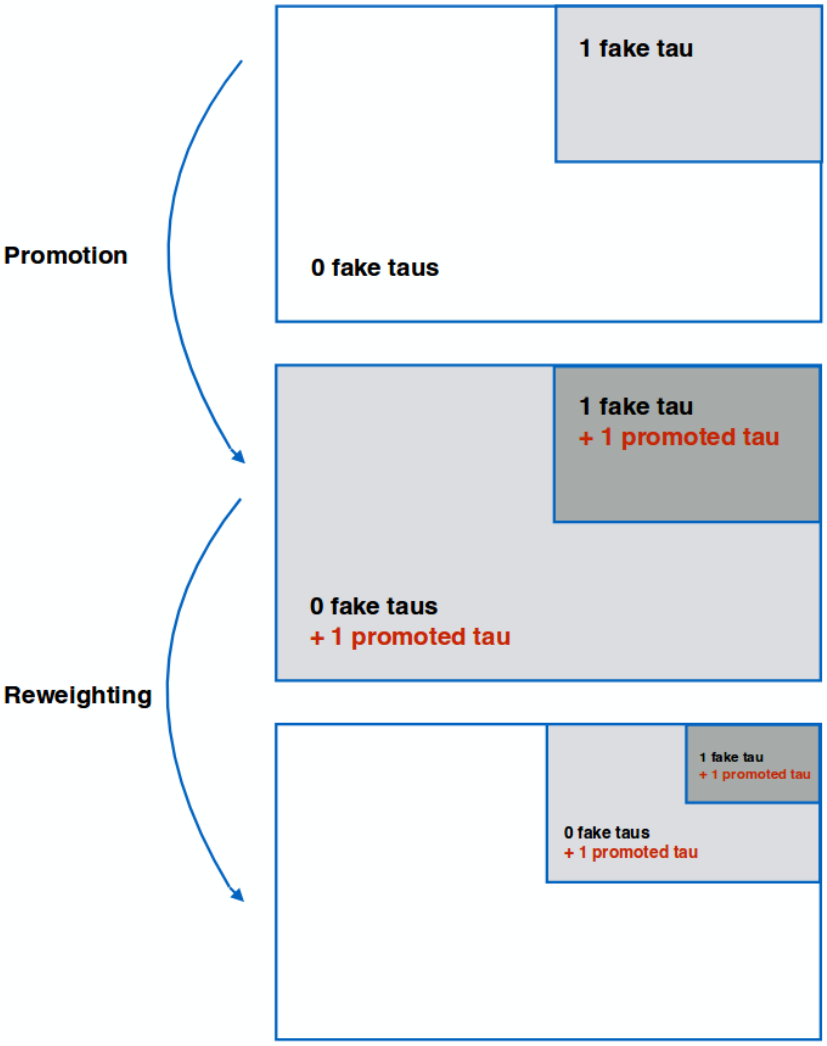

Figure 6.1: Schematic illustration of the Tau Promotion method: the nominal $W \to \tau\nu$-sample that contributes to a final state with two tau leptons has one real tau from the W-boson decay, which is neglected here, and one fake tau originating from a jet. After container taus in the eligible events are promoted, these events that did not contain a fake tau also contain one fake tau and thus, contribute to the background estimation. A reweighting is applied in order to obtain the same contribution of the total background as the nominal sample.

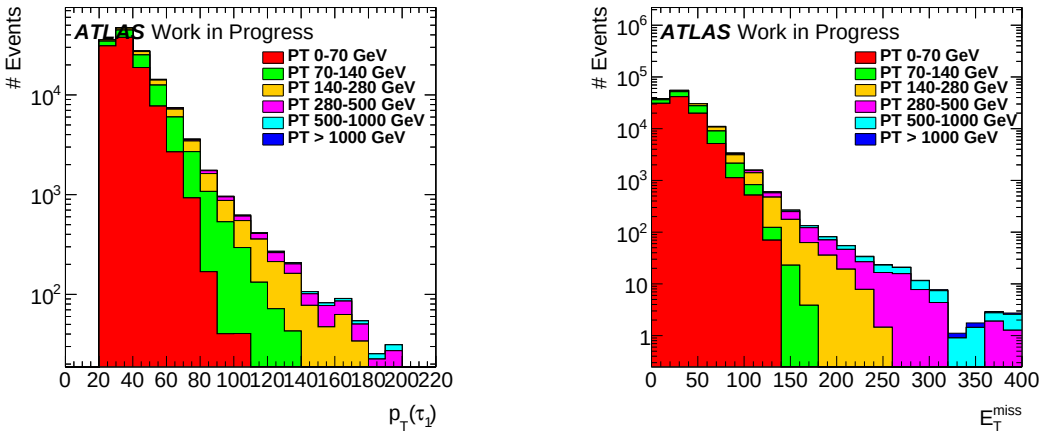

Figure 6.2: The stacked distributions of the $W \to \tau\nu$-samples sorted by $p_{\mathrm{T}}(W)$ containing at least two tau leptons of medium working point with opposite sign charge.

6.2.1 Measurement of fake efficiency in $E_{\mathrm{T}}^{\mathrm{miss}}$-$p_{\mathrm{T}}(\tau)$-plane

As the reweighting procedure depends mostly on the fake efficiency, an accurate measurement of the fake efficiency is necessary. Here, the fake efficiency is assumed to be narrow in certain intervals and is measured in bins. One possibility to measure the fake efficiency is using the missing transverse momentum and the transverse momentum of the tau, which is shown in Figure 6.3 for 1-prong, and Figure 6.4 for 3-prong.

The arrangement of the separate bins is crucial as the measurement of the fake efficiency gets more precise with a narrow binning, however, the statistical uncertainty gets larger. Table 6.2 shows the event yields weighted to an integrated luminosity of 36.1 fb^{-1}, that were obtained when using a common binning for all W+jets Monte Carlo slices. For the same procedure, the unweighted event yields are listed in Table 6.3 in order to observe how many more events contribute to the background after the Tau Promotion compared to the nominal sample.

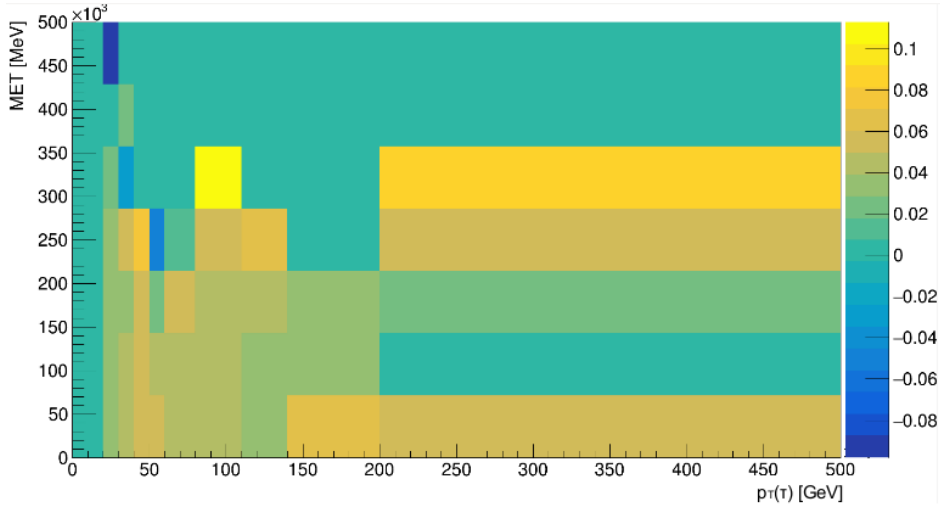

Figure 6.3: Fake efficiency, measured in the $E_{\mathrm{T}}^{\mathrm{miss}}$-$p_{\mathrm{T}}(\tau)$-plane, 1-prong, from sample with DSID 364194 ($280\,\mathrm{GeV} < p_{\mathrm{T}}(W) < 500\,\mathrm{GeV}$, light jet filter). The reason for negative values of the fake efficiency is the following: Monte Carlo simulated events are weighted in order to give the same event distribution as one would expect in data. It can occur that some event weights have a negative value, that propagates into the fake efficiency.

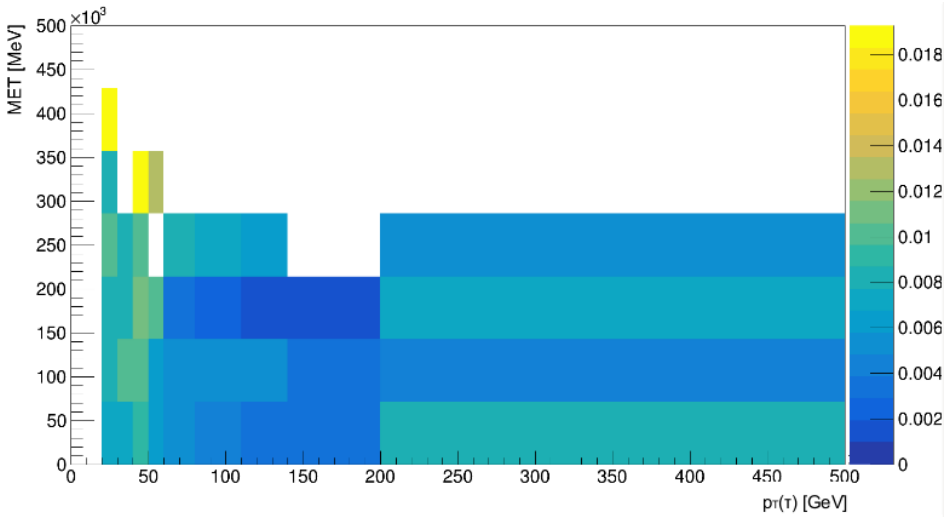

Figure 6.4: Fake efficiency, measured in the $E_{\mathrm{T}}^{\mathrm{miss}}$-$p_{\mathrm{T}}(\tau)$-plane, 3-prong, from sample with DSID 364194 ($280\,\mathrm{GeV} < p_{\mathrm{T}}(W) < 500\,\mathrm{GeV}$, light jet filter).

DSID	nominal (σ_{stat})	reweighted (σ_{stat})	$\frac{\text{reweighted}}{\text{nominal}}$
364184	106231.46 (3.44%)	102100.44 (0.76%)	0.96
364185	31166.27 (4.28%)	28159.71 (1.09%)	0.90
364186	7316.80 (%))	7265.14 (1.03%)	0.99
364187	24381.11 (3.51%)	27438.94 (3.66%)	1.13
364188	11474.72 (2.56%)	10406.13 (0.86%)	0.91
364189	4096.16 (3.05%)	3789.89 (0.79%)	0.93
364190	7978.95 (1.96%)	8270.47 (0.96%)	1.04
364191	5705.10 (1.65%)	5126.24 (5.27%)	0.90
364192	1806.31 (0.10%)	1639.13 (0.24%)	0.91
364193	1301.12 (2.08%)	1332.74 (0.52%)	1.02
364194	1087.63 (2.12%)	1043.22 (0.58%)	0.96
364195	403.59 (3.47%)	385.34 (0.52%)	0.96
364196	511.44 (4.11%)	522.52 (0.50%)	1.02
364197	39.13 (2.38%)	40.38 (0.57%)	1.03
merged	203499.79 (1.98%)	193706.06 (0.45%)	0.95

Table 6.2: Event yields for the separate Monte Carlo W+jets samples at preselection level with common binning. The nominal yields refer to the yields before the Tau Promotion is applied, and the reweighted ones refer to the ones after the application of the method. The statistical uncertainty σ_{stat} is reduced by a factor 4.4 in total. The ratio $\frac{\text{reweighted}}{\text{nominal}}$ is 0.95 total.

DSID	nominal	promoted	$\frac{\text{reweighted}}{\text{nominal}}$
364184	7227	233903	32.37
364185	4917	140480	28.57
364186	6096	196382	32.21
364187	15733	558803	35.52
364188	13853	423309	30.56
364189	10649	354158	33.26
364190	10108	458777	45.39
364191	10505	395712	37.67
364192	28439	1129577	39.72
364193	4733	257124	54.33
364194	3752	176074	46.93
364195	3386	155971	46.06
364196	5793	325555	56.20
364197	3457	208356	60.27
merged	128648	5014181	38.98

Table 6.3: Unweighted event yields for the separate Monte Carlo W+jets samples at preselection level with common binning. In total the amount of $W \to \tau\nu$-events that contribute to the background increases by a factor of 38.98 after the container taus in the eligible events have been promoted.

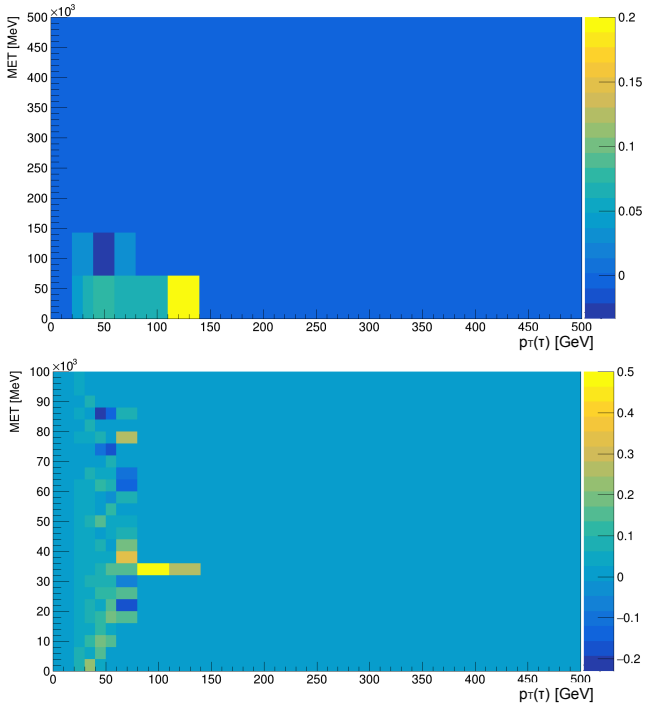

Figure 6.5: The upper plot shows the fake efficiency for the $W \to \tau\nu$-sample with the DSID 364184 ($0\,\text{GeV} < p_\text{T}(W) < 70$, light jet filter), and the lower plot shows the fake efficiency for the same sample after the binning optimization. The lower plot has finer bin distribution leading to a more precise measurement of the fake efficiency.

Within this thesis studies were conducted to find the optimal binning, which gives a precise reweighting, while keeping the statististical uncertainty low. Especially for the Monte Carlo slices, where the W-boson has a low $p_\text{T}(W)$-value ($0\,\text{GeV} < p_\text{T}(W) < 70\,\text{GeV}$), it is important to use a narrow binning in the low $p_\text{T}(W)$-range, while for the Monte Carlo slices with higher $p_\text{T}(W)$-values, the binning can be broader. Due to this fact a variable binning was used for the different Monte Carlo samples. The resulting yields for the Tau Promotion method by measuring the fake efficiency in the E_T^miss-$p_\text{T}(\tau)$-plane are listed in Table 6.4. The reweighting using the variable binning results in a ratio $\frac{\text{reweighted}}{\text{nominal}}$ of 1.01. The reason for the improvement of the ratio compared to the approach with common binning that gave a poorer ratio $\frac{\text{reweighted}}{\text{nominal}}$ of 0.95, is that for the Monte Carlo slices with a low $p_\text{T}(W)$-range, the fake efficiency is steeper for the the low $p_\text{T}(W)$-values, which requires a finer binning compared to the slices with a higher $p_\text{T}(W)$-range. Due to more fluctuations when using a larger number of bins, the statistical uncertainties for the variable binning become slighty higher, rising from 0.45% to 0.71%, which is in the range of acceptance for gaining a better reweighting. The adjustment of the binning for the fake efficiency for the slices with a low $p_\text{T}(W)$-range is shown in Figure 6.5

DSID	nominal (σ_{stat})	reweighted (σ_{stat})	$\frac{\text{reweighted}}{\text{nominal}}$
364184	106231.46 (3.44%)	106266.96 (0.86%)	1.00
364185	31166.27 (4.28%)	30958.45 (1.57%)	0.99
364186	7316.80 (5.66%)	7265.14 (1.03%)	0.99
364187	24381.11 (3.51%)	27438.94 (3.66%)	1.13
364188	11474.72 (2.56%)	10406.13 (0.86%)	0.91
364189	4096.16 (3.05%)	3789.89 (0.79%)	0.93
364190	7978.95 (1.96%)	8270.47 (0.96%)	1.04
364191	5705.10 (1.64%)	5126.24 (0.52%)	0.90
364192	1806.31 (1.00%)	1639.13 (0.24%)	0.91
364193	1301.12 (2.07%)	1332.74 (0.53%)	1.02
364194	1087.63 (2.12%)	1043.22 (0.57%)	0.96
364195	403.59 (3.47%)	385.34 (0.52%)	0.96
364196	511.44 (4.11%)	522.52 (0.38%)	1.02
364197	39.13 (2.56%)	40.38 (5.70%)	1.03
merged	203499.79 (1.98%)	204485.56 (0.71%)	1.01

Table 6.4: Event yields for the separate Monte Carlo W+jets samples at preselection level with variable binning. Compared to Table 6.2, the reweighting is more precise with $\frac{\text{reweighted}}{\text{nominal}}$ being in total 1.01. The factor, by which σ_{stat} is reduced in total, is 2.8. That is lower than the factor in Table 6.2 due to the more narrow binning for the DSIDs 364184 and 364185, that also causes the improved reweighting.

Figure 6.6 shows the nominal and the reweighted distribution of the variables, that are most relevant for the search for direct production of scalar tau leptons [34], for the merged W+jets Monte Carlo. The distributions for each Monte Carlo slice can be found in Appendix II. It can be observed that the reweighted ditribution has less statistical fluctuations than the nominal one. The ratio plots indicate the precision of the reweighting.

The Tau Promotion method consists of two subsequent cycles. In the first cycle, the fake efficiency is measured and in the second cycle the container taus are promoted and the events are afterwards reweighted using the fake efficiency measured in the first cycle. This offers various possibilities in how to arrange the separate Monte Carlo slices into these two cycles. For the studies in Table 6.2 and Table 6.4 the fake efficiency was measured for each slice separately.

Two alternative options that were studied in this thesis, are to combine the Monte Carlo slices, with the same $p_{\text{T}}(W)$-value of the W-boson in the first cycle as well as combining the slices with the same applied filter, respectively. Table 6.5 and Table 6.6 show the yields for the two different cases. It can be observed that the reweighting has a poorer performance, when computing the fake efficiency for several samples together. Thus, neither samples of the same $p_{\text{T}}(W)$-value nor samples with the same applied filter have a similiar fake efficiency.

$p_{\mathrm{T}}(W)$ [GeV]	nominal (σ_{stat})	rew. sep. (σ_{stat})	rew. tog. (σ_{stat})	$\frac{\text{rew.sep}}{\text{nom.}}$	$\frac{\text{rew.tog.}}{\text{nom.}}$
0-70	144714.53 (2.70 %)	144334.88 (0.72%)	63085.09 (0.71%)	1.00	0.43
70-140	39951.98 (2.29%)	38520.54 (0.54%)	14399.94 (0.54%)	0.96	0.36
140-280	15490.36 (1.18%)	14615.75 (0.36%)	3565.44 (0.31%)	0.95	0.23
280-500	2792.33 (1.40%)	2655.07 (0.30%)	955.96 (0.31%)	0.95	0.34

Table 6.5: Event yields for the separate Monte Carlo W+jets samples at preselection level for measuring the fake efficiency in bins in the $E_{\mathrm{T}}^{\mathrm{miss}}$-$p_{\mathrm{T}}(\tau)$-plane separately for each Monte Carlo slices with the same $p_{\mathrm{T}}(W)$-range

filter	nominal (σ_{stat})	rew. sep. (σ_{stat})	rew. tog. (σ_{stat})	$\frac{\text{rew.sep}}{\text{nom.}}$	$\frac{\text{rew.tog.}}{\text{nom.}}$
light jet	139892.64 (2.68%)	139877.02 (0.67%)	58259.33 (0.70%)	1.00	0.41
b jet	49433.71 (2.77%)	47370.55 (1.04%)	12053.23 (0.72%)	0.96	0.24
c jet	13622.86 (3.19%)	12878.67 (0.54%)	3339.10 (0.54%)	0.95	0.25

Table 6.6: Event yields for the separate Monte Carlo W+jets samples at preselection level for measuring the fake efficiency in bins in the $E_{\mathrm{T}}^{\mathrm{miss}}$-$p_{\mathrm{T}}(\tau)$-plane separately for each Monte Carlo slices with the same filter.

6.2.2 Measurement of fake efficiency in $\eta(\tau)$-$p_{\mathrm{T}}(\tau)$-plane

The fake efficiency can also be measured using $\eta(\tau)$ together with $p_{\mathrm{T}}(\tau)$, as it is shown in Figure 6.8 for 1-prong, and in Figure 6.9 for 3-prong.

Also for that approach studies were made within this thesis to find the optimal binning, again meaning that the fake efficiency should be measured accurately leading to a precise reweighting while keeping the statistical uncertainty low. The results for the application of the Tau Promotion method for measuring the fake efficiency in $\eta(\tau)$-$p_{\mathrm{T}}(\tau)$-plane are illustrated in Table 6.7. One can observe that measuring of the fake efficiency in the $\eta(\tau)$-$p_{\mathrm{T}}(\tau)$-plane does not provide a reweighting as good as when measuring the fake efficiency in the in $E_{\mathrm{T}}^{\mathrm{miss}}$-$p_{\mathrm{T}}(\tau)$-plane.

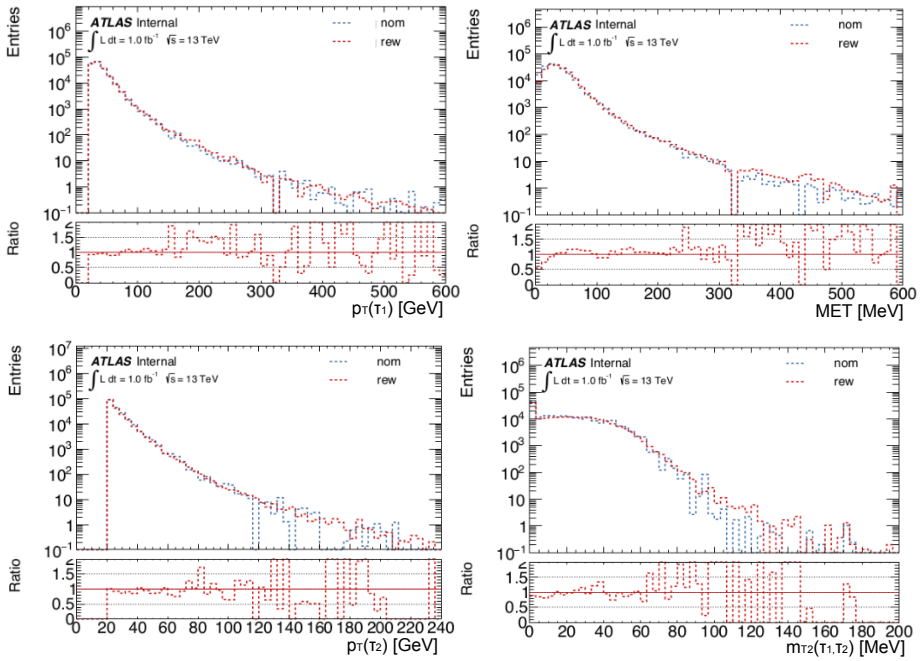

Figure 6.6: This figure shows the distributions of the W+jets background for the most relevant variables for the search for the direct pair production of two staus. The blue curve is the nominal distribution and the red curve is the reweighted distribution after the Tau Promotion was applied. Starting from the upper left corner, from left to right, the variables are: transverse momentum of the leading tau $p_{\mathrm{T}}(\tau_1)$, missing transverse momentum MET , transverse momentum of the next-to-leading tau $p_{\mathrm{T}}(\tau_2)$, and the stransverse mass of the sum of the leading tau and next-to-leading tau $m_{\mathrm{T2}}(\tau_1, \tau_2)$. The ratio plot shows the ratio of the nominal curve with respect to the reweighted one. Especially in the tails of the distribution, which are most relevant for the analysis, one can observe that the reweighted curve has significantly less statistical fluctuations compared to the nominal curve.

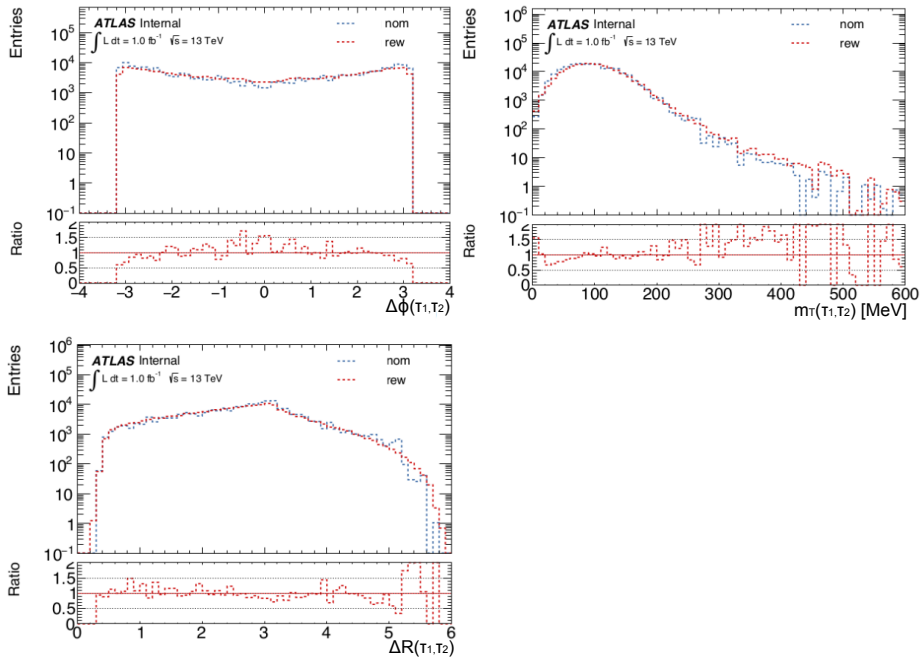

Figure 6.7: This figure shows the distributions of the W+jets background, analogously to figure (..), for the following variables: difference in the azimuthal angel $\Delta\phi(\tau_1, \tau_2)$ between the leading tau and next-to-leading tau, transverse mass of the sum of the leading tau and next-to-leading tau $m_{\mathrm{T}}(\tau_1, \tau_2)$, and the difference in the pseudorapidity between the leading tau and next-to-leading tau $\Delta\mathrm{R}(\tau_1, \tau_2)$.

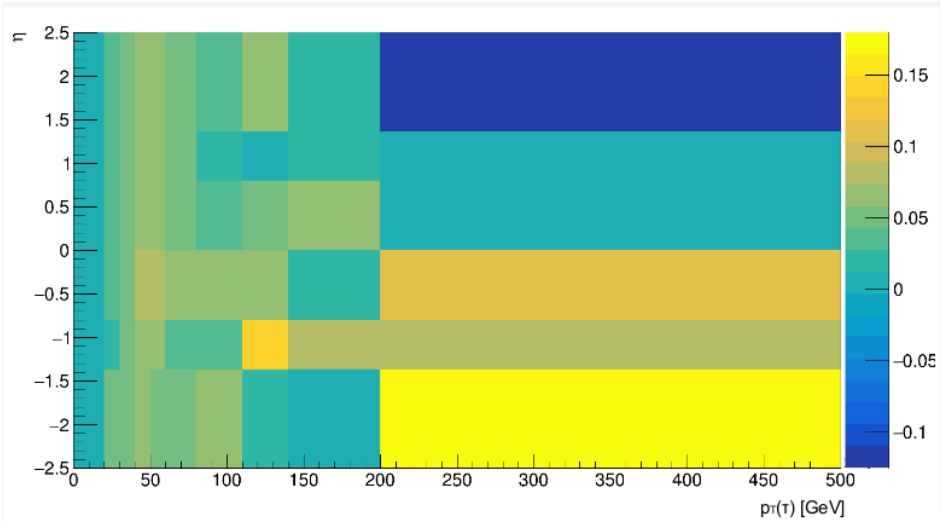

Figure 6.8: Fake efficiency, measured in the $\eta(\tau)$-$p_{\mathrm{T}}(\tau)$-plane, 1-prong, of sample with DSID 364192 ($140\,\mathrm{GeV} < p_{\mathrm{T}}(W) < 280\,\mathrm{GeV}$, b-jet filter).

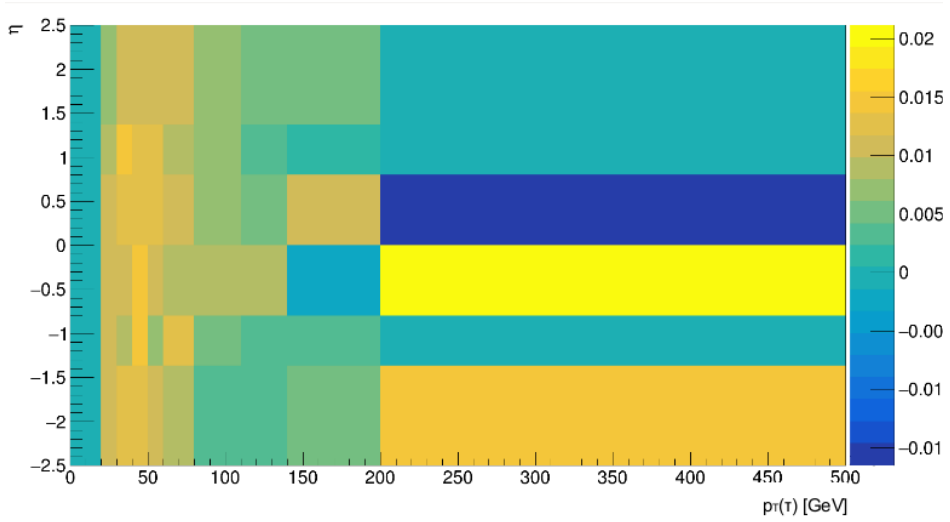

Figure 6.9: Fake efficiency, measured in the $\eta(\tau)$-$p_{\mathrm{T}}(\tau)$-plane, 3-prong, of sample 364192 ($140\,\mathrm{GeV} < p_{\mathrm{T}}(W) < 280\,\mathrm{GeV}$, b-jet filter).

DSID	nominal (σ_{stat})	reweighted (σ_{stat})	$\frac{\text{reweighted}}{\text{nominal}}$
364184	106231.46 (3.44%)	98195.54 (0.92%)	0.92
364185	31166.27 (4.28%)	27891.01 (1.03%)	0.90
364186	7316.80 (5.66%)	6897.13 (0.91%)	0.94
364187	24381.11 (3.51%)	23683.74 (0.76%	0.97
364188	11474.72 (2.56%)	10609.88 (0.71%	0.92
364189	4096.16 (3.05%)	3840.75 (0.73%)	0.93
364190	7978.95 (1.96%)	7668.14 (0.63%)	0.96
364191	5705.10 (1.64%)	4913.69 (0.39%)	0.86
364192	1806.31 (1.00%)	1623.43 (0.25%)	0.90
364193	1301.12 (2.07%)	1225.42 (0.49%)	0.94
364194	1087.63 (2.12%)	972.74 (0.49%)	0.89
364195	403.59 (3.47%)	356.35 (0.56%)	0.88
364196	511.44 (4.11%)	486.15 (0.61%)	0.95
364197	39.13 (2.56%)	36.26 (0.44%)	0.92
merged	203499.79 (1.98%)	188400.30 (0.47%)	0.93

Table 6.7: Event yields for the separate Monte Carlo W+jets samples at preselection level for measuring the fake efficiency in bins in the $\eta(\tau)$-$p_{\mathrm{T}}(\tau)$-plane.

6.2.3 Promotion of container tau with leading p_{T}

Another approach for the Tau Promotion method is to promote the container tau with the leading p_{T} in each eligible event instead of selecting it randomly. The idea behind

this procedure is that more container taus would pass the applied cuts in the analysis as they have a higher transverse momentum, so that more events enter the signal region, leading to a potential additional reduction of the statistical error. For this study the following cuts on the transverse momenta were applied additional to the preselection: $p_{\mathrm{T}}(\tau_1) > 50\mathrm{GeV}$ and $p_{\mathrm{T}}(\tau_2) > 40\mathrm{GeV}$.

However, as shown in Table 6.8, the reweighted yields for the selection of the container tau with the leading p_{T} show a slight overestimation compared to reweighted yields when selecting a container tau randomly.

DSID	nominal	rew.$_{\mathrm{rand}}$ (σ_{stat})	rew.$_{\mathrm{lead}}$ (σ_{stat})	$\frac{\text{rew.}_{\mathrm{rand}}}{\text{nominal}}$	$\frac{\text{rew.}_{\mathrm{lead}}}{\text{nominal}}$
364184	2765.60 (18.23%)	2709.21 (8.27%)	2993.27 (9.22%)	0.98	1.08
364185	571.94 (39.75%)	1246.98 (26.40%)	1472.27 (23.71%)	2.18	2.57
364186	188.89 (22.34)	93.93 (11.83%)	99.88 (8.43%)	0.49	0.53
364187	3356.27 (6.61%)	3638.00 (2.36%)	4222.75 (2.25%)	1.08	1.53
364188	1381.47 (7.53%)	1291.79 (1.63%)	1497.80 (1.67%)	0.93	1.08
364189	410.36 (8.54%)	446.18 (2.24%)	509.34 (2.16%)	1.08	1.24
364190	1301.73 (5.23%)	1328.57 (1.51%)	1579.24 (1.46%)	1.02	1.21
364191	944.34 (4.45%)	801.18 (1.12%)	993 (1.01%)	0.85	1.05
364192	255.77 (3.11%)	237.81 (0.70%)	288.29 (0.67%)	0.93	1.13
364193	271.69 (4.69%)	253.63 (1.17%)	308.91 (1.10%)	0.93	1.14
364194	221.47 (4.98%)	188.12 (1.06%)	233.61 (1.07%)	0.85	1.05
364195	76.97 (4.68%)	69.51 (1.28%)	85.43 (1.18%)	0.90	1.10
364196	84.38 (23%)	94.68 (0.93%)	117.79 (0.85%)	1.12	1.39
364197	6.78 (5.01%)	6.31 (1.11%)	7.90 (1.14%)	0.93	1.17
merged	11837.67 (5.19%)	12405.90 (3.39%)	14409.99 (3.18%)	1.05	1.22

Table 6.8: Event yields for the separate Monte Carlo W+jets samples with the applied cuts $p_{\mathrm{T}}(\tau_1) > 50\mathrm{GeV}$ and $p_{\mathrm{T}}(\tau_2) > 40\mathrm{GeV}$ for the promotion of the leading tau in the $E_{\mathrm{T}}^{\mathrm{miss}}$-$p_{\mathrm{T}}(\tau)$ -plane.

6.3 Results

6.3.1 Promotion of container taus to loose and tight working point

In this subsection the results for the application of the Tau Promotion method to the loose and tight working points are presented. Table 6.9 and Table 6.10 show the weighted and unweighted yields for the promotion of container taus to the tight working point, respectively. The statistical uncertainty σ_{stat} is reduced by a factor 4.29 in total, while the ratio $\frac{\text{reweighted}}{\text{nominal}}$ is 1.01 in total. After the application of the method the number of events that contribute to the background estimation increases by a factor of 82.26.

DSID	nominal (σ_{stat})	reweighted (σ_{stat})	$\frac{\text{reweighted}}{\text{nominal}}$
364184	39743.53 (5.90%)	38051.19 (0.85%)	0.95
364185	13789.58 (6.19%)	13871.19 (1.87%)	1.01
364186	2762.59 (6.01%)	2509.47 (3.27%)	0.91
364187	9562.04 (7.40%)	9401.35 (1.05%)	0.98
364188	4443.70 (4.21%)	3930.56 (0.84%)	0.89
364189	1616.94 (4.40%)	1495.46 (0.94%)	0.93
364190	3015.90 (3.11%)	3025.41 (0.73%)	1.00
364191	2148.88 (2.75%)	1916.14 (0.47%)	0.89
364192	674.78 (1.63%)	602.45 (0.17%)	0.89
364193	482.08 (3.52%)	499.90 (0.80%)	1.04
364194	437.51 (3.43%)	395.67 (0.51%)	0.90
364195	144.11 (8.33%)	143.48 (0.69%)	0.99
364196	203.21 (2.46%)	194.80 (1.03%)	0.96
364197	14.48 (4.14%)	13.55 (0.74%)	0.94
merged	79039.42 (3.30%)	80150.57 (0.77%)	1.01

Table 6.9: Event yields for the separate Monte Carlo W+jets samples at preselection level for the container tau promotion to the tight working point, weighted to an integrated luminosity of 36.1 $f\text{b}^{-1}$. The nominal yields refer to the yields before the Tau Promotion is applied, and the reweighted ones refer to the ones after the application of the method. The statistical uncertainty σ_{stat} is reduced by a factor 4.29 in total. The ratio $\frac{\text{reweighted}}{\text{nominal}}$ is 1.01 in total.

DSID	nominal	promoted	$\frac{\text{promoted}}{\text{nominal}}$
364184	2643	175783	66.51
364185	1830	106411	58.15
364186	2185	146895	67.22
364187	5714	434630	76.06
364188	5162	329315	63.80
364189	3918	273173	69.72
364190	3730	360709	96.70
364191	3975	310010	77.99
364192	10577	878747	83.08
364193	1695	202822	119.66
364194	1408	138233	98.18
364195	1205	121848	101.12
364196	2137	256799	120.17
364197	1234	164644	133.42
merged	47413	3900019	82.26

Table 6.10: Unweighted event yields for the separate Monte Carlo W+jets samples at preselection level for the container tau promotion to the tight working point. The nominal yields refer to the yields before the Tau Promotion is applied, and the reweighted ones refer to the ones after the application of the method. The ratio $\frac{\text{reweighted}}{\text{nominal}}$ is 82.26 in total.

In Table 6.11 and Table 6.12 the weighted and unweighted yields are listed for the promotion to the loose working point, respectively. The statistical uncertainty σ_{stat} is reduced by a factor 2.75 in total and the ratio $\frac{\text{reweighted}}{\text{nominal}}$ is 1.28 total. After the container taus are promoted, the number of events that contribute to the background increases by a factor of 22.16.

DSID	nominal (σ_{stat})	reweighted (σ_{stat})	$\frac{\text{reweighted}}{\text{nominal}}$
364184	245058.80 (0.02%)	311542.38 (0.57%)	1.27
364185	71191.75 (2.84%)	81230.20 (0.80%)	1.14
364186	16936.82 (2.96%)	21272.48 (0.64%)	1.26
364187	56121.19 (2.02%)	71315.77 (0.63%)	1.27
364188	25978.24 (1.71%)	29026.29 (0.59%)	1.12
364189	9229.73 (2.02%)	10865.74 (0.59%)	1.18
364190	18731.56 (1.76%)	22619.19 (0.46%)	1.21
364191	12793.30 (1.07%)	13717.28 (0.34%)	1.07
364192	4138.98 (0.65%)	4591.53 (0.20%)	1.11
364193	3050.27 (1.31%)	3518.02 (0.37%)	1.15
364194	2507.93 (1.40%)	2675.60 (0.56%)	1.07
364195	915.98 (1.86%)	973.22 (0.41%)	1.06
364196	1196.48 (1.92%)	1313.82 (0.46%)	1.10
364197	88.83 (1.14%)	95.77 (0.38%)	1.08
merged	467939.93 (1.32%)	574757.35 (0.34%)	1.23

Table 6.11: Event yields for the separate Monte Carlo W+jets samples at preselection level for the container tau promotion to the loose working point, weighted to an integrated luminosity of 36.1 $f\text{b}^{-1}$. The nominal yields refer to the yields before the Tau Promotion is applied, and the reweighted ones refer to the ones after the application of the method. The statistical uncertainty σ_{stat} is reduced by a factor 2.75 in total. The ratio $\frac{\text{reweighted}}{\text{nominal}}$ is 1.28 total.

DSID	nominal (σ_{stat})	promoted (σ_{stat})	$\frac{\text{promoted}}{\text{nominal}}$
364184	16616	343136	20.65
364185	11384	202014	17.75
364186	14070	289666	20.59
364187	36565	754290	20.63
364188	32126	568382	17.69
364189	24825	484923	19.53
364190	23759	589531	24.82
364191	24180	510221	21.10
364192	66338	1478424	22.29
364193	11065	322908	29.18
364194	8904	222883	25.03
364195	7830	199449	25.47
364196	13617	407900	29.96
364197	8121	259603	31.97
merged	299400	6633330	22.16

Table 6.12: Unweighted event yields for the separate Monte Carlo W+jets samples at preselection level for the container tau promotion to the loose working point. The nominal yields refer to the yields before the Tau Promotion is applied, and the reweighted ones refer to the ones after the application of the method. The ratio $\frac{\text{reweighted}}{\text{nominal}}$ is 22.16 total.

6.3.2 Application of Tau Promotion in the search for direct production of supersymmetric scalar tau leptons

The results in this subsection were provided by Clara Leitgeb from LMU Munich. The event yields in Table 6.13 and Table 6.14 were obtained by using a Boosted Decision Tree as a tool for multivariate analysis. Further information on the signal region optimization and the samples used can be found in [34].

Table 6.13 shows the event yields for each background process without applying the Tau Promotion method on the W+jets sample. It can be observed that the statistical uncertainty on the W+jets events is quite large with 129.44%, which is propagated into the statistical uncertainty of the total background. In Table 6.14 the exact same yields are listed for applying the Tau Promotion method on the W+jets sample. While the number of events slightly reduces from 1.05 to 0.88, the crucial result is the reduction of the statistical error from 129.44% to 66.85%. This leads to a reduction of the statistical uncertainty of the total background from 50.14% to 25.95%.

Process	Events (σ_{stat})
W+jets	1.05 (129.44%)
Z+jets	0.84 (51.10%)
Diboson	0.80 (81.56%)
Top	0.19 (45.67%)
QCD	0.46 (125.03%)
Total background	3.34 (50.14%)

Table 6.13: Event yields for each background process for the search for direct production of supersymmetric scalar tau leptons, scaled to an integrated luminosity of 36 fb^{-1}. Tau Promotion was not applied on the W+jets sample.

Process	Events (σ_{stat})
W+jets	0.88 (66.85%)
Z+jets	0.84 (51.10%)
Diboson	0.80 (81.56%)
Top	0.19 (45.67%)
QCD	0.46 (125.03%)
Total background	3.17 (25.95%)

Table 6.14: Event yields for each background process for the search for direct production of supersymmetric scalar tau leptons, scaled to an integrated luminosity of 36 fb^{-1}. Tau Promotion was applied on the W+jets sample. Compared to the nominal yields in Table 6.13 the statistical uncertainty on W+jets reduces from 129.44% to 66.85%, while the number of events slightly reduces from 1.05 to 0.88.

The event yields show that Z+jets processes compose the second largest background for the search for direct production of supersymmetric scalar tau leptons, after the W+jets events. In the subsequent chapter studies are conducted if a similiar method as the Tau Promotion can be applied on the Z+jets background in order to reduce the statistical uncertainties.

7 Studies on improvement for Z+jets Monte Carlo background modelling

As it was mentioned in chapter 6, next to Monte Carlo background modelling of the W+jets events in the search for the direct pair production of two staus, also the one for the Z+jets events shows a high statistical uncertainty. Therefore it was examined if a method similar to the Tau Promotion method could be applied to the Z+jets Monte Carlo modelling. The Z+jets events were split up into the separate decay chanels, namely $Z \to \tau\tau$, $Z \to \mu\mu$, $Z \to ee$, and $Z \to \nu\nu$, in order to estimate each contribution to the total background. The distributions are shown for the signal region for each relevant variable in Figure 7.1.

decay cannel	event yields (σ_{stat})
$Z \to \tau\tau$	1410991.13 (0.71%)
$Z \to \mu\mu$	1791.81 (1.43%)
$Z \to ee$	7662.12 (7.23%)
$Z \to \nu\nu$	6215.09 (10.82%)

Table 7.1: Event yields for the different Z+jets channels weighted to an integrated luminosity of 36 $f\text{b}^{-1}$.

The reweighting procedure in the Tau Promotion method is based on the fake efficiency. Due to this fact it is important that a sufficient number of the taus in the $Z \to \tau\tau$ events are fake taus. Table 7.3 shows, however, that most of the events in the $Z \to \tau\tau$-channel that contribute to the signal region, shown in Table 7.2, contain only real taus. The cutflow for this signal region is taken from [47], as the search for the direct production of charginos and neutralinos in final states with tau leptons also has two tau leptons in the final state. Hence it is not possible to apply a method similar to the Tau Promotion method in order to reduce the systematic uncertainty on the Z+jets Monte Carlo background modelling for the search of the direct pair production of two staus.

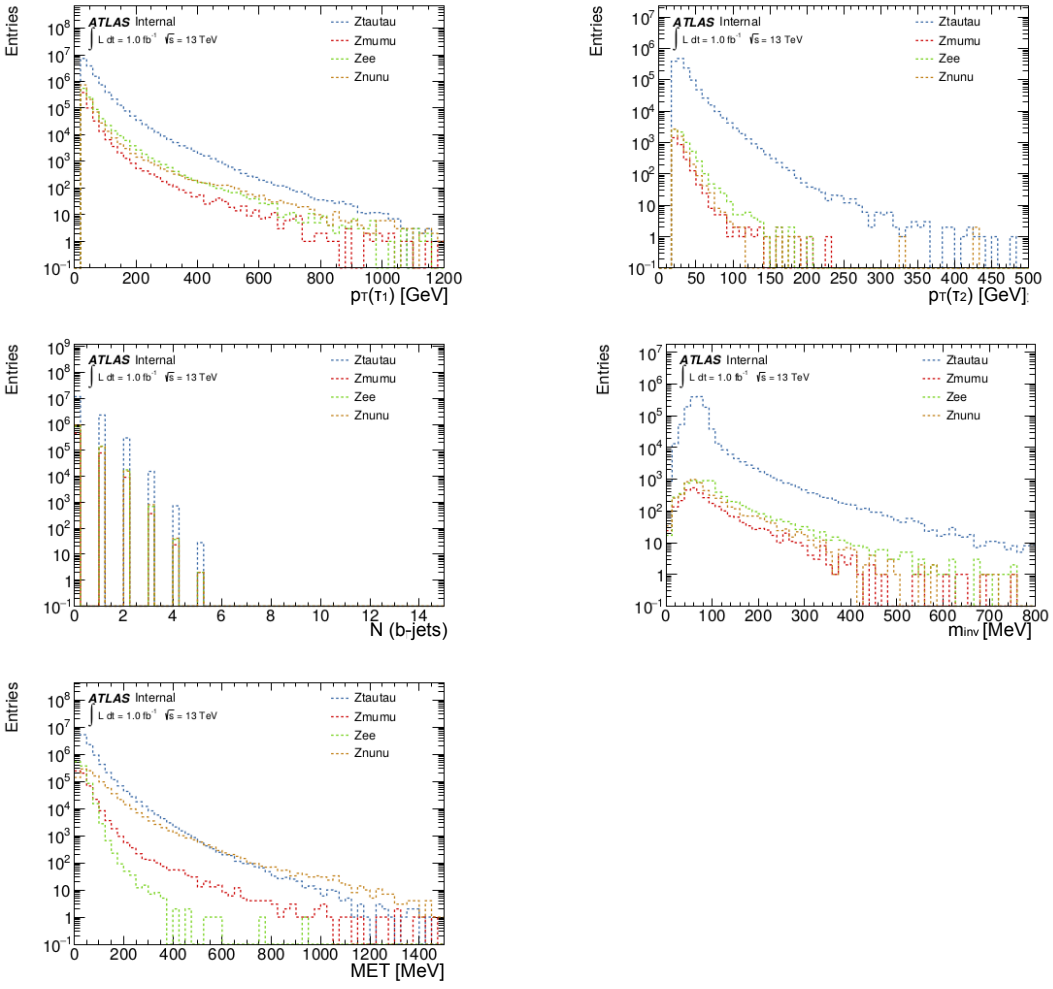

Figure 7.1: Stacked distributions of the Monte Carlo background Z+jets events weighted to an integrated luminosity of 36.1 fb^{-1} and separated by their decay channel. The distributions show, that the decay channel $Z \to \tau\tau$ has the largest contribution to the total Monte Carlo background estimation of Z+jets events. The yields are shown in Table 7.1.

Signal region
at least one opposite sign tau pair
b-jet veto
Z-veto
at least two medium tau candidates
$m_{\mathrm{T2}}(\tau_1, \tau_2) > 70$ GeV
$E_{\mathrm{T}}^{\mathrm{miss}} > 150$ GeV
$p_{\mathrm{T}}(\tau_1) > 50$ GeV
$p_{\mathrm{T}}(\tau_2) > 40$ GeV

Table 7.2: Signal region taken from [47] to estimate contribution of real and fake taus from Z+jets background.

	weighted event yields	unweighted event yields
all taus (real and fake)	0.61 (42.74%)	15
at least one fake tau	0.06 (65.60%)	3
at least two fake taus	0	0

Table 7.3: In order to examine if a method similar to the Tau Promotion method can be applied to the Z+jets Monte Carlo background modelling, it was investigated if the majority of the taus in the signal region (Table 7.2) is fake or real. The events are weighted to an integrated luminosity of 36.1 fb^{-1}. As the majority of events contain real taus, it is not possible to a apply a method similar to the Tau Promotion method.

8 Conclusion and Outlook

The associated production of a W-boson together with one or more jets as a background process in final states containing two hadronically decaying tau leptons suffers from large statistical uncertainties. The reason for this is that only a small fraction of these Monte Carlo generated events contain two tau leptons in the final state, one real tau originating from the W-boson decay, and one fake tau with a jet misidentified as a tau lepton. Thus, the majority of the events cannot be used for the background estimation.

The Tau Promotion method is a Monte Carlo driven reweighting technique that enables to use a large fraction of the processes without two tau leptons for the background modelling, leading to a reduction of the statistical error. The method is currently used for the HadHad-channel in the search for direct production of supersymmetric scalar tau leptons using 13 TeV data taken with the ATLAS Detector at the LHC.

Concerning the systematic uncertainties of the method, that are not estimated yet, one could propagate the uncertainties on the fake efficiency which is used for the reweighting procedure.

So far the Tau Promotion method can be applied to the $W \rightarrow \tau\nu$-channel of the W+jets background. A possible development would be to conduct further studies on how to adapt the current method so it can be also used for W+jets final states with a W-boson and a light lepton.

Furthermore, it can be studied to also promote real taus, which were not identified as real taus. For that one needs to take into account that the misidentification rate for this case differs from the fake efficiency.

Appendix I: List of MC Samples

$W+$ jets samples:

mc15_13TeV.364184.Sherpa_221_NNPDF30NNLO_Wtaunu_MAXHTPTV0_70_CVetoBVeto.merge.DAOD_SUSY3.e5340_s2726_r7772_r7676_p2949
mc15_13TeV.364185.Sherpa_221_NNPDF30NNLO_Wtaunu_MAXHTPTV0_70_CFilterBVeto.merge.DAOD_SUSY3.e5340_s2726_r7772_r7676_p2949
mc15_13TeV.364186.Sherpa_221_NNPDF30NNLO_Wtaunu_MAXHTPTV0_70_BFilter.merge.DAOD_SUSY3.e5340_s2726_r7772_r7676_p2949
mc15_13TeV.364187.Sherpa_221_NNPDF30NNLO_Wtaunu_MAXHTPTV70_140_CVetoBVeto.merge.DAOD_SUSY3.e5340_s2726_r7772_r7676_p2949
mc15_13TeV.364188.Sherpa_221_NNPDF30NNLO_Wtaunu_MAXHTPTV70_140_CFilterBVeto.merge.DAOD_SUSY3.e5340_s2726_r7772_r7676_p2949
mc15_13TeV.364189.Sherpa_221_NNPDF30NNLO_Wtaunu_MAXHTPTV70_140_BFilter.merge.DAOD_SUSY3.e5340_s2726_r7772_r7676_p2949
mc15_13TeV.364190.Sherpa_221_NNPDF30NNLO_Wtaunu_MAXHTPTV140_280_CVetoBVeto.merge.DAOD_SUSY3.e5340_s2726_r7772_r7676_p2949
mc15_13TeV.364191.Sherpa_221_NNPDF30NNLO_Wtaunu_MAXHTPTV140_280_CFilterBVeto.merge.DAOD_SUSY3.e5340_s2726_r7772_r7676_p2949
mc15_13TeV.364192.Sherpa_221_NNPDF30NNLO_Wtaunu_MAXHTPTV140_280_BFilter.merge.DAOD_SUSY3.e5340_s2726_r7772_r7676_p2949
mc15_13TeV.364193.Sherpa_221_NNPDF30NNLO_Wtaunu_MAXHTPTV280_500_CVetoBVeto.merge.DAOD_SUSY3.e5340_s2726_r7772_r7676_p2949
mc15_13TeV.364194.Sherpa_221_NNPDF30NNLO_Wtaunu_MAXHTPTV280_500_CFilterBVeto.merge.DAOD_SUSY3.e5340_s2726_r7772_r7676_p2949
mc15_13TeV.364195.Sherpa_221_NNPDF30NNLO_Wtaunu_MAXHTPTV280_500_BFilter.merge.DAOD_SUSY3.e5340_s2726_r7772_r7676_p2949
mc15_13TeV.364196.Sherpa_221_NNPDF30NNLO_Wtaunu_MAXHTPTV500_1000.merge.DAOD_SUSY3.e5340_s2726_r7772_r7676_p2949
mc15_13TeV.364197.Sherpa_221_NNPDF30NNLO_Wtaunu_MAXHTPTV1000_E_CMS.merge.DAOD_SUSY3.e5340_s2726_r7772_r7676_p2949

$Z+$ jets samples:

mc15_13TeV.364100.Sherpa_221_NNPDF30NNLO_Zmumu_MAXHTPTV0_70_CVetoBVeto.merge.DAOD_SUSY3.e5271_s2726_r7772_r7676_p2949
mc15_13TeV.364101.Sherpa_221_NNPDF30NNLO_Zmumu_MAXHTPTV0_70_CFilterBVeto.merge.DAOD_SUSY3.e5271_s2726_r7772_r7676_p2949
mc15_13TeV.364102.Sherpa_221_NNPDF30NNLO_Zmumu_MAXHTPTV0_70_BFilter.merge.DAOD_SUSY3.e5271_s2726_r7772_r7676_p2949
mc15_13TeV.364103.Sherpa_221_NNPDF30NNLO_Zmumu_MAXHTPTV70_140_CVetoBVeto.merge.DAOD_SUSY3.e5271_s2726_r7772_r7676_p2949
mc15_13TeV.364104.Sherpa_221_NNPDF30NNLO_Zmumu_MAXHTPTV70_140_CFilterBVeto.merge.DAOD_SUSY3.e5271_s2726_r7772_r7676_p2949
mc15_13TeV.364105.Sherpa_221_NNPDF30NNLO_Zmumu_MAXHTPTV70_140_BFilter.merge.DAOD_SUSY3.e5271_s2726_r7772_r7676_p2949
mc15_13TeV.364106.Sherpa_221_NNPDF30NNLO_Zmumu_MAXHTPTV140_280_CVetoBVeto.merge.DAOD_SUSY3.e5271_s2726_r7772_r7676_p2949
mc15_13TeV.364107.Sherpa_221_NNPDF30NNLO_Zmumu_MAXHTPTV140_280_CFilterBVeto.merge.DAOD_SUSY3.e5271_s2726_r7772_r7676_p2949
mc15_13TeV.364108.Sherpa_221_NNPDF30NNLO_Zmumu_MAXHTPTV140_280_BFilter.merge.DAOD_SUSY3.e5271_s2726_r7772_r7676_p2949
mc15_13TeV.364109.Sherpa_221_NNPDF30NNLO_Zmumu_MAXHTPTV280_500_CVetoBVeto.merge.DAOD_SUSY3.e5271_s2726_r7772_r7676_p2949
mc15_13TeV.364110.Sherpa_221_NNPDF30NNLO_Zmumu_MAXHTPTV280_500_CFilterBVeto.merge.DAOD_SUSY3.e5271_s2726_r7772_r7676_p2949
mc15_13TeV.364111.Sherpa_221_NNPDF30NNLO_Zmumu_MAXHTPTV280_500_BFilter.merge.DAOD_SUSY3.e5271_s2726_r7772_r7676_p2949
mc15_13TeV.364112.Sherpa_221_NNPDF30NNLO_Zmumu_MAXHTPTV500_1000.merge.DAOD_SUSY3.e5271_s2726_r7772_r7676_p2949
mc15_13TeV.364113.Sherpa_221_NNPDF30NNLO_Zmumu_MAXHTPTV1000_E_CMS.merge.DAOD_SUSY3.e5271_s2726_r7772_r7676_p2949
mc15_13TeV.364114.Sherpa_221_NNPDF30NNLO_Zee_MAXHTPTV0_70_CVetoBVeto.merge.DAOD_SUSY3.e5299_s2726_r7772_r7676_p2949
mc15_13TeV.364115.Sherpa_221_NNPDF30NNLO_Zee_MAXHTPTV0_70_CFilterBVeto.merge.DAOD_SUSY3.e5299_s2726_r7772_r7676_p2949
mc15_13TeV.364116.Sherpa_221_NNPDF30NNLO_Zee_MAXHTPTV0_70_BFilter.merge.DAOD_SUSY3.e5299_s2726_r7772_r7676_p2949
mc15_13TeV.364117.Sherpa_221_NNPDF30NNLO_Zee_MAXHTPTV70_140_CVetoBVeto.merge.DAOD_SUSY3.e5299_s2726_r7772_r7676_p2949
mc15_13TeV.364118.Sherpa_221_NNPDF30NNLO_Zee_MAXHTPTV70_140_CFilterBVeto.merge.DAOD_SUSY3.e5299_s2726_r7772_r7676_p2949
mc15_13TeV.364119.Sherpa_221_NNPDF30NNLO_Zee_MAXHTPTV70_140_BFilter.merge.DAOD_SUSY3.e5299_s2726_r7772_r7676_p2949
mc15_13TeV.364120.Sherpa_221_NNPDF30NNLO_Zee_MAXHTPTV140_280_CVetoBVeto.merge.DAOD_SUSY3.e5299_s2726_r7772_r7676_p2949
mc15_13TeV.364121.Sherpa_221_NNPDF30NNLO_Zee_MAXHTPTV140_280_CFilterBVeto.merge.DAOD_SUSY3.e5299_s2726_r7772_r7676_p2949
mc15_13TeV.364122.Sherpa_221_NNPDF30NNLO_Zee_MAXHTPTV140_280_BFilter.merge.DAOD_SUSY3.e5299_s2726_r7772_r7676_p2949
mc15_13TeV.364123.Sherpa_221_NNPDF30NNLO_Zee_MAXHTPTV280_500_CVetoBVeto.merge.DAOD_SUSY3.e5299_s2726_r7772_r7676_p2949
mc15_13TeV.364124.Sherpa_221_NNPDF30NNLO_Zee_MAXHTPTV280_500_CFilterBVeto.merge.DAOD_SUSY3.e5299_s2726_r7772_r7676_p2949
mc15_13TeV.364125.Sherpa_221_NNPDF30NNLO_Zee_MAXHTPTV280_500_BFilter.merge.DAOD_SUSY3.e5299_s2726_r7772_r7676_p2949
mc15_13TeV.364126.Sherpa_221_NNPDF30NNLO_Zee_MAXHTPTV500_1000.merge.DAOD_SUSY3.e5299_s2726_r7772_r7676_p2949
mc15_13TeV.364127.Sherpa_221_NNPDF30NNLO_Zee_MAXHTPTV1000_E_CMS.merge.DAOD_SUSY3.e5299_s2726_r7772_r7676_p2949
mc15_13TeV.364128.Sherpa_221_NNPDF30NNLO_Ztautau_MAXHTPTV0_70_CVetoBVeto.merge.DAOD_SUSY3.e5307_s2726_r7772_r7676_p2949
mc15_13TeV.364129.Sherpa_221_NNPDF30NNLO_Ztautau_MAXHTPTV0_70_CFilterBVeto.merge.DAOD_SUSY3.e5307_s2726_r7772_r7676_p2949
mc15_13TeV.364130.Sherpa_221_NNPDF30NNLO_Ztautau_MAXHTPTV0_70_BFilter.merge.DAOD_SUSY3.e5307_s2726_r7772_r7676_p2949
mc15_13TeV.364131.Sherpa_221_NNPDF30NNLO_Ztautau_MAXHTPTV70_140_CVetoBVeto.merge.DAOD_SUSY3.e5307_s2726_r7772_r7676_p2949
mc15_13TeV.364132.Sherpa_221_NNPDF30NNLO_Ztautau_MAXHTPTV70_140_CFilterBVeto.merge.DAOD_SUSY3.e5307_s2726_r7772_r7676_p2949
mc15_13TeV.364133.Sherpa_221_NNPDF30NNLO_Ztautau_MAXHTPTV70_140_BFilter.merge.DAOD_SUSY3.e5307_s2726_r7772_r7676_p2949
mc15_13TeV.364134.Sherpa_221_NNPDF30NNLO_Ztautau_MAXHTPTV140_280_CVetoBVeto.merge.DAOD_SUSY3.e5307_s2726_r7772_r7676_p2949
mc15_13TeV.364135.Sherpa_221_NNPDF30NNLO_Ztautau_MAXHTPTV140_280_CFilterBVeto.merge.DAOD_SUSY3.e5307_s2726_r7772_r7676_p2949
mc15_13TeV.364136.Sherpa_221_NNPDF30NNLO_Ztautau_MAXHTPTV140_280_BFilter.merge.DAOD_SUSY3.e5307_s2726_r7772_r7676_p2949
mc15_13TeV.364137.Sherpa_221_NNPDF30NNLO_Ztautau_MAXHTPTV280_500_CVetoBVeto.merge.DAOD_SUSY3.e5307_s2726_r7772_r7676_p2949
mc15_13TeV.364138.Sherpa_221_NNPDF30NNLO_Ztautau_MAXHTPTV280_500_CFilterBVeto.merge.DAOD_SUSY3.e5313_s2726_r7772_r7676_p2949
mc15_13TeV.364139.Sherpa_221_NNPDF30NNLO_Ztautau_MAXHTPTV280_500_BFilter.merge.DAOD_SUSY3.e5313_s2726_r7772_r7676_p2949
mc15_13TeV.364140.Sherpa_221_NNPDF30NNLO_Ztautau_MAXHTPTV500_1000.merge.DAOD_SUSY3.e5307_s2726_r7772_r7676_p2949
mc15_13TeV.364141.Sherpa_221_NNPDF30NNLO_Ztautau_MAXHTPTV1000_E_CMS.merge.DAOD_SUSY3.e5307_s2726_r7772_r7676_p2949
mc15_13TeV.364142.Sherpa_221_NNPDF30NNLO_Znunu_MAXHTPTV0_70_CVetoBVeto.merge.DAOD_SUSY3.e5308_s2726_r7772_r7676_p2949
mc15_13TeV.364143.Sherpa_221_NNPDF30NNLO_Znunu_MAXHTPTV0_70_CFilterBVeto.merge.DAOD_SUSY3.e5308_s2726_r7772_r7676_p2949
mc15_13TeV.364144.Sherpa_221_NNPDF30NNLO_Znunu_MAXHTPTV0_70_BFilter.merge.DAOD_SUSY3.e5308_s2726_r7772_r7676_p2949
mc15_13TeV.364145.Sherpa_221_NNPDF30NNLO_Znunu_MAXHTPTV70_140_CVetoBVeto.merge.DAOD_SUSY3.e5308_s2726_r7772_r7676_p2949
mc15_13TeV.364146.Sherpa_221_NNPDF30NNLO_Znunu_MAXHTPTV70_140_CFilterBVeto.merge.DAOD_SUSY3.e5308_s2726_r7772_r7676_p2949
mc15_13TeV.364147.Sherpa_221_NNPDF30NNLO_Znunu_MAXHTPTV70_140_BFilter.merge.DAOD_SUSY3.e5308_s2726_r7772_r7676_p2949
mc15_13TeV.364148.Sherpa_221_NNPDF30NNLO_Znunu_MAXHTPTV140_280_CVetoBVeto.merge.DAOD_SUSY3.e5308_s2726_r7772_r7676_p2949
mc15_13TeV.364149.Sherpa_221_NNPDF30NNLO_Znunu_MAXHTPTV140_280_CFilterBVeto.merge.DAOD_SUSY3.e5308_s2726_r7772_r7676_p2949
mc15_13TeV.364150.Sherpa_221_NNPDF30NNLO_Znunu_MAXHTPTV140_280_BFilter.merge.DAOD_SUSY3.e5308_s2726_r7772_r7676_p2949
mc15_13TeV.364151.Sherpa_221_NNPDF30NNLO_Znunu_MAXHTPTV280_500_CVetoBVeto.merge.DAOD_SUSY3.e5308_s2726_r7772_r7676_p2949
mc15_13TeV.364152.Sherpa_221_NNPDF30NNLO_Znunu_MAXHTPTV280_500_CFilterBVeto.merge.DAOD_SUSY3.e5308_s2726_r7772_r7676_p2949

mc15_13TeV.364153.Sherpa_221_NNPDF30NNLO_Znunu_MAXHTPTV280_500_BFilter.merge.DAOD_SUSY3.e5308_s2726_r7772_r7676_p2949
mc15_13TeV.364154.Sherpa_221_NNPDF30NNLO_Znunu_MAXHTPTV500_1000.merge.DAOD_SUSY3.e5308_s2726_r7772_r7676_p2949
mc15_13TeV.364155.Sherpa_221_NNPDF30NNLO_Znunu_MAXHTPTV1000_E_CMS.merge.DAOD_SUSY3.e5308_s2726_r7772_r7676_p2949
mc15_13TeV.364198.Sherpa_221_NN30NNLO_Zmm_Mll10_40_MAXHTPTV0_70_BVeto.merge.DAOD_SUSY3.e5421_s2726_r7772_r7676_p2949
mc15_13TeV.364199.Sherpa_221_NN30NNLO_Zmm_Mll10_40_MAXHTPTV0_70_BFilter.merge.DAOD_SUSY3.e5421_s2726_r7772_r7676_p2949
mc15_13TeV.364200.Sherpa_221_NN30NNLO_Zmm_Mll10_40_MAXHTPTV70_280_BVeto.merge.DAOD_SUSY3.e5421_s2726_r7772_r7676_p2949
mc15_13TeV.364201.Sherpa_221_NN30NNLO_Zmm_Mll10_40_MAXHTPTV70_280_BFilter.merge.DAOD_SUSY3.e5421_s2726_r7772_r7676_p2949
mc15_13TeV.364202.Sherpa_221_NN30NNLO_Zmm_Mll10_40_MAXHTPTV280_E_CMS_BVeto.merge.DAOD_SUSY3.e5421_s2726_r7772_r7676_p2949
mc15_13TeV.364203.Sherpa_221_NN30NNLO_Zmm_Mll10_40_MAXHTPTV280_E_CMS_BFilter.merge.DAOD_SUSY3.e5421_s2726_r7772_r7676_p2949
mc15_13TeV.364204.Sherpa_221_NN30NNLO_Zee_Mll10_40_MAXHTPTV0_70_BVeto.merge.DAOD_SUSY3.e5421_s2726_r7772_r7676_p2949
mc15_13TeV.364205.Sherpa_221_NN30NNLO_Zee_Mll10_40_MAXHTPTV0_70_BFilter.merge.DAOD_SUSY3.e5421_s2726_r7772_r7676_p2949
mc15_13TeV.364206.Sherpa_221_NN30NNLO_Zee_Mll10_40_MAXHTPTV70_280_BVeto.merge.DAOD_SUSY3.e5421_s2726_r7772_r7676_p2949
mc15_13TeV.364207.Sherpa_221_NN30NNLO_Zee_Mll10_40_MAXHTPTV70_280_BFilter.merge.DAOD_SUSY3.e5421_s2726_r7772_r7676_p2949
mc15_13TeV.364208.Sherpa_221_NN30NNLO_Zee_Mll10_40_MAXHTPTV280_E_CMS_BVeto.merge.DAOD_SUSY3.e5421_s2726_r7772_r7676_p2949
mc15_13TeV.364209.Sherpa_221_NN30NNLO_Zee_Mll10_40_MAXHTPTV280_E_CMS_BFilter.merge.DAOD_SUSY3.e5421_s2726_r7772_r7676_p2949
mc15_13TeV.364210.Sherpa_221_NN30NNLO_Ztt_Mll10_40_MAXHTPTV0_70_BVeto.merge.DAOD_SUSY3.e5421_s2726_r7772_r7676_p2949
mc15_13TeV.364211.Sherpa_221_NN30NNLO_Ztt_Mll10_40_MAXHTPTV0_70_BFilter.merge.DAOD_SUSY3.e5421_s2726_r7772_r7676_p2949
mc15_13TeV.364212.Sherpa_221_NN30NNLO_Ztt_Mll10_40_MAXHTPTV70_280_BVeto.merge.DAOD_SUSY3.e5421_s2726_r7772_r7676_p2949
mc15_13TeV.364213.Sherpa_221_NN30NNLO_Ztt_Mll10_40_MAXHTPTV70_280_BFilter.merge.DAOD_SUSY3.e5421_s2726_r7772_r7676_p2949
mc15_13TeV.364214.Sherpa_221_NN30NNLO_Ztt_Mll10_40_MAXHTPTV280_E_CMS_BVeto.merge.DAOD_SUSY3.e5421_s2726_r7772_r7676_p2949
mc15_13TeV.364215.Sherpa_221_NN30NNLO_Ztt_Mll10_40_MAXHTPTV280_E_CMS_BFilter.merge.DAOD_SUSY3.e5421_s2726_r7772_r7676_p2949

Appendix II: Distributions of a subset of variables for the Tau Promotion method

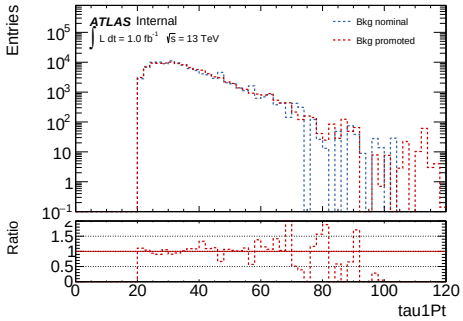

(a) $p_{\mathrm{T}}(\tau_1)$ [GeV]

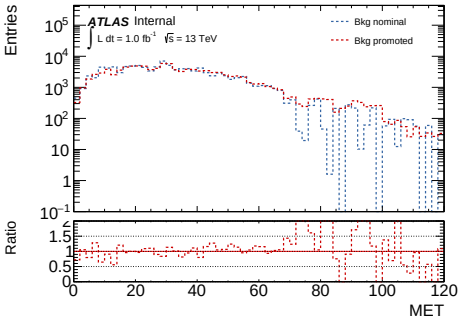

(b) MET

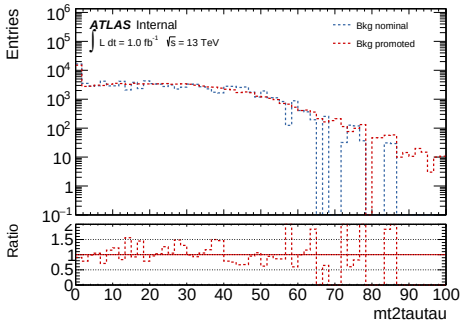

(c) $m_{\mathrm{T2}}(\tau_1, \tau_2)$

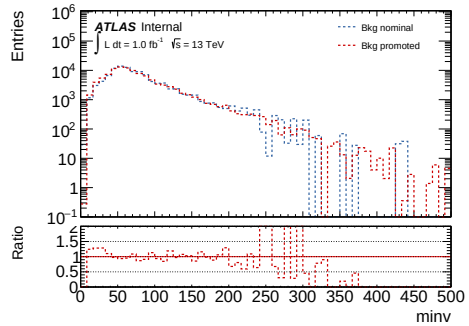

(d) m_{inv}

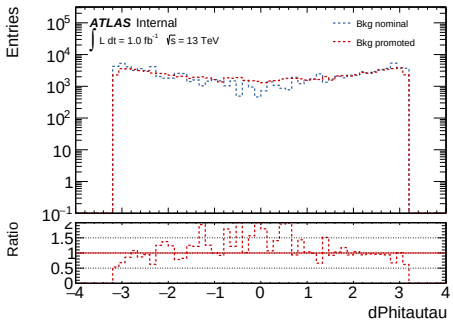

(e) $\Delta\phi(\tau_1, \tau_2)$

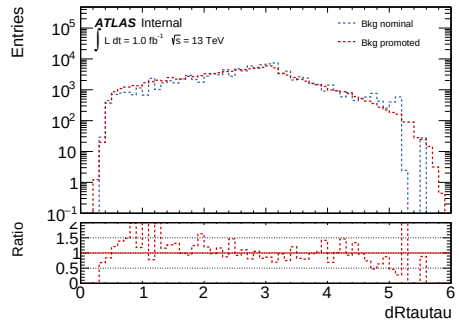

(f) $\Delta\mathrm{R}(\tau_1, \tau_2)$

Figure .1: Distributions for DSID 364184 ($\mathbf{0}$ GeV $< p_{\mathrm{T}}(W) <$ $\mathbf{70}$ GeV, light jet) before (blue) and after (red) Tau Promotion was applied. It can be observed that the reweighted curve has less fluctuations compared to the nominal one. The container taus are promoted to the medium working point. The ratio plot shows the agreement between the nominal and the reweighted curve.

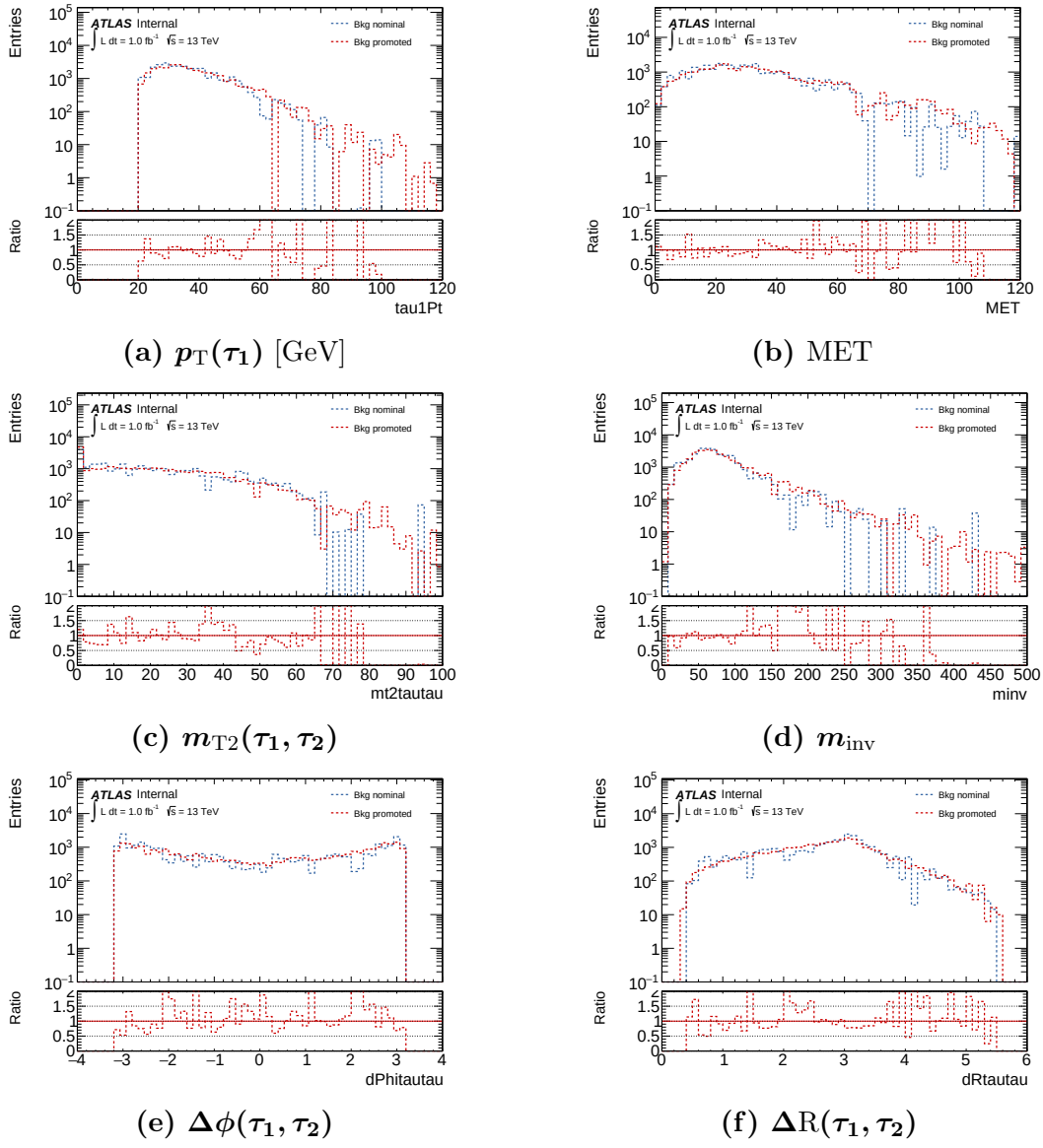

(a) $p_{\mathrm{T}}(\tau_1)$ [GeV] **(b)** MET

(c) $m_{\mathrm{T2}}(\tau_1, \tau_2)$ **(d)** m_{inv}

(e) $\Delta\phi(\tau_1, \tau_2)$ **(f)** $\Delta\mathrm{R}(\tau_1, \tau_2)$

Figure .2: Distributions for DSID 364185 ($\mathbf{0}$ GeV $< p_{\mathrm{T}}(W) <$ $\mathbf{70}$ GeV, c-jet) before (blue) and after (red) Tau Promotion was applied. It can be observed that the reweighted curve has less fluctuations compared to the nominal one. The ratio plot shows the agreement between the nominal and the reweighted curve.

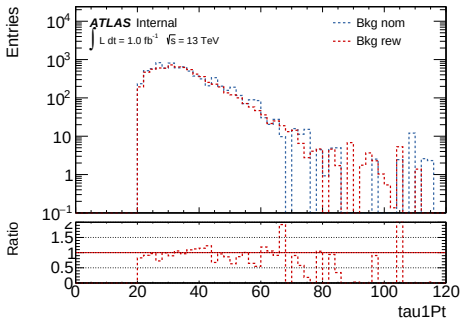

(a) $p_{\mathrm{T}}(\tau_1)$ [GeV]

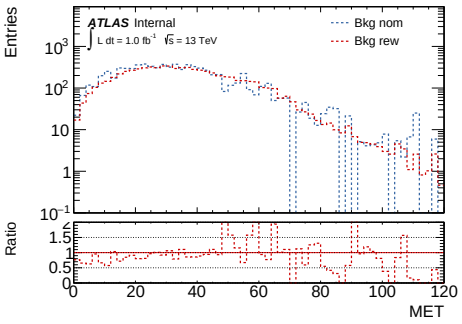

(b) MET

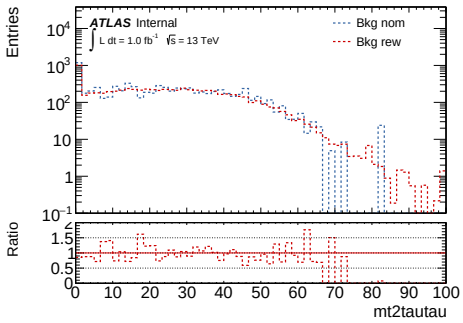

(c) $m_{\mathrm{T2}}(\tau_1, \tau_2)$

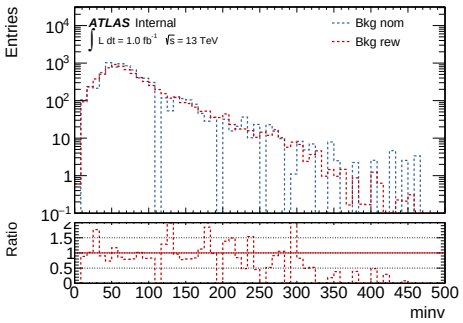

(d) m_{inv}

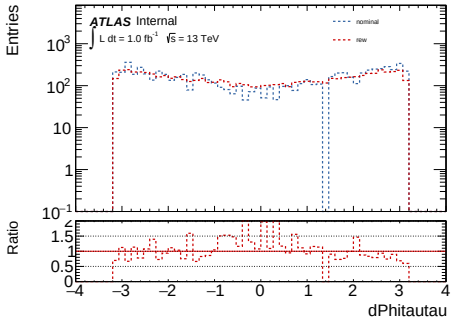

(e) $\Delta\phi(\tau_1, \tau_2)$

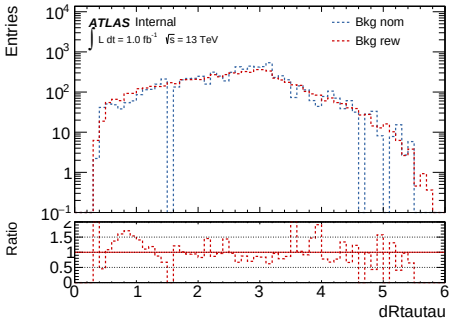

(f) $\Delta\mathrm{R}(\tau_1, \tau_2)$

Figure .3: Distributions for DSID 364186 ($\mathbf{0}$ GeV $< p_{\mathrm{T}}(W) <$ $\mathbf{70}$ GeV, b-jet) before (blue) and after (red) Tau Promotion was applied. It can be observed that the reweighted curve has less fluctuations compared to the nominal one. The ratio plot shows the agreement between the nominal and the reweighted curve.

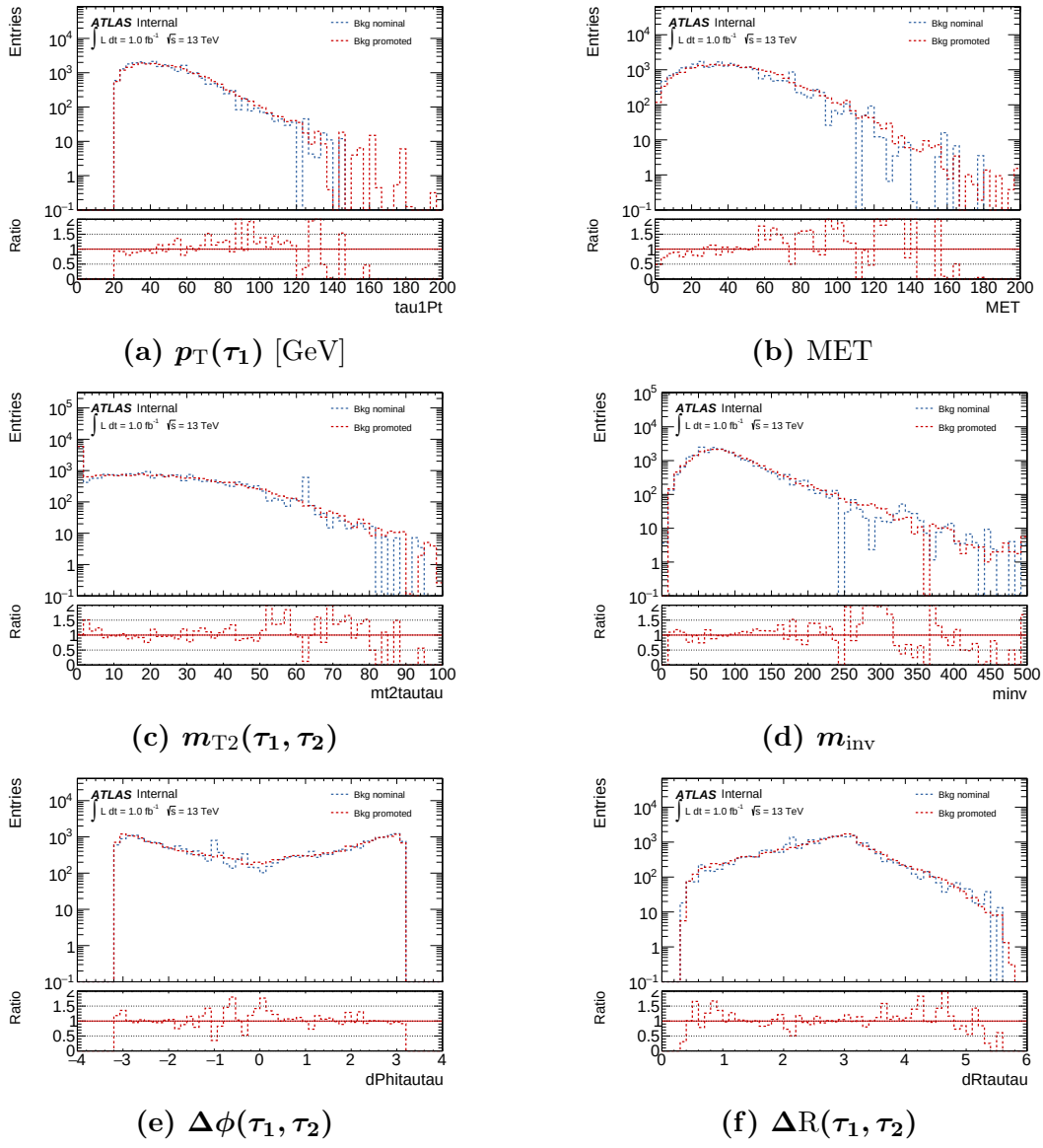

(a) $p_{\mathrm{T}}(\tau_1)$ [GeV] **(b)** MET

(c) $m_{\mathrm{T2}}(\tau_1, \tau_2)$ **(d)** m_{inv}

(e) $\Delta\phi(\tau_1, \tau_2)$ **(f)** $\Delta\mathrm{R}(\tau_1, \tau_2)$

Figure .4: Distributions for DSID 364187 ($\mathbf{70}\,\mathrm{GeV} < p_{\mathrm{T}}(W) < \mathbf{140}\,\mathrm{GeV}$, light jet) before (blue) and after (red) Tau Promotion was applied. It can be observed that the reweighted curve has less fluctuations compared to the nominal one. The ratio plot shows the agreement between the nominal and the reweighted curve.

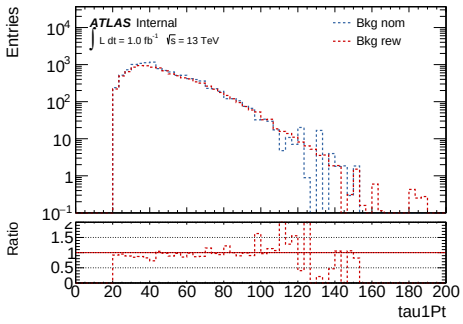

(a) $p_{\mathrm{T}}(\tau_1)$ [GeV]

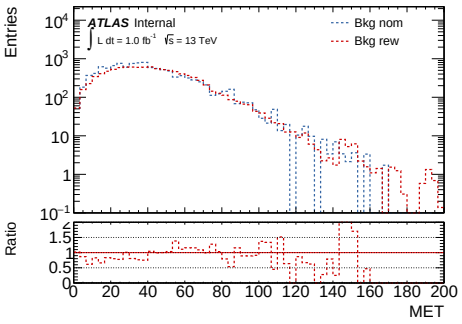

(b) MET

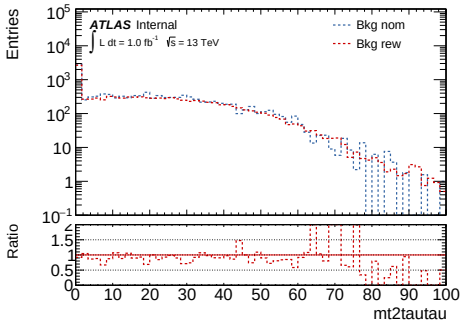

(c) $m_{\mathrm{T2}}(\tau_1, \tau_2)$

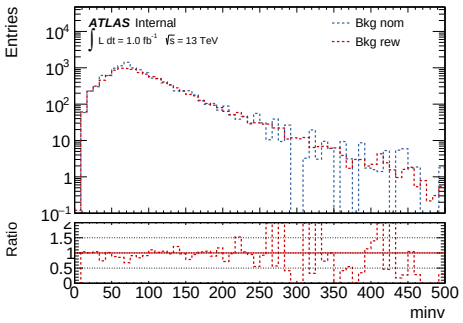

(d) m_{inv}

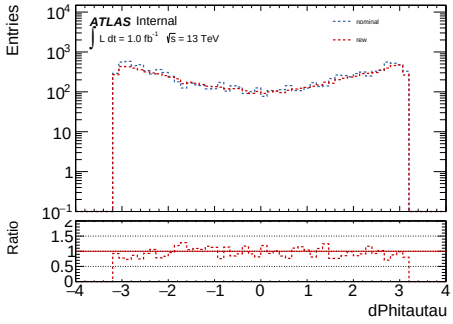

(e) $\Delta\phi(\tau_1, \tau_2)$

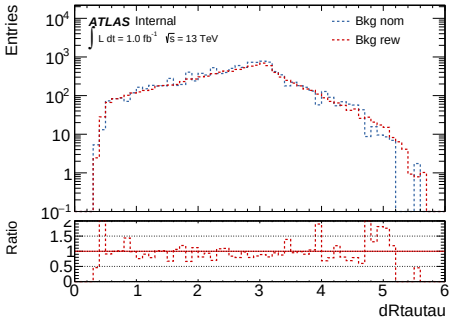

(f) $\Delta\mathrm{R}(\tau_1, \tau_2)$

Figure .5: Distributions for DSID 364188 ($\mathbf{70}\,\mathrm{GeV} < p_{\mathrm{T}}(W) < \mathbf{140}\,\mathrm{GeV}$, c-jet) before (blue) and after (red) Tau Promotion was applied. It can be observed that the reweighted curve has less fluctuations compared to the nominal one. The ratio plot shows the agreement between the nominal and the reweighted curve.

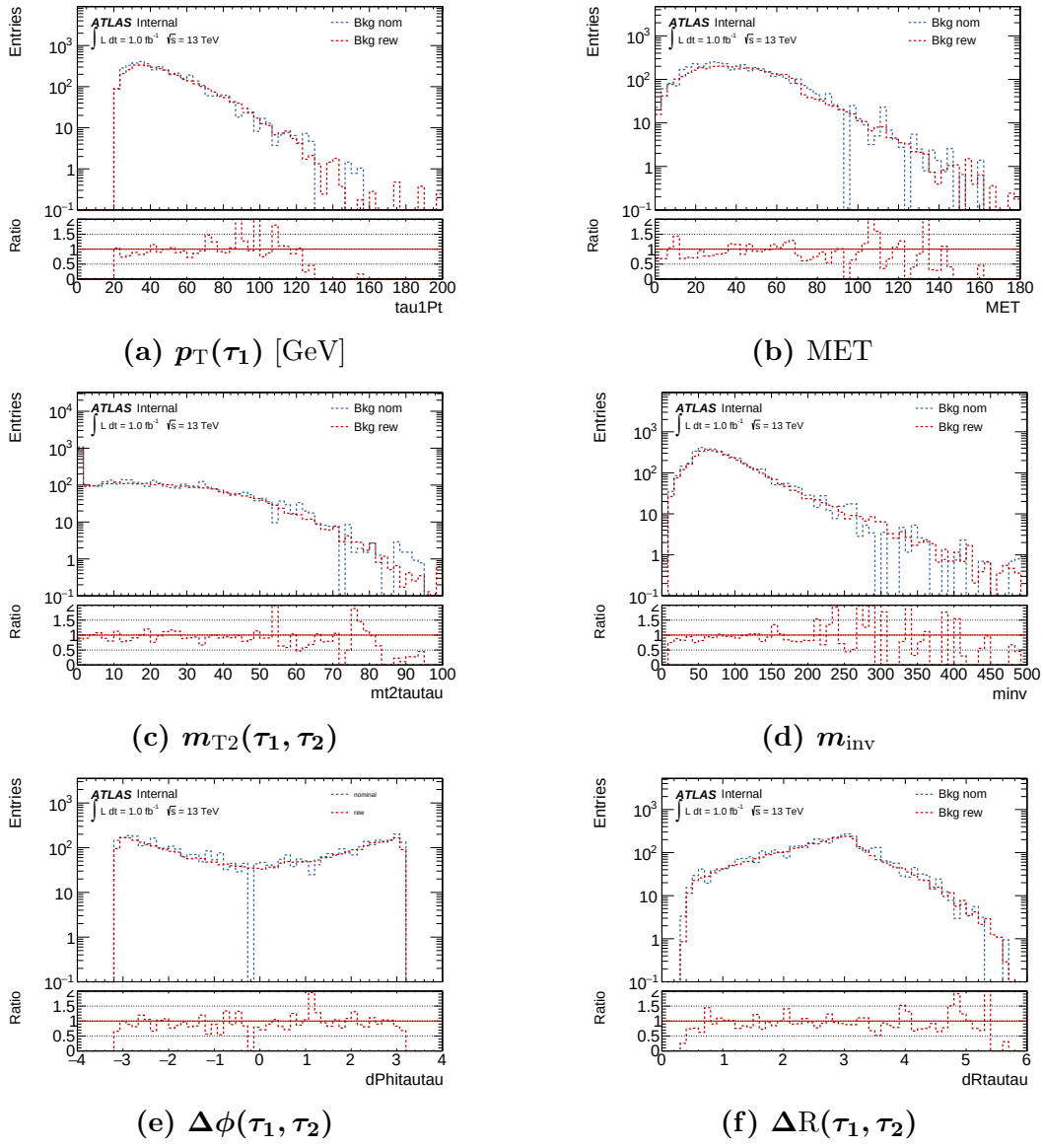

(a) $p_{\mathrm{T}}(\tau_1)$ [GeV] **(b)** MET

(c) $m_{\mathrm{T2}}(\tau_1, \tau_2)$ **(d)** m_{inv}

(e) $\Delta\phi(\tau_1, \tau_2)$ **(f)** $\Delta\mathrm{R}(\tau_1, \tau_2)$

Figure .6: Distributions for DSID 364189 ($\mathbf{70}\,\mathrm{GeV} < p_{\mathrm{T}}(W) < \mathbf{140}\,\mathrm{GeV}$, b-jet) before (blue) and after (red) Tau Promotion was applied. It can be observed that the reweighted curve has less fluctuations compared to the nominal one. The ratio plot shows the agreement between the nominal and the reweighted curve.

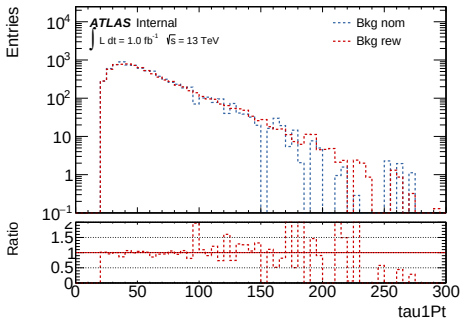

(a) $p_{\mathrm{T}}(\tau_1)$ [GeV]

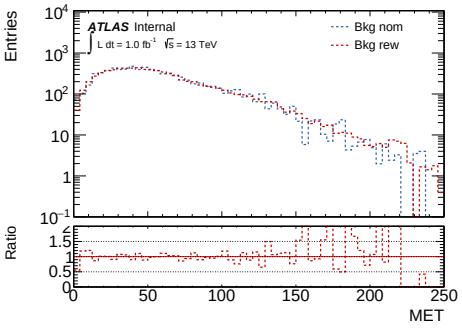

(b) MET

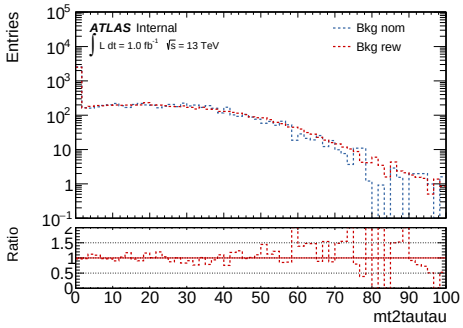

(c) $m_{\mathrm{T2}}(\tau_1, \tau_2)$

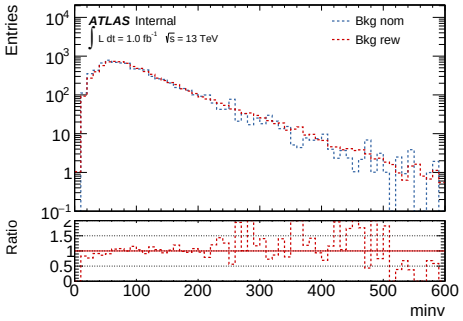

(d) m_{inv}

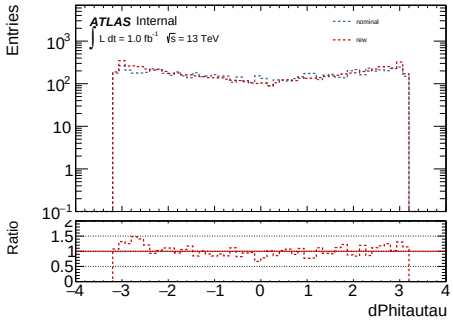

(e) $\Delta\phi(\tau_1, \tau_2)$

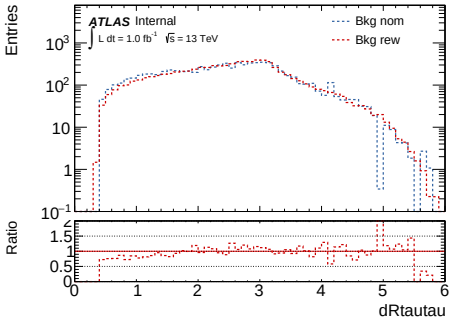

(f) $\Delta\mathrm{R}(\tau_1, \tau_2)$

Figure .7: Distributions for DSID 364190 (**140** GeV $<$ $p_{\mathrm{T}}(W)$ $<$ ***GeV*280** GeV, light jet) before (blue) and after (red) Tau Promotion was applied. It can be observed that the reweighted curve has less fluctuations compared to the nominal one. The ratio plot shows the agreement between the nominal and the reweighted curve.

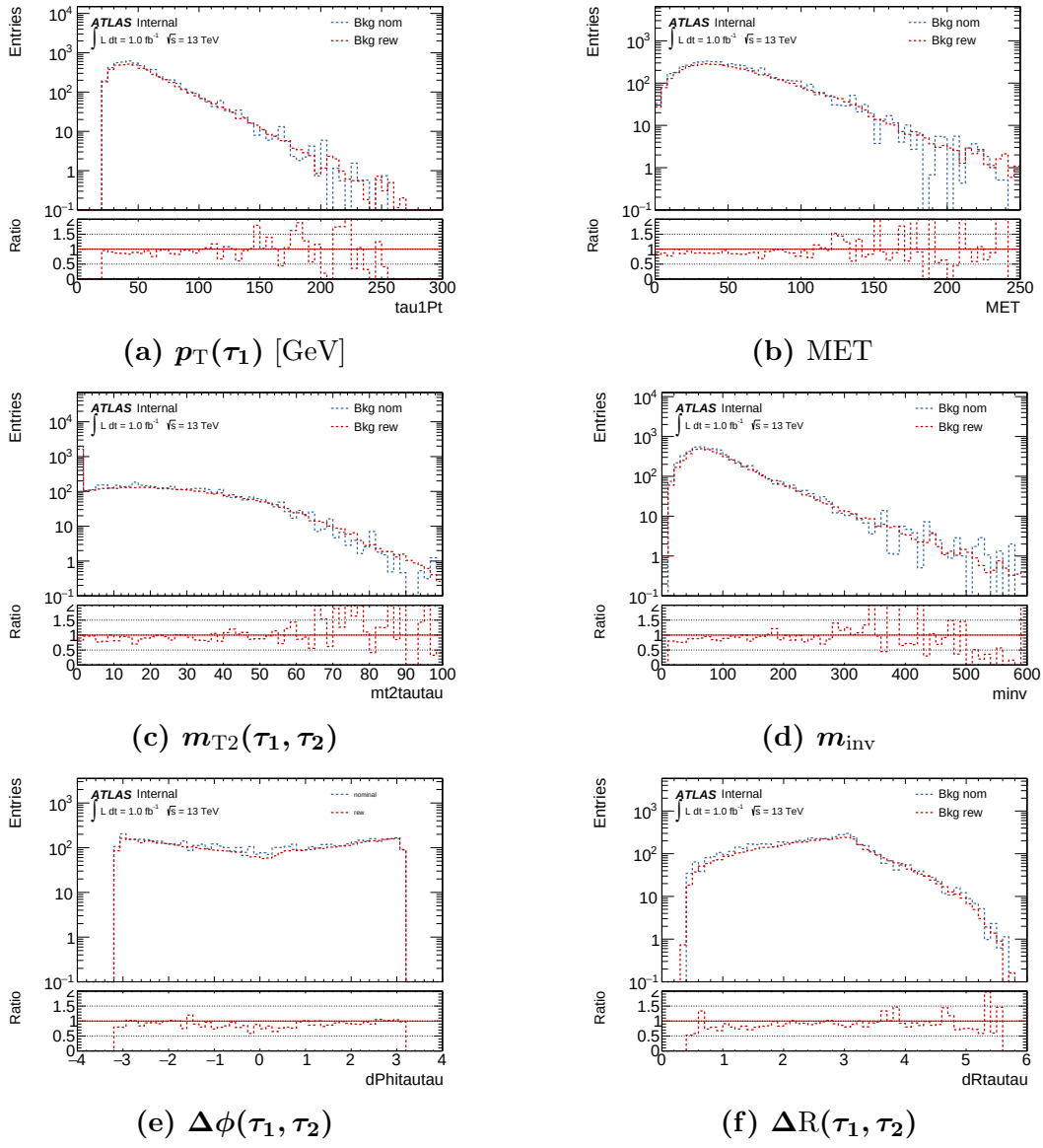

(a) $p_{\mathrm{T}}(\tau_1)$ [GeV] **(b)** MET

(c) $m_{\mathrm{T2}}(\tau_1, \tau_2)$ **(d)** m_{inv}

(e) $\Delta\phi(\tau_1, \tau_2)$ **(f)** $\Delta\mathrm{R}(\tau_1, \tau_2)$

Figure .8: Distributions for DSID 364191 ($\mathbf{140}\,\mathrm{GeV} < p_{\mathrm{T}}(W) < \mathbf{280}\,\mathrm{GeV}$, c-jet) before (blue) and after (red) Tau Promotion was applied. It can be observed that the reweighted curve has less fluctuations compared to the nominal one. The ratio plot shows the agreement between the nominal and the reweighted curve.

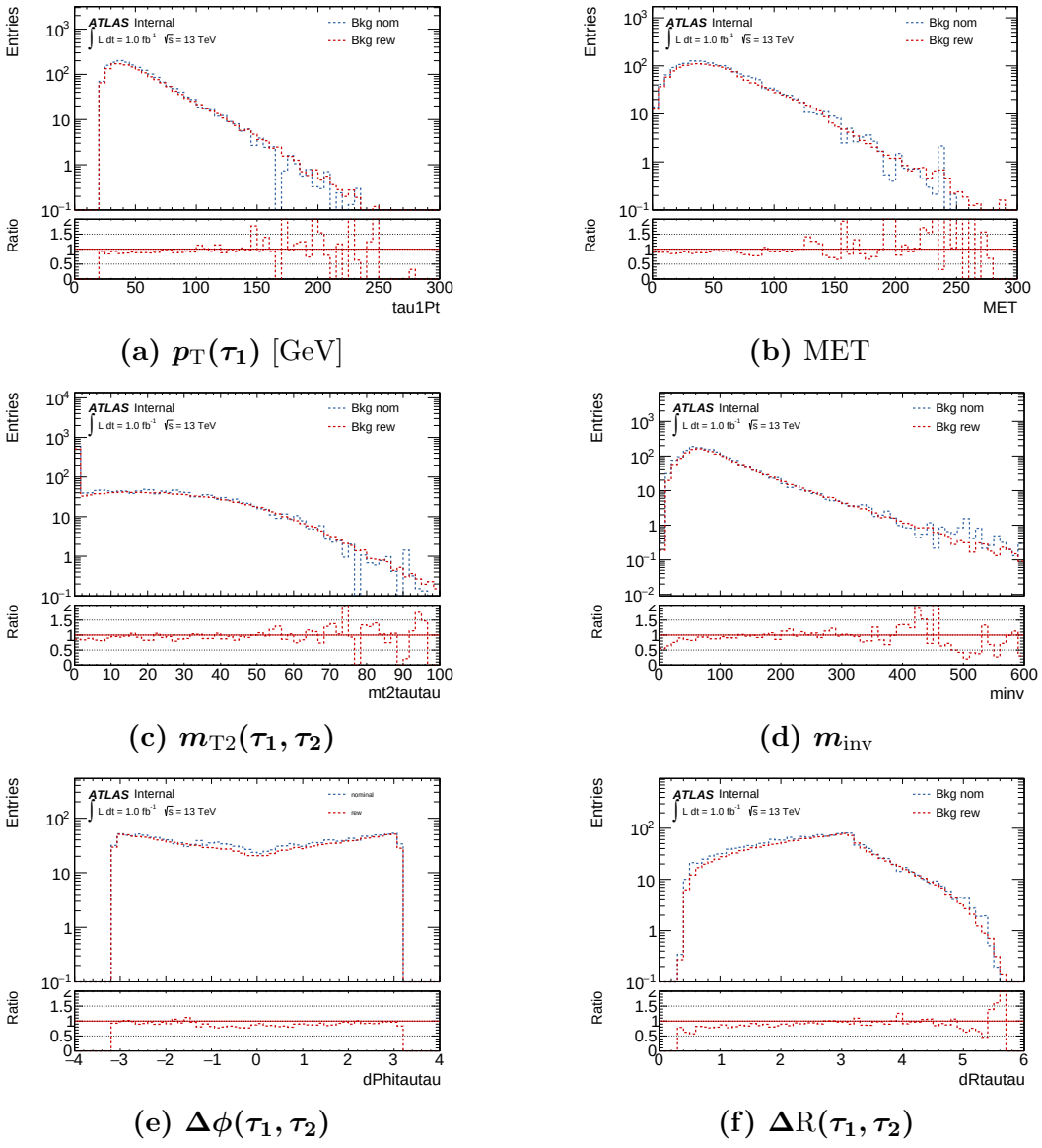

(a) $p_{\mathrm{T}}(\tau_1)$ [GeV] **(b)** MET

(c) $m_{\mathrm{T2}}(\tau_1, \tau_2)$ **(d)** m_{inv}

(e) $\Delta\phi(\tau_1, \tau_2)$ **(f)** $\Delta\mathrm{R}(\tau_1, \tau_2)$

Figure .9: Distributions for DSID 364192 ($\mathbf{140}\,\mathrm{GeV} < p_{\mathrm{T}}(W) < \mathbf{280}\,\mathrm{GeV}$, b-jet) before (blue) and after (red) Tau Promotion was applied. It can be observed that the reweighted curve has less fluctuations compared to the nominal one. The ratio plot shows the agreement between the nominal and the reweighted curve.

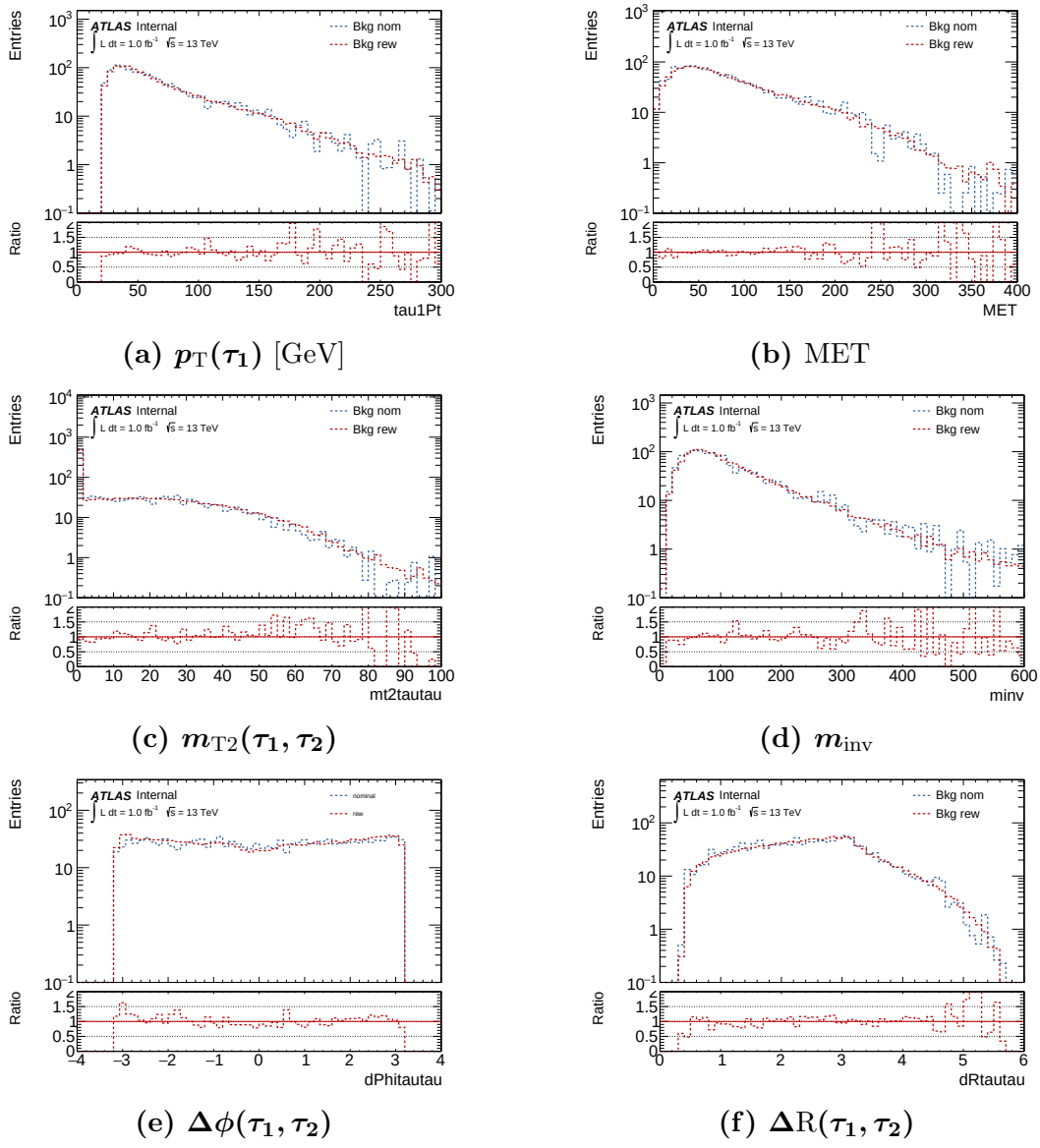

(a) $p_{\mathrm{T}}(\tau_1)$ [GeV] **(b)** MET

(c) $m_{\mathrm{T2}}(\tau_1, \tau_2)$ **(d)** m_{inv}

(e) $\Delta\phi(\tau_1, \tau_2)$ **(f)** $\Delta\mathrm{R}(\tau_1, \tau_2)$

Figure .10: Distributions for DSID 364193 (**280** GeV $< p_{\mathrm{T}}(W) <$ **500** GeV, light jet) before (blue) and after (red) Tau Promotion was applied. It can be observed that the reweighted curve has less fluctuations compared to the nominal one. The ratio plot shows the agreement between the nominal and the reweighted curve.

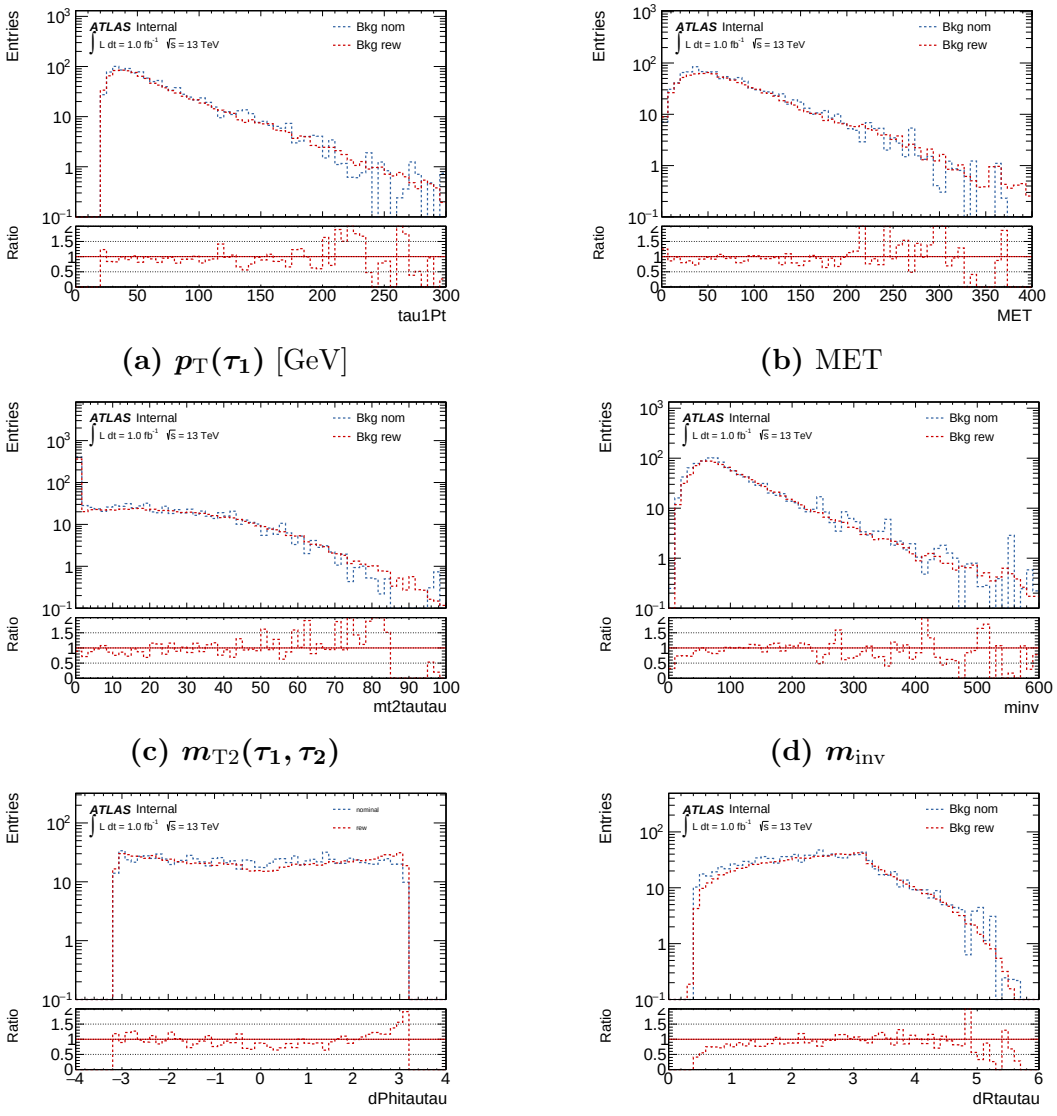

(a) $p_{\mathrm{T}}(\tau_1)$ [GeV] **(b)** MET

(c) $m_{\mathrm{T2}}(\tau_1, \tau_2)$ **(d)** m_{inv}

(e) $\Delta\phi(\tau_1, \tau_2)$ **(f)** $\Delta\mathrm{R}(\tau_1, \tau_2)$

Figure .11: Distributions for DSID 364194 ($\mathbf{280}\,\mathrm{GeV} < p_{\mathrm{T}}(W) < \mathbf{500}\,\mathrm{GeV}$, c-jet) before (blue) and after (red) Tau Promotion was applied. It can be observed that the reweighted curve has less fluctuations compared to the nominal one. The ratio plot shows the agreement between the nominal and the reweighted curve.

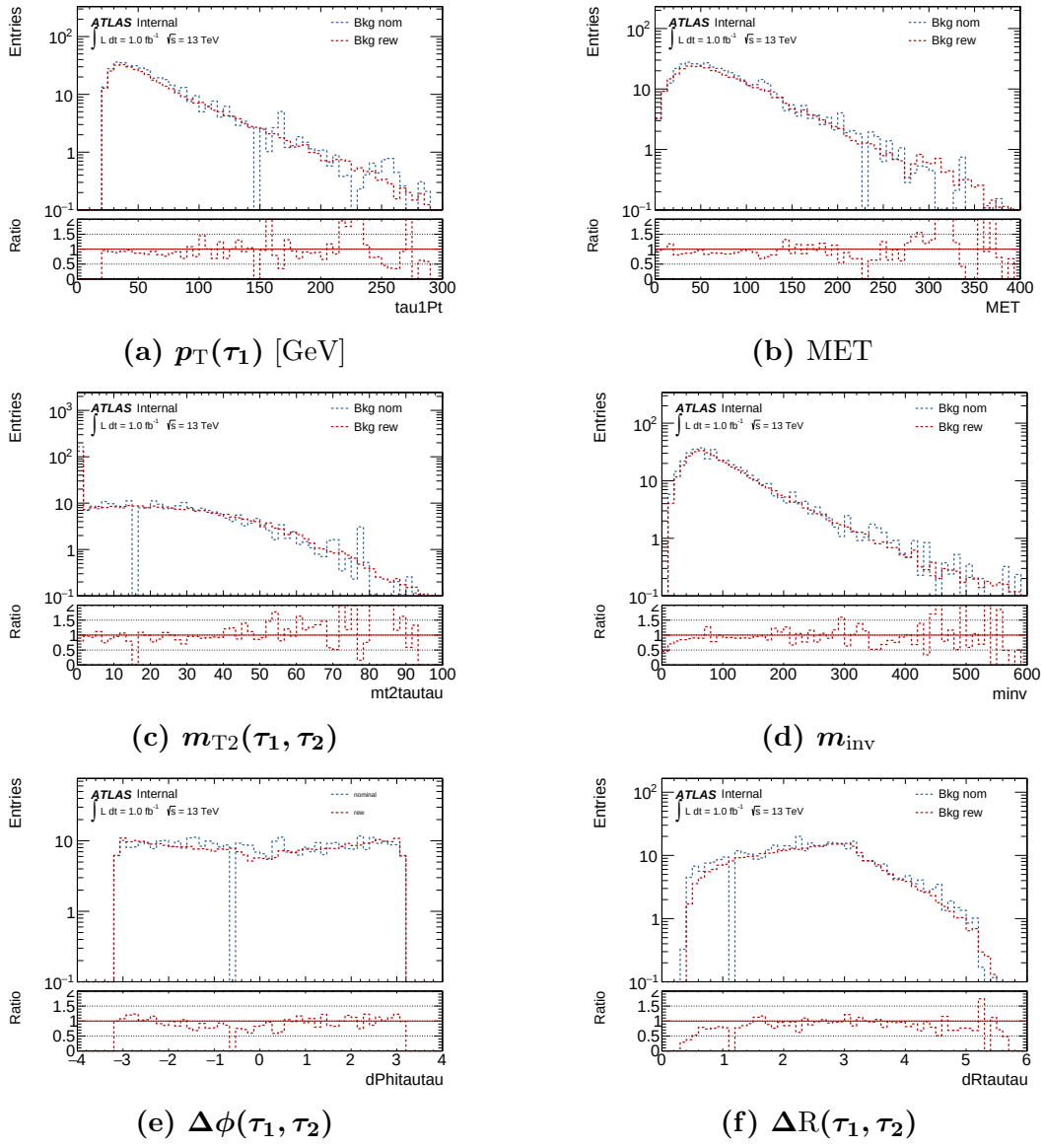

(a) $p_{\mathrm{T}}(\tau_1)$ [GeV] **(b)** MET

(c) $m_{\mathrm{T2}}(\tau_1, \tau_2)$ **(d)** m_{inv}

(e) $\Delta\phi(\tau_1, \tau_2)$ **(f)** $\Delta\mathrm{R}(\tau_1, \tau_2)$

Figure .12: Distributions for DSID 364195 ($\mathbf{280}\,\mathrm{GeV} < p_{\mathrm{T}}(W) < \mathbf{500}\,\mathrm{GeV}$, b-jet) before (blue) and after (red) Tau Promotion was applied. It can be observed that the reweighted curve has less fluctuations compared to the nominal one. The ratio plot shows the agreement between the nominal and the reweighted curve.

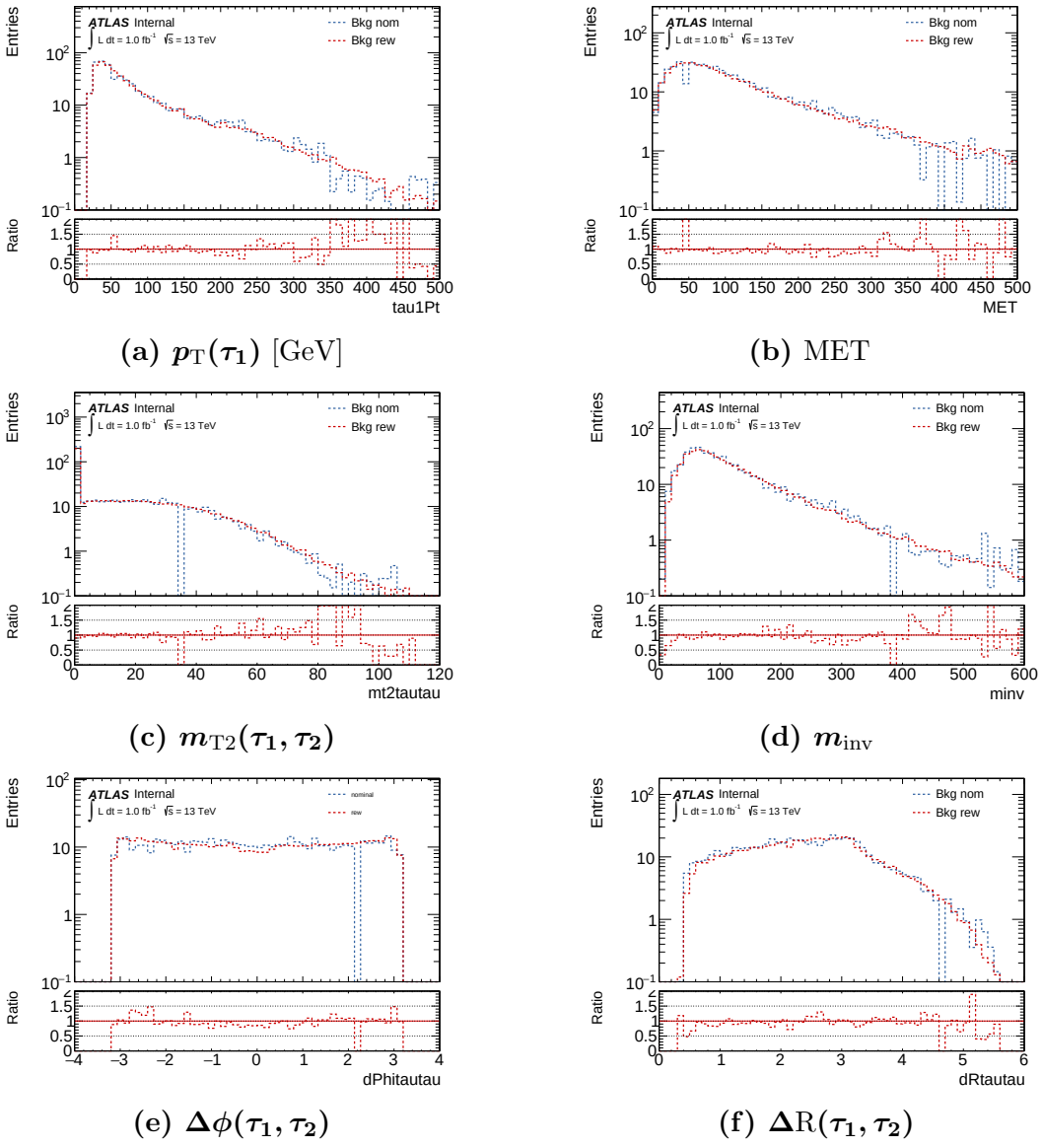

(a) $p_{\mathrm{T}}(\tau_1)$ [GeV] **(b)** MET

(c) $m_{\mathrm{T2}}(\tau_1, \tau_2)$ **(d)** m_{inv}

(e) $\Delta\phi(\tau_1, \tau_2)$ **(f)** $\Delta\mathrm{R}(\tau_1, \tau_2)$

Figure .13: Distributions for DSID 364196 (**500** GeV $< p_{\mathrm{T}}(W) <$ **1000** GeV) before (blue) and after (red) Tau Promotion was applied. It can be observed that the reweighted curve has less fluctuations compared to the nominal one. The ratio plot shows the agreement between the nominal and the reweighted curve.

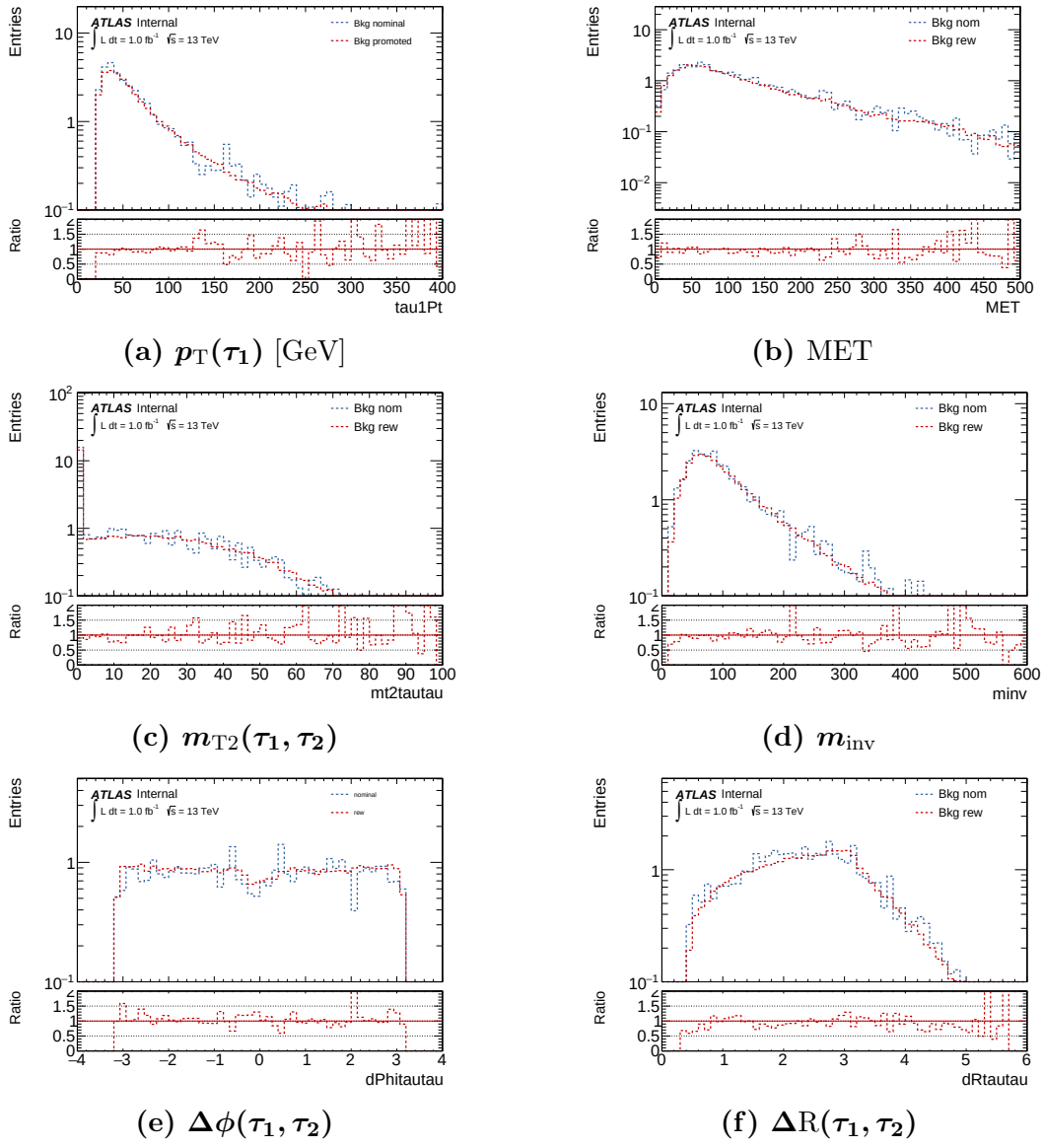

(a) $p_{\mathrm{T}}(\tau_1)$ [GeV] **(b)** MET

(c) $m_{\mathrm{T2}}(\tau_1, \tau_2)$ **(d)** m_{inv}

(e) $\Delta\phi(\tau_1, \tau_2)$ **(f)** $\Delta\mathrm{R}(\tau_1, \tau_2)$

Figure .14: Distributions for DSID 364197 ($p_{\mathrm{T}}(W) \geq 1000$ GeV) before (blue) and after (red) Tau Promotion was applied. It can be observed that the reweighted curve has less fluctuations compared to the nominal one. The ratio plot shows the agreement between the nominal and the reweighted curve.

Bibliography

[1] **ATLAS** Collaboration, ATLAS, "Observation of a new particle in the search for the standard model higgs boson with the atlas detector at the LHC," arXiv:1207.7214.

[2] **CMS** Collaboration, CMS, "Observation of a new boson at a mass of 125 GeV with the CMS experiment at the LHC," arXiv:1207.7235.

[3] D. Griffiths, "Introduction to Elementary Particles," *WILEY-VCH* (2008) .

[4] D. Schaile, "Advanced Particle Physics (Lecture notes)," *LMU Munich* (2015) .

[5] S. P. Martin, "A Supersymmetry Primer," arXiv:hep-ph/9709356.

[6] M. E. Peskin and D. V. Schroede, "An Introduction to Quantum Field Theory," *Westview Press* (1995) .

[7] C. P. et al (Particle Data Group), "Quark summary table," *Chin. Phys. C, 40, 100001* (2016) . http://pdg.lbl.gov/2016/tables/rpp2016-sum-quarks.pdf.

[8] C. P. et al (Particle Data Group), "Lepton summary table," *Chin. Phys. C, 40, 100001* (2016) . http://pdg.lbl.gov/2016/tables/rpp2016-sum-leptons.pdf.

[9] C. P. et al (Particle Data Group), "Boson summary table," *Chin. Phys. C, 40, 100001* (2016) . http://pdg.lbl.gov/2016/tables/rpp2016-sum-gauge-higgs-bosons.pdf.

[10] S. Hughes, "Introduction; Couloumb's law; Superposition; Electric energy (Lecture notes)," *Massachusetts Institute of Technology* (Feb, 2005) . http://web.mit.edu/sahughes/www/8.022/lec01.pdf.

[11] G. Bhattacharyya, "Hierarchy problem and BSM physics," *Pramana J. Phys.* (Oct, 2017) . http://www.ias.ac.in/article/fulltext/pram/089/04/0053.

[12] A. V. Gladyshev and D. I. Kazakov, "IS (Low Energy) SUSY STILL ALIVE?," arXiv:212.2548.

[13] T. Xie, "Supersymmetry And Gauge Couplings Correction,". https://www.researchgate.net/publication/311843425_Supersymmetry_And_Gauge_Couplings_Correction.

[14] P. Binétruy, *Supersymmetry: theory, experiment and cosmology*. Oxford University Press, New York, USA, 1st ed., 2006.

[15] H. Baer and X. Tata, *Weak Scale Supersymmetry: From Superfields to Scattering Events*. Cambridge University Press, New York, USA, 1st ed., 2006.

[16] J. Conlon, "Introduction to supersymmetry (lecture notes)." `https://www-thphys.physics.ox.ac.uk/people/JosephConlon/LectureNotes/SUSYLectures.pdf`. last visited on 2017-04-25.

[17] I. J. R. Aitchison, "Supersymmetry and the MSSM: An Elementary Introduction," `arXiv:hep-ph/0505105`.

[18] Nausheen R. Shah, "Minimal Supersymmetric Standard Model (lecture notes)." `http://theory.uchicago.edu/~sethi/Teaching/P487-S2003/MSSMnausheen.pdf`, Jun, 2003. last visited on 2017-04-28.

[19] **Super-Kamiokande Collaboration** Collaboration, H. Nishino *et al.*, "Search for Proton Decay via $p \to e^+\pi^0$ and $p \to \mu^+\pi^0$ in a Large Water Cherenkov Detector," *Phys. Rev. Lett.* **102** (Apr, 2009) 141801. `https://link.aps.org/doi/10.1103/PhysRevLett.102.141801`.

[20] T. M. Undagoitia, F. von Feilitzsch, M. Goeger-Neff, C. Grieb, K. A. Hochmuth, L. Oberauer, W. Potzel, and M. Wurm, "Search for the proton decay $p \to K +$ antineutrino in the large liquid scintillator low energy neutrino astronomy detector LENA," `arXiv:hep-ph/0511230`.

[21] K. Intriligator and N. Seiberg, "Lectures on supersymmetry breaking," `arXiv:hep-ph/0702069`.

[22] K. Krasnov, "Spontaneous symmetry breaking and gravity," `arXiv:1112.5097`.

[23] G. Jungman, M. Kamionkowski, and K. Griest, "Supersymmetric Dark Matter," *Physics Reports* **267** (1996) 195–373.

[24] K. Garrett and G. Dud, "Dark Matter: A Primer," `arXiv:1006.2483`.

[25] **ATLAS** Collaboration, ATLAS, "Search for the direct production of charginos, neutralinos and staus in final states with at least two hadronically decaying taus and missing transverse momentum in pp collisions at $\sqrt{s}$=8TeV with the ATLAS detector ," `arXiv:1407.0350`.

[26] "The CERN accelerator complex," Jul, 2016. `https://cds.cern.ch/record/2197559`.

[27] "CERN homepage:ATLAS." `http://atlas.cern/discover/detector`. last visited on 2017-11-27.

[28] J. Alison, "The road to discovery: Detector alignment, electron identification, particle misidentification, ww physics, and the discovery of the higgs boson.." https://hep.uchicago.edu/~johnda/thesis/alison_thesis.pdf, 2012. Dissertation.

[29] "Computer generated image of the whole ATLAS detector," Mar, 2008. https://cds.cern.ch/record/1095924.

[30] Z. Marshall, "Simulation of Pile-up in the ATLAS Experiment," *Journal of Physics: Conference Series 513.2* (2014) . http://iopscience.iop.org/article/10.1088/1742-6596/513/2/022024.

[31] R. Gupta, "Introduction to Lattice QCD." http://arxiv.org/abs/hep-lat/9807028.

[32] T. Sjostrand, "Monte Carlo Event Generation for LHC," 1991. http://home.thep.lu.se/~torbjorn/preprints/th6275.pdf.

[33] M. Dobbs et al., "Les Houches Guidebook to Monte Carlo Generators for Hadron Collider Physics," 2004. http://arxiv.org/abs/hep-ph/0403045v2.

[34] C. Leitgeb, "Search for Direct Production of Supersymmetric Scalar Tau Leptons Using 13 TeV Data Taken with the ATLAS Detector at the LHC." https://www.etp.physik.uni-muenchen.de/publications/theses/download/master_cleitgeb.pdf, Oct., 2017. Master Thesis.

[35] University of Oxford, "How ATLAS Detects Particles,". http://collider.physics.ox.ac.uk/detecting.html.

[36] **ATLAS** Collaboration, "Electron efficiency measurements with the ATLAS detector using the 2015 LHC proton-proton collision data," Tech. Rep. ATLAS-CONF-2016-024, CERN, Geneva, Jun, 2016. https://cds.cern.ch/record/2157687?ln=de.

[37] **ATLAS** Collaboration, "Electron identification measurements in ATLAS using $\sqrt{s} = 13$ TeV data with 50 ns bunch spacing,," Tech. Rep. ATL-PHYS-PUB-2015-041, CERN, Geneva, Aug, 2015. https://cds.cern.ch/record/2048202/files/ATL-PHYS-PUB-2015-041.pdf.

[38] M. C. et al., "The anti-k_T jet clustering algorithm,". https://arxiv.org/abs/0802.1189.

[39] **ATLAS** Collaboration, "ATLAS jet and missing energy reconstruction, calibration and performance in LHC Run-2," Tech. Rep. ATL-PHYS-PROC-2017-045, CERN, Geneva, May, 2017. https://cds.cern.ch/record/2263777?ln=de.

[40] **ATLAS** Collaboration, "Jet Calibration and Systematic Uncertainties for Jets Reconstructed in the ATLAS Detector at $\sqrt{s} = 13\,\text{TeV}$," Tech. Rep. ATL-PHYS-PUB-2015-015, CERN, Geneva, Jul, 2015. https://cds.cern.ch/record/2037613.

[41] **ATLAS** Collaboration, "Measurement of the tau lepton reconstruction and identification performance in the ATLAS experiment using *pp* collisions at $\sqrt{s}$=13TeV," Tech. Rep. ATLAS-CONF-2017-029, CERN, Geneva, May, 2017. http://cds.cern.ch/record/2261772.

[42] A. H. et al., "TMVA - Toolkit for Multivariate Data Analysis." http://arxiv.org/abs/physics/0703039v5, 2009.

[43] **ATLAS** Collaboration, "Reconstruction, Energy Calibration, and Identification of Hadronically Decaying Tau Leptons in the ATLAS Experiment for Run-2 of the LHC," Tech. Rep. ATL-PHYS-PUB-2015-045, CERN, Geneva, Nov, 2015. https://atlas.web.cern.ch/Atlas/GROUPS/PHYSICS/PUBNOTES/ATL-PHYS-PUB-2015-045/.

[44] **ATLAS** Collaboration, "Performance of missing transverse momentum reconstruction for the ATLAS detector in the first proton-proton collisions at at $\sqrt{s} = 13\,\text{TeV}$," Tech. Rep. ATL-PHYS-PUB-2015-027, CERN, Geneva, Jul, 2015. https://cds.cern.ch/record/2037904.

[45] **ATLAS** Collaboration, "Expected performance of missing transverse momentum reconstruction for the ATLAS detector at $\sqrt{s} = 13\,\text{TeV}$," Tech. Rep. ATL-PHYS-PUB-2015-023, CERN, Geneva, Jul, 2015. https://cds.cern.ch/record/2037700.

[46] B. Abbott, M. Abolins, B. S. Acharya, and et. al, "A measurement of the w boson mass," arXiv:hep-ex/9712029.

[47] **ATLAS** Collaboration, "Search for the direct production of charginos and neutralinos in final states with tau leptons in $\sqrt{s}$=13 TeV *pp* collisions with the ATLAS detector," Tech. Rep. ATLAS-CONF-2017-035, CERN, Geneva, May, 2017. http://cds.cern.ch/record/2265807/files/ATLAS-CONF-2017-035.pdf.

Selbständigkeitserklärung

Ich versichere hiermit, die vorliegende Arbeit mit dem Titel

Improving the modelling of the associated production of W-bosons and jets in the ATLAS detector

(Verbesserung der Modellierung der assoziierten Produktion von W-Bosonen und Jets im ATLAS Detektor)

selbständig verfasst zu haben und keine anderen als die angegebenen Quellen und Hilfsmittel verwendet zu haben.

München, 07. Februar 2018, Adam Samara